

**ZEOLITE AND METAL OXIDE CATALYSTS FOR THE
PRODUCTION OF DIMETHYL SULFIDE AND
METHANETHIOL**

A Thesis,

Submitted to the Graduate Faculty of the
Louisiana State University and
Agricultural and Mechanical College
in partial fulfillment of the
requirements for the degree of
Master of Science in Chemical Engineering

In

The Department of Chemical Engineering

by
Craig Plaisance
B.S., Louisiana State University, 2003
August 2005

ACKNOWLEDGEMENTS

There are many people to whom my thanks are due for the vital roles they played in helping me to complete this thesis. First, I would like to thank my advisor, Kerry M. Dooley for his guidance and instruction during my time working under him. I would like to thank Karsten E. Thompson and Ralph W. Pike for serving on my thesis committee. Thanks to Gaylord Chemical for funding the dimethyl sulfide and methanethiol work. Thanks to EagleView Technologies, Inc. and MGK Co. for funding the metal-doped cerium oxide work. Thanks to the Center for Advanced Microstructures and Devices (CAMD) for allowing use of the synchrotron facilities to conduct X-ray absorption experiments. I would like to thank Amitava D. Roy, Roland C. Tittsworth, and Vadim Palshin for assisting with the X-ray absorption work at CAMD. I would also like to thank Paul Rodriguez, Joe Bell, and Fred McKenzie from the Chemical Engineering Workshop for their assistance. Last, but not least, I would like to thank my family for their moral and financial support over the past two years.

TABLE OF CONTENTS

ACKNOWLEDGEMENTS	ii
LIST OF TABLES	v
LIST OF FIGURES	vi
ABSTRACT	viii
CHAPTER 1. INTRODUCTION AND REVIEW OF LITERATURE	1
1.1 Goals and Project Summary	1
1.2 Reaction Chemistry on Zeolite and Metal Oxide Catalysts	2
1.3 Reaction Mechanisms	4
1.4 Trends in Reactivity and Selectivity	6
1.5 Ab-Initio Calculations	11
1.6 Summary of Literature Review and Proposed Study	13
CHAPTER 2. EXPERIMENTAL	15
2.1 Catalyst Preparation	15
2.2 Continuous Flow Reactor Experiments	15
2.3 Catalyst Characterization	18
CHAPTER 3. RESULTS	20
3.1 Continuous Flow Reactor Experiments	20
3.1.1 Calculations	20
3.1.2 Experimental Reaction Data	27
3.2 Catalyst Deactivation	44
3.3 Acid Site Characterization	45
CHAPTER 4. XAS CHARACTERIZATION OF METAL-DOPED SUPPORTED CERIUM OXIDE CATALYSTS	48
4.1 Background / Literature Review	48
4.2 Experimental	54
4.3 Analysis	55
4.4 Results and Discussion	59
CHAPTER 5. DISCUSSION AND CONCLUSIONS	71
5.1 Reactor Experiments and Acid Site Characterization	71
5.2 Reaction Mechanisms	73
5.3 XAS Investigation of Metal-Doped CeO ₂ /Al ₂ O ₃ Catalysts	80
REFERENCES	82
APPENDIX A. GAS CHROMATOGRAPHY DETAILS	85

APPENDIX B. MASS BALANCE CALCULATIONS FOR REACTOR EXPERIMENTS AND GC CALIBRATION.....	86
APPENDIX C. DATA FROM REACTOR EXPERIMENTS AND ACID CHARACTERIZATION.....	90
VITA.....	106

LIST OF TABLES

2.1	Composition and BET surface area of catalysts used.....	16
3.1	Parameters used in the Weisz-Prater calculation for $\text{WO}_3/\text{Al}_2\text{O}_3$ and HZSM-5	22
3.2	Performance of $\text{La}_2\text{O}_3/\text{Al}_2\text{O}_3$ with increasing temperature from 340-400°C	28
3.3	Performance of $\text{La}_2\text{O}_3/\text{Al}_2\text{O}_3$ at 400°C with increasing feed ratio	28
3.4	Performance of WO_3/ZrO_2 at 360°C with increasing feed ratio.....	31
3.5	Performance of WO_3/ZrO_2 at 340°C with increasing feed ratio.....	31
3.6	Performance of $\gamma\text{-Al}_2\text{O}_3$ with increasing temperature from 340-400°C	34
3.7	Performance of $\gamma\text{-Al}_2\text{O}_3$ at 400°C with increasing feed ratio	34
3.8	Performance of HZSM-5 with increasing temperature from 340-400°C	37
3.9	Performance of HZSM-5 at 400°C with increasing feed ratio	37
3.10	Performance of $\text{WO}_3/\text{Al}_2\text{O}_3$ with increasing temperature from 340-400°C	41
3.11	Data for SAPO-18 with yield to hydrocarbons less than 10%.....	44
3.12	Data for AIPO-18.....	44
4.1	Experimental parameters for all XANES and EXAFS runs	56
4.2	Fitted EXAFS parameters for 0.8% Co catalyst.....	69
4.3	Fitted EXAFS parameters for 2.4% Co catalyst.....	70
A.1	GC settings for product analysis.....	85
A.2	Retention times for reactants and products.....	85
A.3	Response factors for reactants and products.....	85

LIST OF FIGURES

1.1	Adsorption of molecules on metal oxide and zeolite surfaces.....	3
1.2	Surface intermediates proposed for the formation of MT and DMS	5
2.1	Setup used in continuous flow reactor experiments	17
3.1	Yields and conversion on $\text{La}_2\text{O}_3/\text{Al}_2\text{O}_3$ versus yield to sulfur products at 340-400°C.....	29
3.2	Yield to DMS and MT versus methanol conversion on $\text{La}_2\text{O}_3/\text{Al}_2\text{O}_3$ at 340-400°C.....	29
3.3	Yields and conversion on WO_3/ZrO_2 versus yield to sulfur products at 340°C	33
3.4	Yield to DMS and MT versus methanol conversion on WO_3/ZrO_2 at 340°C.....	33
3.5	Yields and conversion on $\gamma\text{-Al}_2\text{O}_3$ versus yield to sulfur products at 340-400°C.....	36
3.6	Yield to MT and DMS versus methanol conversion on $\gamma\text{-Al}_2\text{O}_3$ at 340-400°C.....	36
3.7	Yields and conversion on HZSM-5 versus yield to sulfur products at 340-400°C.....	39
3.8	Yield to MT and DMS versus methanol conversion on HZSM-5 at 340-400°C.....	39
3.9	Yields and conversion on $\text{WO}_3/\text{Al}_2\text{O}_3$ versus yield to sulfur products at 340-400°C.....	40
3.10	Yield to MT and DMS versus methanol conversion on $\text{WO}_3/\text{Al}_2\text{O}_3$	40
3.11	Performance of $\text{MoO}_3/\text{SiO}_2$ at different temperatures	42
3.12	Concentration of acid sites determined by the desorption of propanamine in different temperature ranges	46
4.1	Ce L_{III} XANES spectra of CeO_2 and Ce_{III} acetate	50
4.2	Initial and final states of a Ce(IV) atom corresponding to an L_{III} transition.....	51
4.3	Normalized Ce L_{III} XANES of pure and doped catalysts at different stages of reduction	61
4.4	Normalized Ce L_{III} XANES of pure and doped $\text{CeO}_2/\text{Al}_2\text{O}_3$ catalysts reduced in 10% H_2/N_2 at 420°C for 15 min.....	61
4.5	Average number of oxygen vacancies around each cerium atom as determined by XANES using the Takahashi and WinXAS methods	62

4.6	XANES spectra at Co K-edge for cobalt containing CeO ₂ /Al ₂ O ₃ catalysts and standards	66
4.7	Pd L _{III} XANES of Pd/CeO ₂ /Al ₂ O ₃ catalyst and Pd standards, ambient conditions	66
4.8	EXAFS for Co K of 0.8% Co (top) and 2.4% Co (bottom) doped CeO ₂ /Al ₂ O ₃	67
4.9	Fourier transformed (k ² weighted magnitude and real parts) EXAFS for Co K of 0.8% Co (top) and 2.4% Co (bottom) doped CeO ₂ /Al ₂ O ₃	68
5.1	Illustration of the effect of surface acidity on the adsorption energy of methanol on LC/BC active sites	76
5.2	Steps of the proposed mechanism.....	77
5.3	Diagram showing the relations between paths 1-5 in the overall mechanism.....	78
5.4	Illustration of the effect of surface acidity on the activation barrier heights of paths leading to MT (1 or 2) and DMS (3).....	79

ABSTRACT

Metal oxide and zeolite catalysts were examined to determine their suitability for the production of methanethiol and dimethyl sulfide from the condensation of methanol and hydrogen sulfide. Fixed bed reactor experiments were used to test the catalysts in these processes. The acid sites of these catalysts were characterized by investigating the thermal desorption of 1-propanamine from these sites.

It was found that WO_3/ZrO_2 , $\text{La}_2\text{O}_3/\text{Al}_2\text{O}_3$, $\gamma\text{-Al}_2\text{O}_3$, and HZSM-5 catalysts were active and selective in the production of dimethyl sulfide. On these four catalysts, the reaction converting methanol to dimethyl ether and the methanethiol disproportionation reaction were fast and close to equilibrium. The yield to dimethyl ether was high at short contact times and decreased with increased contact time. The $\text{WO}_3/\text{Al}_2\text{O}_3$ catalyst was less active than these four, but was selective to methanethiol. For these catalysts, the selectivity to sulfur products did not decrease as the methanol partial pressure varied over orders of magnitude, indicating that the sulfidation reactions are close to zero order in methanol. The $\text{MoO}_3/\text{SiO}_2$, $\text{TiO}_2/\text{SiO}_2$, SAPO-18, and AIPO-18 catalysts were not suitable for production of either product due to low activity or selectivity.

Acid site characterization experiments showed that sites desorbing 1-propanamine and its reaction products at temperatures between 300 and 350°C were the most active in the sulfidation of methanol. Based on this work and results in the literature, a mechanism was proposed that correlates methanethiol selectivity to catalyst acid strength.

In additional work, X-ray absorption spectroscopy was used to characterize metal doped $\text{CeO}_2/\text{Al}_2\text{O}_3$ catalysts active for the condensation of carboxylic acids to ketones. No general correlation was found between the number of oxygen vacancies measured by Ce L_{III} XANES and

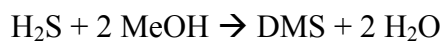
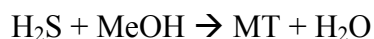
the activity of a catalyst for this reaction. It was found by Co K edge XANES and EXAFS that cobalt atoms doped into this catalyst are substituted for cerium atoms in the CeO₂ lattice and are coordinated tetrahedrally by four oxygen atoms. Pd L_{III} edge XANES showed that palladium doped into the CeO₂/Al₂O₃ catalyst mostly dissolves in the CeO₂ lattice in a highly ionic state.

CHAPTER 1

INTRODUCTION AND REVIEW OF LITERATURE

1.1 Goals and Project Summary

Dimethyl sulfide (DMS) and methanethiol (MT) are produced by the condensation of hydrogen sulfide with methanol (MeOH) over a metal oxide or zeolite catalyst. The general reactions are:



In addition to forming sulfur product (DMS and MT), methanol condenses to dimethyl ether (DME) and can react to other minor byproducts.

Methanethiol is used to produce methionine which is used as a feed additive and in pharmaceutical production. Dimethyl sulfide is used to produce dimethyl sulfoxide which is used as a solvent and in pharmaceutical production (Mashkin et al., 1995).

The aim of this project is to identify zeolite and metal oxide catalysts that are suitable for the production of either DMS or MT and then find optimal sets of reaction parameters. Properties used to determine the suitability of catalysts included activity, selectivity toward desired products, deactivation and regeneration of the catalyst, and whether or not the side products could be recycled. Reactor parameters that were optimized for each catalyst were temperature, space velocity, and feed ratio of methanol to hydrogen sulfide. Finally, a mechanism is proposed to explain trends in the effects of catalyst acid strength on the reactivities and selectivities found in the literature and in this work.

1.2 Reaction Chemistry on Zeolite and Metal Oxide Catalysts

It is known that the active sites on metal oxide and zeolite catalysts consist of Lewis acid centers (LCs), protic centers (PCs), and basic centers (BCs) (Gates, 1992). On metal oxides, the strength of all three of these sites is mainly determined by the amount of hybridization between electronic levels on oxygen and metal sublattices, which increases with the electronegativity of the metal cation (Henrich and Cox, 1994). The position of the top of the surface valence band determines the strength of BCs and PCs. The higher this energy, the more strongly these electrons interact with unoccupied orbitals on other atoms and molecules, increasing the basicity. The lower this energy, the weaker the surface binds hydrogen atoms, causing the Bronsted acidity to increase. Greater hybridization between oxygen and metal atoms decreases the level of this band. LCs are formed when two PCs interact, resulting in the formation of water and leaving an exposed cation. When this happens, a low energy unoccupied orbital forms on the cation, which can interact with occupied orbitals on reactant molecules. The greater the extent of hybridization, the lower this orbital lies in energy and the stronger the LC is. As the Lewis acidity increases, the number of the sites usually decreases since more energy is required for their formation.

The primary molecules involved in methanol condensation reactions are MeOH, DME, MT, DMS, H₂S, and H₂O. Through interaction with the surface, reactive acidic and basic groups on these molecules are formed which participate in the acid-base reactions that define the overall mechanism (Mashkina et al., 1988). An example of such species is shown in Figure 1.1 (a) where the methyl group and hydrogen atom on a MeOH molecule are activated by the interaction of the oxygen with an acidic site on the surface (Gates, 1992). These acidic groups can transfer to another molecule by interacting with one of its basic groups. An example of a basic group is

also shown in Figure 1.1 (a) where the methoxy group in a molecule of MeOH is activated when the hydrogen atom interacts with a surface BC. An example of a surface reaction proceeding by this mechanism is the formation of DME from two activated MeOH molecules shown in Figure 1.1 (b). It should be noted that C-S bonds are not significantly activated by the interaction of the sulfur atom with a PC (Mashkina et al., 1991).

The molecules involved in the reaction can also chemisorb onto LCs and BCs, forming methoxy, mercaptide, and sulfide groups [Figure 1.1 (c)] that can react as acids or bases with each other or with other activated molecules (Mashkina et al., 1988).

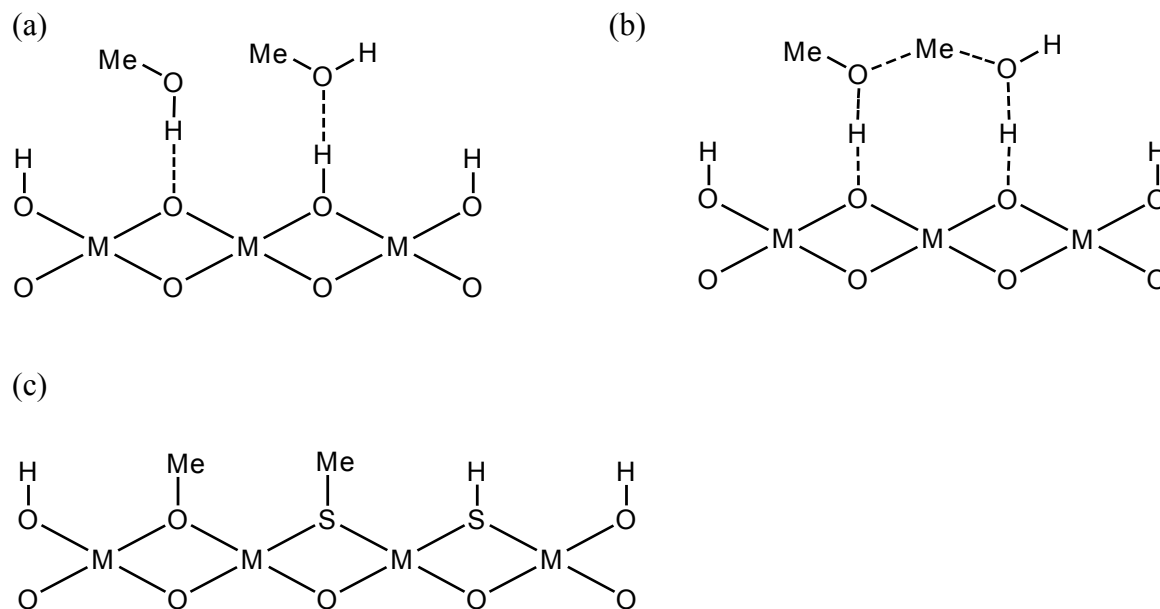


Figure 1.1. Adsorption of molecules on metal oxide and zeolite surfaces. Acidic and basic sites on the surface can (a) interact with corresponding moieties of the reactant molecules. These activated molecules can then exchange groups with each other (b) to form in this case DME and H₂O. Reactants can also chemisorb onto LCs (c) to form methoxy, mercaptide, and sulfide groups.

The catalytic sites in zeolitic materials are similar to those on metal oxides (Mashkina, 1991). The same principles govern the strength of BCs, PCs, and LCs and their reactivity. In addition, the amount of aluminum in T-positions has a large impact on the strength of the PCs

(Kubelkova et al., 1989; Rabo and Gajda, 1989). As more aluminum is incorporated into the lattice, the energy of the valence band increases since aluminum is a less electronegative element than silicon. This raises the basicity of the surface; the protons are more strongly bound. Thus as the number of PCs increases, their strength decreases. Another characteristic unique to zeolites is that the protons can be exchanged for cations that can serve as LCs (Ziolek et al., 1998). As the basicity of the cation increases, the PC strength decreases (Kubelkova et al., 1989).

1.3 Reaction Mechanisms

Several mechanisms have been proposed in the literature for the reactions between methanol and H₂S on metal oxide and zeolite surfaces. Mashkina et al. (1988) propose a serial mechanism for metal oxides by which surface methyl and bisulfide (HS-LC) species interact to form MT, which then desorbs. MT can then chemisorb on LCs and react with a methyl species to form DMS. These reactions are



and are shown in Figure 1.2 (a). The ratio between the rates of MT and DMS formation will depend on the basicity of the two reactants. Since MT is more basic than H₂S, it will preferentially chemisorb on LCs and react with methoxy groups. The disproportionation of MT to DMS occurs by the reaction



and occurs on strong acid sites such as LCs. Mashkin et al. (1995) provide further evidence for this mechanism and also propose that DME is formed when surface methyl or methoxy species interact with each other or with gas phase methanol.

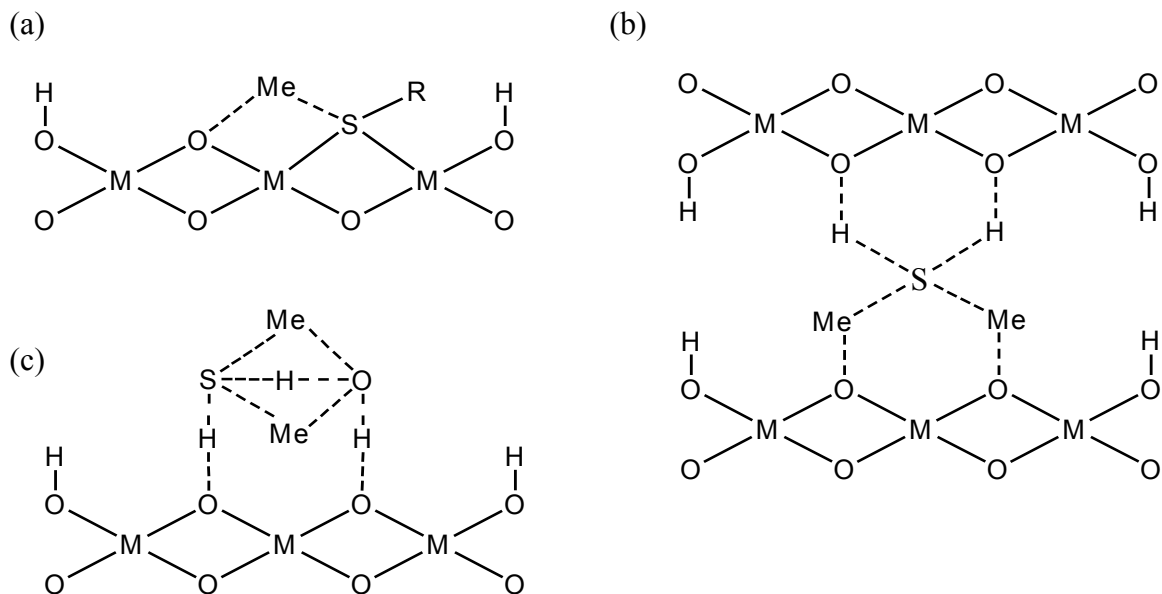


Figure 1.2. Surface intermediates proposed for the formation of MT and DMS between (a) surface methyl and sulfur species (R is H or Me), (b) surface methyl and activated H₂S and (c) activated DME and H₂S.

Ziolek et al. (1993) examined metal oxides of varying acidity and concluded that DMS selectivity (vs. MT) increases with the cation charge as predicted by the Sanderson electronegativity scale. The thermal stability of dissociatively adsorbed methanol is highest for strongly basic and strongly acidic surfaces and is lowest for amphoteric surfaces such as alumina and titania; but the activity for sulfur products is highest for the latter. Surface methyl species can interact with both chemisorbed bisulfide and mercaptide as well as activated H₂S and MT.

A parallel mechanism is proposed for zeolites (Mashkina et al., 1991; Mashkina and Yakovleva, 1991), in which surface methyl species react with chemisorbed bisulfide to form MT as in (1), or with activated H₂S to form DMS according to



and shown in Figure 1.2 (b). They found that the reaction of MT with methanol in (2) is insignificant, and (3) is faster than either (1) or (4). They claim that MT can dissociate on a

conjugate LC-BC pair to form a methyl group and H₂S, however, this seems unlikely except on extremely basic catalysts due to the much higher strength of the C-S bond that is broken compared to the C-O bond that forms.

Ziolek et al. (1998) propose that MT is formed by (1) and DMS is formed by the reaction of DME with H₂S, with the participation of PCs and BCs as shown in Figure 1.2 (c). No convincing experimental evidence is offered for this mechanism.

1.4 Trends in Reactivity and Selectivity

There are examples in the literature where metal oxide catalysts with acidic and basic sites of a wide variety of strengths are characterized and evaluated for the synthesis of DMS and MT. The studies show the dominant reaction pathways that are followed on different materials and under different conditions, and what effect these pathways have on catalyst activity and product distribution.

Mashkina et al. (1988) investigated metal oxide supports (silica, silica-alumina, alumina) pure and doped. Their silica was the most inert support studied, having no BCs or LCs and only weak PCs with PA (proton affinity) = 1390 kJ/mol. This support showed very little activity in the reaction of MeOH with H₂S, only converting MeOH at a rate of 6 μmol/m²-h to mainly DME (31% sulfur product selectivity). Doping the support with 30% H₃PO₄ produces strong PCs with PA < 1300 kJ/mol. This increases the specific activity by a factor of four and exclusively produces DME, suggesting that while PCs can weakly activate MeOH they cannot activate H₂S. In MASNMR studies (Nosov et al., 1991), methanol was not found to dissociate on silica, however Me-O-P species were found on the phosphated support. Similar studies (Mastikhin et al., 1989) found no evidence of dissociated H₂S on either catalyst.

When the authors doped the silica with MoO₃ or WO₃, the activity to sulfur products increased by more than an order of magnitude when compared to pure silica. While a large quantity of strong PCs was detected on the MoO₃-doped catalyst, no other active sites were found by CO adsorption. However, pyridine adsorption detected a large quantity of LCs of unspecified strength on the WO₃-doped catalyst. Increasing the concentration of the transition metal oxide increases the activity to sulfur products and the selectivity to DMS over MT.

They also found silica-supported heteropolyacids to be somewhat active in MT and DMS production. Supporting 9.4% phosphotungstic acid creates LCs of $Q_{CO} = 28$ kJ/mol (heat of adsorption for CO) in addition to strong PCs. The activity for sulfur products is 9 $\mu\text{mol}/\text{m}^2\text{-hr}$, indicating that these weak LCs have some ability to chemisorb H₂S, however the selectivity to these products is only 14%. Supporting 7.5% silicotungstic acid gives LCs similar to those in phosphotungstic acid, and additionally gives a few strong LCs with $Q_{CO} = 46$ kJ/mol. These sites increase the rate of formation of sulfur products by a factor of six, while completely suppressing DME production.

Mashkina et al. (1988) found that adding alumina to the silica support decreases the binding energy of surface oxygen and allows a few strong LCs to form with $Q_{CO} = 56$ kJ/mol. Additionally, a large number of strong PCs appear that are associated with hydroxyl species bridging aluminum and silicon atoms on the surface. These PCs are weaker than those found in many zeolites due to a weaker Al-O bond (Rabo and Gajda, 1989). While the PCs seem to catalyze the reaction to DME (32% selective), the selectivity for DMS (vs. MT) is quite high with the former making up 91% of the sulfur products.

Addition of 7% WO₃ to this support increases the number of PCs and decreases the number of LCs both by a factor of two, although the LC strength does not change. The activity

to DME doubles, in close agreement with a pathway dominated by PCs. The activity to sulfur products increases by an order of magnitude and yields a nearly equal mixture of MT and DMS.

The last supports studied, γ -alumina and η -alumina, were two orders of magnitude more active for sulfur products than silica supports. Being a more electropositive element, alumina contains large quantities of weaker LCs ($Q_{CO} = 34$ kJ/mol), but also a substantial number of stronger LCs ($Q_{CO} = 41$ kJ/mol). Equal amounts of MT and DMS are produced. Eta alumina is similar to gamma alumina except that the stronger LCs have a Q_{CO} of 56 kJ/mol. This results in the activity to sulfur products doubling and the selectivity to DMS (vs. MT) increasing to 63%. MASNMR (Mastikhin et al., 1989) found evidence of H_2S dissociation on $\gamma-Al_2O_3$ to form bisulfide surface species.

Doping the γ -alumina support with various transition metal oxides had only a slight effect on the activity and selectivity. Adding various amounts of Cr_2O_3 increased the activity to sulfur products and the selectivity to DMS, while adding V_2O_5 or WO_3 increased the selectivity to MT. Doping with 3% HF produced the most active catalyst, with an initial activity to sulfur products of $4900 \mu\text{mol}/\text{m}^2\text{-hr}$, but it deactivated rapidly. MASNMR (Mastikhin et al., 1989) showed that doping γ -alumina with Na^+ and K^+ had little effect on the dissociation of H_2S , but F^- inhibited this process and left more electron density on the H-atom in adsorbed bisulfide.

Ziolek et al. (1993) found basic metal oxide surfaces such as MgO, $MgAl_2O_4$, TiO_2 rutile, and ZrO_2 to be highly selective to MT vs. DMS (>90% selectivity). Activity was lower than for the aluminas and decreased in the order $MgO \ll MgAl_2O_4 < TiO_2 \sim ZrO_2$. CeO_2 was also very selective to MT vs. DMS but was also highly selective to methane. Additional studies (Ziolek et al., 1995) showed that H_2S dissociates completely to sulfide on MgO and ZrO_2 and to bisulfide

on TiO₂ rutile. Dissociative adsorption does not occur on anatase and this catalyst shows higher activity and DMS selectivity than rutile (40% selectivity to DMS vs. MT).

Mashkin et al. (1995) found that WO₃/Al₂O₃ was selective to DMS and K₂O/WO₃/Al₂O₃ was selective to MT at 360°C. The first catalyst has moderately strong LCs ($Q_{CO} = 36$ kJ/mol) that disappear when potassium is added. Runs were also conducted using DME in the place of MeOH and similar results were obtained. As the temperature increased from 360 to 500°C, the selectivity to DMS increased and that for MT decreased on the K-doped catalyst, supporting a mechanism in which formation of DMS has a higher activation energy than MT. No DMS is produced at short contact times on WO₃/Al₂O₃, indicating that DMS is formed as a secondary product from MT. Furthermore, MT yield goes through a maximum and then decreases at longer contact times upon conversion to DMS. When MT and MeOH were fed to the reactor, WO₃/Al₂O₃ was active to DMS but K/WO₃/Al₂O₃ was not.

Several deprotonated X and Y zeolites were characterized by Ziolk et al. (1998) containing different cations from the alkali series. Activity was lower than for the protonated forms and selectivity to MT was around 90%. Due to the lack of surface protons, water cannot desorb to form LCs associated with the silicon and aluminum atoms. Instead, weak LCs ($Q_{CO} \sim 20$ kJ/mol) due to the interaction of cations and BCs terminating the surface are the active species in the reaction. On zeolite X, H₂S likely dissociates over a LC and a BC to form a PC that can aid in chemisorption of MeOH onto a BC, giving off H₂O. The activity has a strong dependence on the cation, being highest for the larger cations.

When deprotonated Y zeolites were applied in a similar fashion, the cation had little impact on activity or selectivity, and the activity was less than that on zeolite X. Fewer M-SH groups were found on NaY than on NaX (Nosov et al., 1991), and this number increased with

basicity of the cation on MNaY (Ziolek et al., 1998). Going from Li – Rb, the activity in the absence of H₂S decreased slightly, so a more acidic surface may be better at dissociating MeOH. This same trend in activity occurred when H₂S was present, indicating that chemisorption of MeOH may be the rate determining step here.

When the cations in Y zeolites were partially exchanged for NH₄⁺, the activity increases significantly and the selectivity shifts to DMS. As the acidity of the cation decreases, the activity to sulfur products and the selectivity to MT vs. DMS both increase. On these catalysts, strong LCs are present (Q_{CO} = 55 kJ/mol for HNaY, Mashkina et al. 1988), and these probably activate H₂S dissociation. LiHNaY and NaHY, as well as HNaX, were selective to hydrocarbons but the other zeolites examined were not. Comparing the zeolites containing K – Cs, the activity and selectivity to MT increased with the basicity of the cation. When additional Cs₂O is added to the CsHNaY zeolite, the selectivity to MT increases to > 90% and the activity decreases.

Another study (Mashkina et al., 1991; Mashkina and Yakovleva, 1991) compares the rate of formation of DMS on NaX, NaY, HNaY, and HZSM-5 at 360C. As found by Ziolek et al. (1998), NaY and NaX were selective to MT and NaY was less active than NaX. HNaY was found to be more active than NaY for sulfur products and was selective to DME and DMS. HZSM-5, which is known to have strong PCs (PA ~1200 kJ/mol) and LCs, was an order of magnitude more active than the others and was 85% selective to DMS. For all of these zeolites, the ratio of MT to DMS being produced was constant up to 60% methanol conversion. These catalysts were also examined for the disproportionation reaction of MT to DMS and H₂S by feeding pure MT into the reactor. For all zeolites, the rate of DMS formation with this feed was higher than the rate of its formation when the feed consisted of H₂S and MeOH.

MASNMR studies (Nosov et al., 1991; Mastikhin et al., 1989) characterized the surface species found on NaX, NaY, and HZSM-5. In the absence of H₂S, methanol dissociates on HZSM-5 but not on NaX and NaY. Dissociation of H₂S occurs on NaX and to a lesser extent on NaY with participation of Na⁺ cations, indicating that cations in the SIII sites of NaX are more accessible. Dissociation occurs on HZSM-5 at moderately strong LCs, possibly due to extraframework aluminum sites.

Ziolek et al. (1998) studied the catalytic properties of MCM-41 doped with aluminum and niobium for this reaction at 350°C. HAl-MCM-41 had more and stronger PCs than HNb-MCM-41, while the latter had more LCs. As expected, activity was highest for HAl-MCM-41 and decreased as niobium was added while selectivity to MT vs. DMS followed the opposite trend.

Paskach et al. (2002) studied Mo₆S₈ clusters existing as various phases and found that amorphous ternary molybdenum sulfides were fairly selective to MT (70 – 80%). Of the systems studied, La(Mo₆S₈)S_{1.5} was the most selective to MT and Ho(Mo₆S₈)S_{1.5} was the most active. Side products included the usual DMS and DME along with CO, CO₂, COS and CS₂.

1.5 Ab-Initio Calculations

In developing a reaction mechanism in this work, ab-initio electronic quantum mechanical calculations were performed on various molecular species using the Gaussian 03 package (Frisch et al., 2004). This package solves the time-independent electronic Schrodinger equation in a basis set of Gaussian atomic orbitals using the independent electron approximation augmented by gradient corrected density functional theory.

The exact time-independent electronic Schrodinger equation is a second order partial differential equation over the spatial coordinates of all electrons in the system and is given by

$$-\frac{\hbar^2}{2m}\nabla^2\psi + V\psi = E\psi$$

where ψ is the time-dependent electronic wave function with $3N$ independent arguments where N is the number of electrons in the system (Cramer, 2002). The mass of an electron is m , V is the potential energy of a particular configuration of the N electrons, E is the energy of the wave function, and ∇^2 is the Laplacian over all $3N$ electronic coordinates. Since most systems of interest have on the order of 100 electrons, their would be 300 degrees of freedom, making the solution of this equation impractical. Instead, an independent Schrodinger equation is solved for each electron moving in the average electrostatic potential of the other electrons. This is called the independent electron approximation of the Schrodinger equation.

The independent electron approximation, however, overestimates the electrostatic repulsion of the electrons, because the electrons tend to avoid each other in order to minimize this repulsion (Cramer, 2002). Therefore, the binding energy of the system calculated by this method will be higher than the actual binding energy by an amount called the correlation energy. In order to partially correct for this error, the correlation energy is approximated assuming that it is a function of the electron density. This approximation is called local density functional theory, and assumes the correlation energy at a particular point in space is the same as the correlation energy of a uniform electron gas having the density of the actual system at that point. Further corrections (gradient corrections) are applied that take into account not only the electron density at a particular point in space but also its gradient.

Even with the independent electron approximation, it is not computationally practical to solve the Schrodinger equation using finite difference methods (Cramer, 2002). The equation is instead solved within a finite function space of n Gaussian basis functions, each centered at an

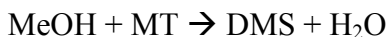
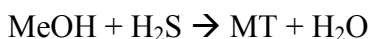
atom in the system. The basis functions centered on a particular atom are similar in form to the analytic hydrogenic wave functions. By using a basis set such as this, the partial differential equation is converted to a set of n nonlinear algebraic equations that can be solved using an iterative method.

The most common basis sets and density functionals along with the average errors in computed energies associated with them are discussed by Foresman and Frisch (1996). Calculations in the present work are performed using the 6-311+G(d) basis set with the B3LYP density functional. Average deviations in computed energy vs. actual energy for this method are about 10 kJ/mol. All of the conclusions drawn from these calculations are insensitive to this amount of error.

1.6 Summary of Literature Review and Proposed Study

The following conclusions can be drawn from a study of the literature pertaining to production of MT and DMS from methanol and H₂S, using metal oxide and zeolite catalysts:

- Alumina-based mixed metal oxide and zeolite catalysts are active in the formation of MT and DMS from methanol and H₂S. Zirconia and titania are also active for these reactions.
- The following reactions occur on these catalysts:



- Reactant and product molecules interact weakly with PCs and BCs on the catalyst surface and dissociatively adsorb on LC/BC pairs

- Metal oxides with moderate acid strength such as alumina are the most active catalysts for these reactions. Much more acidic or more basic catalysts such as MgO and $\text{PO}_4^{3-}/\text{SiO}_2$ are nearly inactive.
- Basic metal oxides are selective to MT and acidic metal oxides are selective to DMS.
- H-form X and Y zeolites are active in the formation of MT and DMS. The deprotonated forms of these zeolites are much less active. HZSM-5 is the most active zeolite for these reactions.
- Disproportionation of MT is faster than the reaction between methanol and H_2S on zeolites.

Based on the study of the literature, the following study is proposed for this work.

- Use fixed bed reactor experiments to determine the suitability of mixed metal oxide and zeolite catalysts for the production of either MT or DMS from methanol and H_2S at high methanol conversion. Determine optimum reactor conditions – temperature, space velocity, and feed ratio of methanol to H_2S – and study the deactivation of these catalysts.
- Use thermal desorption experiments to determine the concentration and strength of acid sites on these catalysts.
- Propose a mechanism that correlates activity and product distribution to the strength of acid sites on the catalysts studied in this work and in the literature.

CHAPTER 2

EXPERIMENTAL

2.1 Catalyst Preparation

In this work ten different catalysts were used, whose properties are given in Table 2.1. $\text{La}_2\text{O}_3/\text{Al}_2\text{O}_3$, Al_2O_3 , and $\text{TiO}_2/\text{SiO}_2$ were acquired from Davison Catalysts as Davicat® AL 2400, Davicat® AL 2100, and Davicat® SITI 4350. AIPO-18 and SAPO-18 were synthesized hydrothermally by the method of Chen et al. (Chen et al., 1994). The 15% WO_3/ZrO_2 catalyst was provided by ExxonMobil and was prepared by incipient wetness impregnation (IWI). The 10% $\text{MoO}_3/\text{SiO}_2$ stabilized with $< 1\%$ K_2O was provided by Ferro and prepared by IWI. The HZSM-5 is an MFI zeolite (Si/Al ratio of 21.5); it was provided by PQ Corp. and was characterized by Dooley et al. (1996).

The 10% $\text{WO}_3/\text{Al}_2\text{O}_3$ catalyst was prepared by IWI from Conoco Catapal alumina using a 22 wt.% $\text{Na}_2\text{WO}_4 \cdot 2\text{H}_2\text{O}$ solution. After IWI the solid product was reacted at reflux with 1.5 times excess concentrated HCl, added dropwise. The reaction $\text{Na}_2\text{WO}_4 \cdot 2\text{H}_2\text{O} + 2 \text{HCl} \rightarrow \text{WO}_3 + 3 \text{H}_2\text{O} + 2 \text{NaCl}$ will take place under these conditions. An excess of 5% NH_4NO_3 was then added to react any excess HCl to NH_4Cl , and the solid thoroughly washed with DI water followed by drying at 120°C .

2.2 Continuous Flow Reactor Experiments

All reactions were carried out in a fixed bed reactor contained in an 18 cm length of 1/2 in stainless steel tubing as shown in Figure 2.1. The reactor was loaded with 1.5 – 2.5 g of catalyst packed between two layers of glass beads and quartz wool and was operated in downflow mode. Heating was applied through an external clamshell furnace powered through a Eurotherm power controller. The relay received input from a Eurotherm 818-P PID temperature

controller that measured the temperature of the catalyst bed via a K thermocouple inserted into its center. Pure methanol was fed by a Sage Instrument 341A syringe pump into a vaporizer where it was mixed with 12% H₂S/N₂ at 200°C. The vaporizer consisted of 18 cm of 1/2 in stainless steel tubing filled with glass beads held in place by quartz wool. The vaporizer was wrapped with electrical heating tape, under which a J thermocouple was inserted connected to an Omega digital readout. Methanol was injected into one end of the vaporizer by a needle protruding into the bed of glass beads. The effluent was carried through 1/8 in stainless steel tubing wrapped in electrical heating tape kept at 170°C as measured by a J thermocouple 38 cm downstream from the reactor exit.

Table 2.1. Composition and BET surface area of catalysts used.

Composition	Surface Area (m ² /g)
γ-Al ₂ O ₃	170
4% La ₂ O ₃ /Al ₂ O ₃ (Boehmite)	325
3% TiO ₂ /SiO ₂	350
15% WO ₃ /ZrO ₂	78
10% WO ₃ /Al ₂ O ₃	161
<1% K ₂ O/10% MoO ₃ /SiO ₂	243
HZSM-5 (Si/Al = 21.5)	443
SAPO-18 (Al/Si = 10)	466
AlPO-18	466 *

* Assumed to have a surface area equal to that of SAPO-18

Either H₂S/N₂, N₂, or air could be selected by two three-way valves as the gas going to the reactor. When a reaction was not being run, N₂ was passed through the reactor. Air was used to regenerate the catalyst.

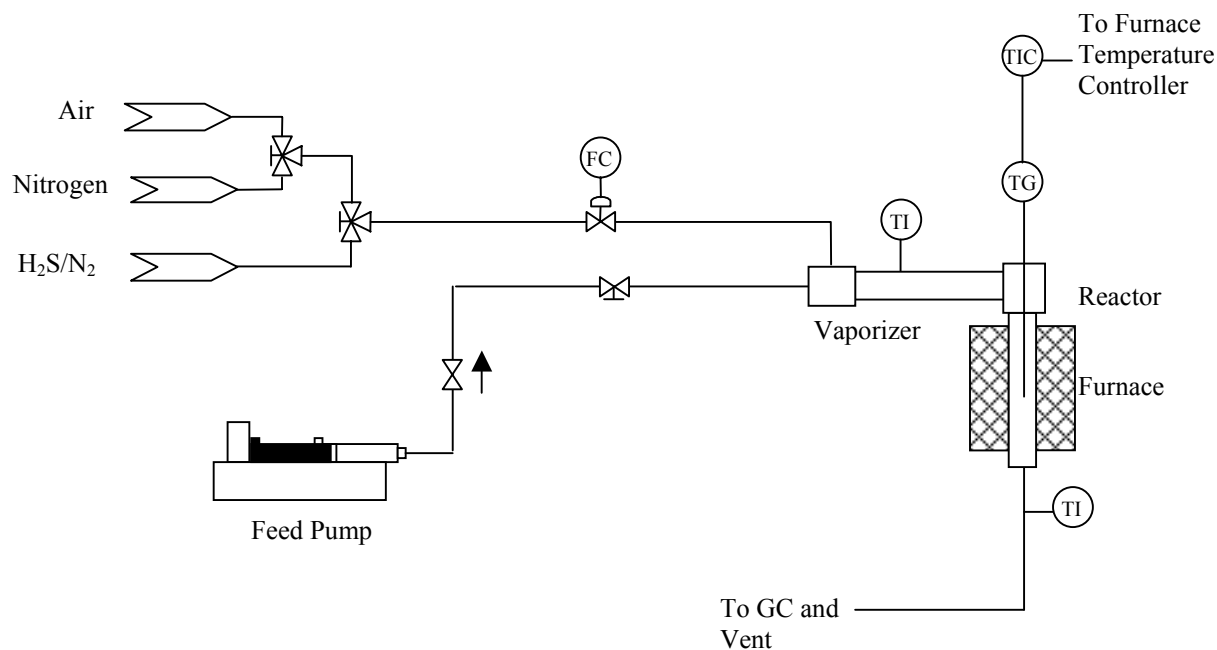


Figure 2.1. Setup used in continuous flow reactor experiments.

In these experiments, the weight hourly space velocity of methanol (WHSV) was varied between 0.07-1.6 g/h-g cat., with a molar feed ratio of methanol to H₂S ranging from 0.3-2.2. The reactor bed temperature was varied from 360-400°C and the pressure at its inlet was 1.3-1.7 bar. Catalysts were calcined in nitrogen or air at 400-500°C and regenerated in air at 450-500°C.

The effluent passed through heated tubing to an automatic injection valve (1 mL sample loop) on a HP 5890 Series II GC heated to 120°C. The column used was a Zebron ZB-1 (0.32 mm ID, 30 m length) and a flame ionization detector (FID) was used. Gas samples could also be manually injected into a Hewlett-Packard HP-5MS column (0.25 mm ID, 30 m length) and

analyzed by a HP 5972 mass selective detector (MSD). Details of GC runs are contained in Appendix A.

Since an FID was used to quantify the product composition, the nitrogen, water, and hydrogen sulfide that make up a large part of the stream could not be detected. It was therefore necessary to calibrate the GC response based on the absolute amount of compound contained in the injection volume. Methanol was calibrated by sampling a stream of methanol and nitrogen with known composition. The calibration for DMS was performed by introducing an excess of methanol with H₂S through the reactor at 400°C in the presence of La₂O₃/Al₂O₃ so that all of the H₂S was converted to DMS. A GC analysis was taken, along with an MS scan to confirm that all of the H₂S had reacted to form DMS. Using mass balances detailed in Appendix B, the GC response factor (mole fraction/area based on sample loop volume) for DMS could be calculated from this GC run. The same procedure was repeated in the presence of WO₃/Al₂O₃ and an excess of H₂S to determine the response factor for MT. To determine the response factor for DME, a stream of methanol and nitrogen was passed through the reactor loaded with La₂O₃/Al₂O₃ at 400°C and sampled by the GC. Due to the difficulty in deconvoluting methanol and DME peaks in the FID response, it was assumed that the reaction producing DME came to equilibrium.

2.3 Catalyst Characterization

The acidic properties of the catalysts were characterized by thermal analysis of n-propanamine (n-PA) desorption using the method of Kanazirev et al. (1994). A Perkin-Elmer TGA7 microbalance was used to detect weight change upon thermal treatment of the catalysts in He or a mixture of He and n-PA. Ten to 15 mg of sample was weighed out in the platinum microbalance pan and dried in 50 cm³/min He flow via temperature programming from 50-

400°C at 10°C/min with a final hold of 10 min or more. The sample was then rapidly cooled to 50°C and exposed to PA until saturated by bubbling 50 cm³/min He through the liquid at ambient temperature. The bubbler was then bypassed and the sample was purged with pure He for 10 min at 50°C. Thermal gravimetric analysis was then performed by linearly varying the temperature from 50-550°C at 5°C/min.

CHAPTER 3

RESULTS

3.1 Continuous Flow Reactor Experiments

3.1.1 Calculations

Complete data sets for all reaction experiments are given in Appendix C. The terminology used to describe the results here and in the spreadsheets is as follows:

- Methanol conversion = $100 \times (\text{mol MeOH reacted})/(\text{mol MeOH fed})$
- H₂S conversion = $100 \times (\text{mol H}_2\text{S reacted})/(\text{mol H}_2\text{S fed})$
- MT Yield = $100 \times (\text{mol MeOH that form MT})/(\text{mol MeOH fed})$
- DMS Yield = $100 \times (\text{mol MeOH that form DMS})/(\text{mol MeOH fed})$
- DME Yield = $100 \times (\text{mol MeOH that form DME})/(\text{mol MeOH fed})$
- Sulfur product (SP) Yield = MT Yield + DMS Yield
- MT (DMS) Selectivity = $(\text{MT (DMS) Yield})/(\text{SP Yield})$
- WHSV = $(\text{weight MeOH fed hourly})/(\text{weight of dry catalyst})$
- Space velocity = $(\text{mol MeOH fed hourly})/(\text{BET surface area of catalyst})$

The amount of methanol fed to the reactor was calculated using a carbon mass balance based on the composition of the product stream. Hydrogen sulfide could not be analyzed by the FID, so an indirect method was required to calculate its conversion. Knowing the amount of sulfur entering the reactor as H₂S and the amount leaving as DMS and MT, the sulfur mass balance could be closed to calculate the amount of H₂S leaving the reactor. The equations used for determining the feed ratio and the H₂S conversion are given in Appendix B. Since the concentrations measured by the FID were only accurate to within a few percent, this method of

calculating the H₂S leaving the reactor was not reliable at high H₂S conversion and in a few cases an H₂S conversion greater than 100% was calculated.

To determine if the reaction rate was limited by intra-particle diffusion, a calculation using the Weisz-Prater method was performed on the two catalysts where diffusion resistance was most likely – WO₃/Al₂O₃ because it had the largest particle size and HZSM-5 because it had the smallest pore size. The Weisz-Prater parameter, C_{PW} , estimates the ratio of the reaction rate to a characteristic diffusion rate and is given by

$$C_{PW} = \frac{-r_A \cdot \rho_p \cdot R_p^2}{D_e \cdot C_{As}}$$

where $(-r_A)$ is the rate of consumption of reactant A , R_p is the radius of the catalyst particle, ρ_p is the density of the catalyst particle, C_{As} is the concentration of A at the catalyst particle surface, and D_e is an effective diffusivity for A in the catalyst particle given by

$$D_{eA} = \frac{D_A \cdot \phi_p}{\tau}$$

where ϕ_p is the porosity and τ is the tortuosity of the catalyst particle, and D_A is the actual diffusivity of A in the catalyst pores calculated from the molecular diffusivity, D_{AM} , and the Knudsen diffusivity, D_{AK} by

$$\frac{1}{D_A} = \frac{1}{D_{AM}} + \frac{1}{D_{AK}}$$

Since the gas consists of about 80% N₂, the binary diffusivity of methanol in air at 400°C can be used [0.6 cm²/s (Perry et al., 1997)]. As seen below, the molecular diffusivity is more than an order of magnitude larger than the Knudsen diffusivity, so D_A can be approximated by the latter.

The Knudsen diffusivity is calculated by

$$D_{AK} = \frac{2}{3} \cdot d_{pore} \cdot \sqrt{\frac{2RT}{\pi M_A}}$$

where d_{pore} is the pore diameter and M_A is the molecular weight of A .

The parameters used for both catalysts are given in Table 3.1 along with the calculated Weisz-Prater parameter. For both catalysts, the Weisz-Prater parameter is much less than unity, indicating that the diffusive resistance has a negligible effect on reaction rate. The other metal oxide catalysts have particle diameters much smaller than WO_3/Al_2O_3 , so diffusive resistance will be negligible for them also.

Table 3.1. Parameters used in the Weisz-Prater calculation for WO_3/Al_2O_3 and HZSM-5

	WO_3/Al_2O_3	HZSM-5
$(-r_A)$ (mol/g-s) x 10^7	3.2	1.8
ρ_p (g/cm ³)	1.0	1.8
R_p (μ m)	1700	150
d_{pore} (nm)	8.0	0.54
C_{As} (mol/L)	0.18	0.17
D_e (cm ² /s)	3.9×10^{-3}	1.2×10^{-4}
D_{AK} (cm ² /s)	1.8×10^{-2}	1.2×10^{-3}
τ	3	3
ϕ_p	0.65	0.30
C_{WP}	3×10^{-3}	9×10^{-4}

In order to determine whether the MT disproportionation reaction proceeded in the forward or reverse direction near the reactor exit, the affinity A was determined for each run based on product composition and reactor temperature. The affinity (Boudart, 1986) is given by

$$A = \frac{-\Delta G}{RT} = \ln\left(\frac{K}{Q}\right)$$

where K is the equilibrium constant of the disproportionation reaction at the reactor temperature, ΔG is the change in Gibbs free energy for the reaction, and Q is defined as

$$Q = \frac{x_{DMS} \cdot x_{H_2S}}{x_{MT}^2}$$

where x is the mole fraction of the respective component in the product stream. The relationship between affinity and net reaction rate is

$$\frac{\vec{v}}{\bar{v}} = \exp(A)$$

where v is the turnover frequency (reaction rate specific to number of active sites) in the forward and reverse directions as indicated by the arrows. Therefore, if the affinity is positive, the reaction is proceeding in the forward direction to produce DMS near the exit of the reactor. The values of K at 340°C and 400°C are 3.45 and 3.14. All thermodynamic properties used in these calculations were taken from the HYSYS Plant 2000 database (Hyprotech Ltd., 2000). At high conversions of H_2S , the relative error in its measured concentration can be quite high due to the indirect method of measuring it, resulting in a large error in the calculated affinity.

The affinity can also be calculated for the dehydration of methanol to DME, with Q defined as

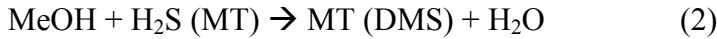
$$Q = \frac{x_{DME} \cdot x_{H_2O}}{x_{MeOH}^2}$$

and with an equilibrium constant of 6.89 at 340°C and 4.93 at 400°C. If the affinity is positive, the formation of DME is favored.

A calculation can be performed in which the yield to sulfur products is fixed and the methanol, water, and DME are brought to equilibrium. This calculation will give the conversion of methanol and the yield of DME if the reaction that forms DME from methanol is fast compared to reactions that form sulfur products. The equilibrium mole fractions for this reaction are given by

$$K_1 = \frac{x_{DME} \cdot x_{H_2O}}{x_{MeOH}^2}$$

where K_1 is the equilibrium constant for reaction 1 given below. The two reactions involved in this calculation are



where the second reaction encompasses the reactions of methanol with both H_2S and MT. Since all important reactions are equimolar, mole fractions can be used instead of molar flows in this analysis. Specifying that no water or DME is present in the feed, the mole fractions of all components are given by

$$\begin{aligned} x_{MeOH} &= x_{MeOH}^0 - \xi_2 - 2\xi_1 \\ x_{DME} &= \xi_1 \\ x_{H_2O} &= \xi_1 + \xi_2 \end{aligned}$$

where ξ_1 and ξ_2 are the extents of reactions 1 and 2 on a mole fraction basis and x_{MeOH}^0 is the mole fraction of methanol in the feed. Substituting these into the equilibrium expression gives

$$K_1 = \frac{\xi_1 \cdot (\xi_1 + \xi_2)}{(x_{MeOH}^0 - \xi_2 - 2\xi_1)^2}$$

Solving for ξ_1 as a function of ξ_2 gives

$$\xi_1 = \frac{1}{2 \cdot (4K_1 - 1)} \cdot \left[4K_1 \cdot x_{MeOH}^0 - (4K_1 - 1) \cdot \xi_2 - \sqrt{4K_1 \cdot (x_{MeOH}^0)^2 - (4K_1 - 1) \cdot \xi_2^2} \right].$$

This can be written in terms of sulfur product yield (Y_{SP}), methanol conversion (X_{MeOH}), and DME yield (Y_{DME}) by substituting

$$Y_{SP} = \frac{\xi_2}{x_{MeOH}^0}$$

$$Y_{DME} = \frac{2\xi_1}{x_{MeOH}^0}$$

$$X_{MeOH} = Y_{SP} + Y_{DME}$$

for ξ_1 and ξ_2 , giving

$$Y_{DME} = \frac{1}{(4K_1 - 1)} \cdot \left[4K_1 - (4K_1 - 1) \cdot Y_{SP} - \sqrt{4K_1 - (4K_1 - 1) \cdot Y_{SP}^2} \right].$$

A similar calculation can be performed in which the yield to sulfur products is fixed and the H₂S, MT, and DMS are brought to equilibrium. This calculation will give the yields to MT and DMS if the disproportionation reaction is faster than the reactions that increase the yield to sulfur products. The equilibrium mole fractions for the disproportionation reaction are given by the expression

$$K_3 = \frac{x_{DMS} \cdot x_{H_2S}}{x_{MT}^2}$$

where K_3 is the equilibrium constant for the disproportionation reaction. The two reactions involved in this calculation are



Specifying that no MT or DMS is present in the feed, the mole fractions of all components are given by

$$x_{H_2S} = x_{H_2S}^0 - \xi_4 + \xi_3$$

$$x_{DMS} = \xi_3$$

$$x_{MT} = \xi_4 - 2\xi_3$$

where ξ_3 and ξ_4 are the extents of reactions 3 and 4 on a mole fraction basis and $x_{H_2S}^0$ is the mole fraction of H_2S in the feed. Substituting these into the equilibrium expression gives

$$K_3 = \frac{\xi_3 \cdot (x_{H_2S}^0 + \xi_3 - \xi_4)}{(\xi_4 - 2\xi_3)^2}.$$

Solving for ξ_3 as a function of ξ_4 gives

$$\xi_3 = \frac{1}{2 \cdot (4K_3 - 1)} \cdot \left[x_{H_2S}^0 + (4K_3 - 1) \cdot \xi_4 - \sqrt{x_{H_2S}^0 + (4K_3 - 1) \cdot \xi_4 \cdot (2x_{H_2S}^0 - \xi_4)} \right].$$

This can be written in terms of sulfur product yield (Y_{SP}), MT yield (Y_{MT}), DMS yield (Y_{DMS}), and feed ratio (FR) by substituting

$$Y_{SP} = \frac{\xi_4}{x_{MeOH}^0}$$

$$Y_{DMS} = \frac{2\xi_3}{x_{MeOH}^0}$$

$$Y_{MT} = Y_{SP} - Y_{DMS}$$

$$FR = \frac{x_{MeOH}^0}{x_{H_2S}^0}$$

for ξ_3 , ξ_4 , and $x_{H_2S}^0$. This gives

$$Y_{DMS} = \frac{1}{(4K_3 - 1)} \cdot \left[\frac{1}{FR} - (4K_3 - 1) \cdot Y_{SP} - \sqrt{\frac{1}{FR^2} + (4K_3 - 1) \cdot Y_{SP} \cdot \left(\frac{2}{FR} - Y_{SP} \right)} \right].$$

3.1.2 Experimental Reaction Data

The catalysts studied fall into three groups based on their reactivity. The first group, consisting of $\text{La}_2\text{O}_3/\text{Al}_2\text{O}_3$, $\gamma\text{-Al}_2\text{O}_3$, HZSM-5 and WO_3/ZrO_2 , showed significantly higher activity to sulfur products than the other catalysts. Although the catalysts in this group were not extensively investigated under identical conditions of temperature, feed ratio and yield of sulfur products, it can be concluded that the general order of specific reactivity is $\text{WO}_3/\text{ZrO}_2 > \text{La}_2\text{O}_3/\text{Al}_2\text{O}_3 > \gamma\text{-Al}_2\text{O}_3 > \text{HZSM-5}$.

$\text{La}_2\text{O}_3/\text{Al}_2\text{O}_3$ gave a high yield to sulfur products even at high space velocities. Tables 3.2 and 3.3 give the results for different conditions of temperature, feed ratio and space velocity. At a temperature of 400°C , methanol feed rates of $38\text{-}135 \mu\text{mol}/\text{m}^2\text{-h}$ (WHSV $0.39\text{-}1.40 \text{ h}^{-1}$), and a feed ratio (moles MeOH/moles H_2S) of $1.9\text{-}2.1$, 92-97% of the methanol is converted to sulfur products with a selectivity to DMS between 89 and 96%. Looking at Table 3.2, it can be seen that the selectivity to DMS increases with temperature, increases with feed ratio over a range of $1.4\text{-}2.1$, and decreases slightly with space velocity from $38\text{-}135 \mu\text{mol}/\text{m}^2\text{-h}$.

The affinity A given in the Tables is that of reaction 3, MT disproportionation, at the reactor exit. At 400°C and an H_2S conversion less than 99%, this affinity is close to zero, indicating that this reaction is close to equilibrium. The affinity for MT disproportionation decreases with temperature from $340\text{-}400^\circ\text{C}$. The average yield to DMS (when fit by linear regression) increases from 55-89% as the sulfur product yield increases from 72-97%. The average MT yield decreases from 17 to 8% over this range.

Figures 3.1 and 3.2 show how the product distribution varies with increasing conversion of methanol to sulfur products. The solid lines represent the equilibrium values (at 370°C) of methanol conversion, DME yield, DMS yield, and MT yield as calculated using the equations of

Table 3.2. Performance of $\text{La}_2\text{O}_3/\text{Al}_2\text{O}_3$ with increasing temperature from 340-400°C. Space velocity is 38-40 $\mu\text{mol}/\text{m}^2\text{-h}$ (WHSV 0.40-0.42 h^{-1}) except at 360°C where it is 29 $\mu\text{mol}/\text{m}^2\text{-h}$ (WHSV 3.1 h^{-1}). Three runs per data point.

Temp. (°C)	Feed Ratio	X, MeOH	X, H ₂ S	Y, SP	S, MT	A
340	1.99 ± 0.33	92 ± 1	91 ± 3	72 ± 10	27 ± 1	2.4 ± 0.3
360	1.46 ± 0.62	94 ± 1	79 ± 22	86 ± 5	26 ± 18	1.3 ± 0.2
380	2.13 ± 0.24	95 ± 1	96 ± 1	84 ± 6	7 ± 4	0.4 ± 0.9
400	2.00 ± 0.11	96 ± 2	93 ± 1	90 ± 4	4 ± 2	-1.4 ± 1.0

Table 3.3. Performance of $\text{La}_2\text{O}_3/\text{Al}_2\text{O}_3$ at 400°C with increasing feed ratio. To convert to WHSV, divide space velocities by 96. Three runs per data point.

Feed Ratio	$\mu\text{mol}/\text{m}^2\text{-h}$	X, MeOH	X, H ₂ S	Y, SP	S, MT	A
1.42 ± 0.66	31 ± 14	98 ± 2	78 ± 27	97 ± 3	14 ± 20	-0.1 ± 0.7
1.73 ± 0.13	68 ± 5	94 ± 3	82 ± 4	91 ± 5	4 ± 2	-2.5 ± 1.0
1.74 ± 0.04	138 ± 3	98 ± 1	99 ± 1	97 ± 1	17 ± 1	3.6 ± 1.1
1.88 ± 0.09	134 ± 6	96 ± 1	99 ± 1	95 ± 1	11 ± 2	2.3 ± 0.1
1.89 ± 0.06	84 ± 3	97 ± 1	99 ± 2	96 ± 1	8 ± 2	1.7 *
1.91 ± 0.06	135 ± 4	96 ± 1	99 ± 1	95 ± 2	10 ± 1	3.0 ± 0.3
1.93 ± 0.08	77 ± 3	97 ± 1	99 ± 1	94 ± 2	9 ± 3	2.5 *
2.00 ± 0.11	38 ± 2	96 ± 2	93 ± 1	90 ± 4	4 ± 2	-1.4 ± 1.0
2.02 ± 0.08	79 ± 3	93 ± 1	97 ± 2	91 ± 2	6 ± 3	0.3 ± 1.6
2.06 ± 0.29	359 ± 50	93 ± 1	102 ± 4	79 ± 6	26 ± 4	
2.12 ± 0.11	82 ± 4	93 ± 1	96 ± 1	87 ± 3	5 ± 2	-0.2 ± 0.9

* Could not compute standard deviation; some indeterminate (infinite) values of A.

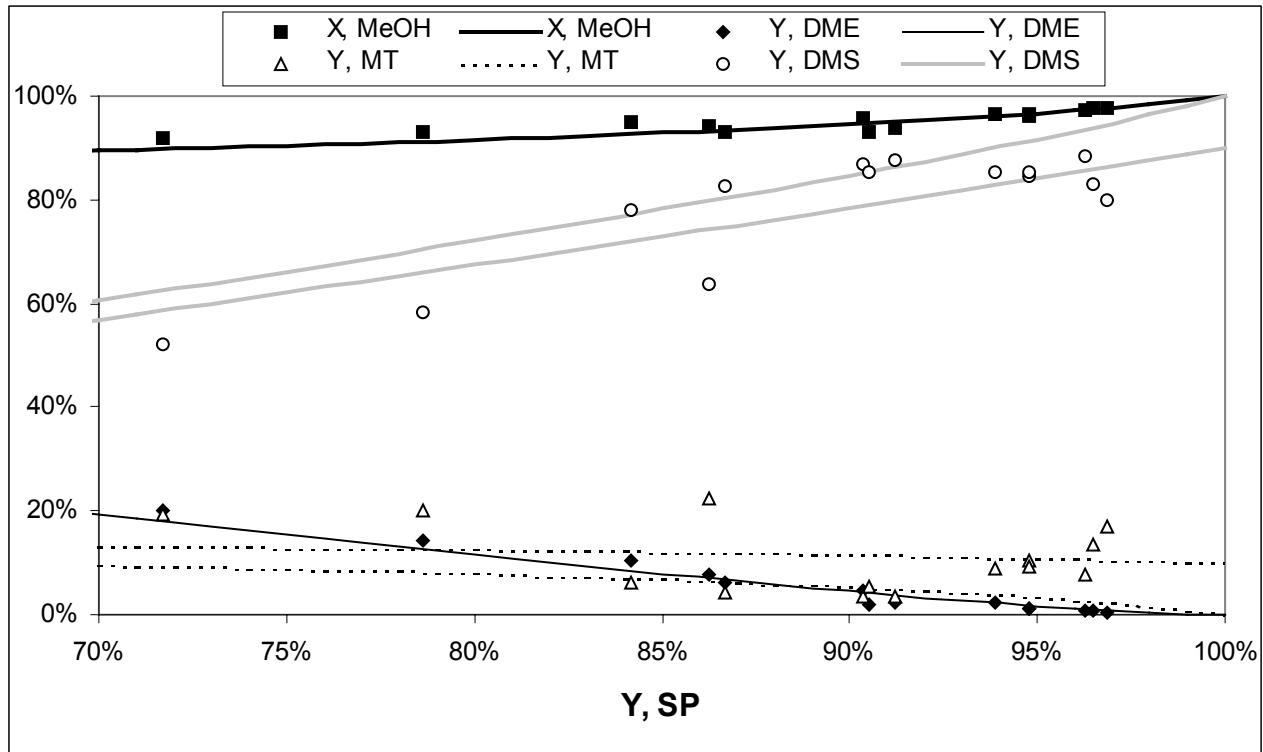


Figure 3.1. Yields and conversion on $\text{La}_2\text{O}_3/\text{Al}_2\text{O}_3$ versus yield to sulfur products at 340-400°C.

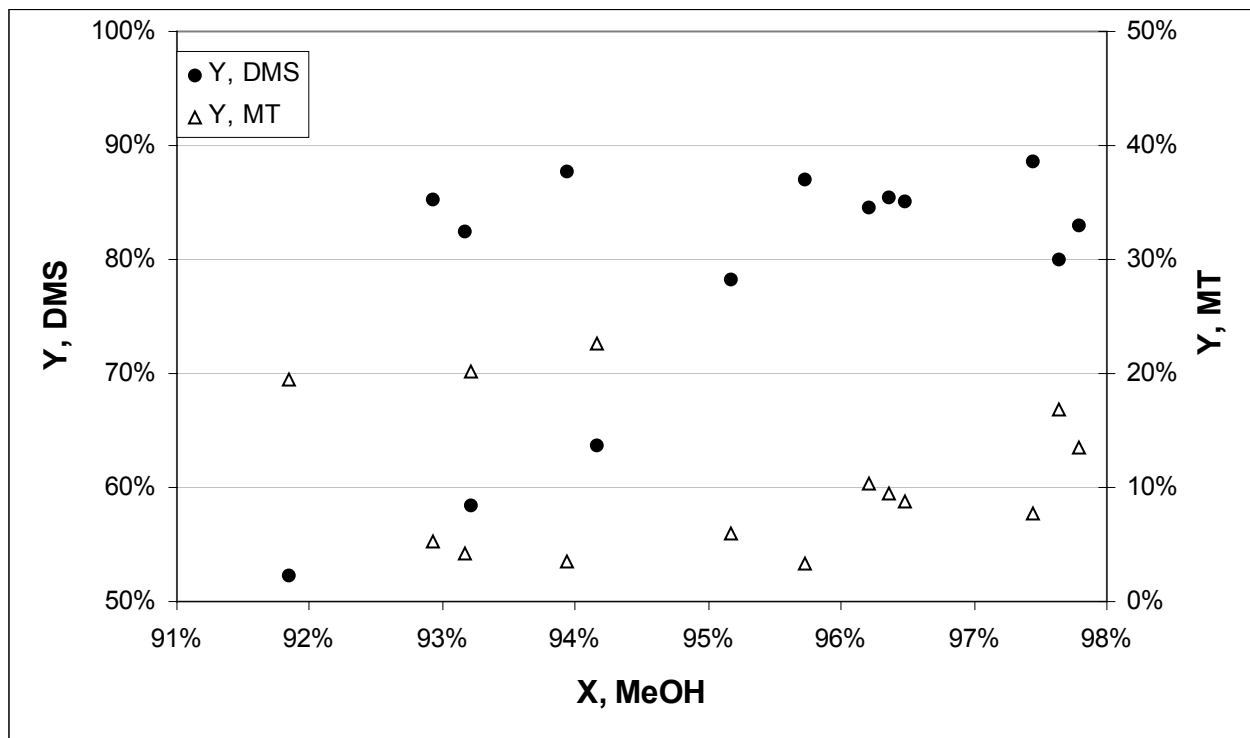


Figure 3.2. Yield to DMS and MT with varying methanol conversion on $\text{La}_2\text{O}_3/\text{Al}_2\text{O}_3$.

section 3.1.1. For the sulfur product yields observed, the equilibrium lines do not vary significantly with temperature from 340-400°C so an average temperature of 370°C can be applied. The lines representing the equilibrium values of DMS and MT yields established by the disproportionation reaction do vary significantly with feed ratio; lines are drawn at feed ratios of 1.6 (the lower line for DMS and the upper line for MT) and 2.0. The equilibrium value for DMS yield at a given sulfur product yield increases with feed ratio and the value for MT yield decreases with feed ratio.

As shown in Figure 3.1, the conversion of methanol to DME peaks at residence times shorter than were investigated. Over the range of data collected, as the yield to sulfur products increases from 72-97%, the conversion of methanol increases only from 92-98%. The yield to DME decreases from 20-1% over the same range. The affinity for this reaction is close to zero, indicating that the reaction is close to equilibrium. From these observations it can be concluded that at longer residence times DME either directly reacts to form sulfur products, or first converts back to methanol, which subsequently reacts to form sulfur products. Figure 3.2 shows that the yields of both DMS and MT fluctuate as methanol conversion increases from 92-98%, and no conclusion as to their trend with respect to conversion is possible.

At 340°C, WO_3/ZrO_2 converts greater than 84% of the methanol to sulfur products at space velocities between 107 and 272 $\mu\text{mol}/\text{m}^2\text{-h}$ (WHSV 0.27-0.68 h^{-1}) and feed ratios of 1.3-2.2. Catalyst performance at varying conditions is shown in Tables 3.4 and 3.5. The affinity (A) in the Tables again refers to reaction (3) at exit conditions. At 340°C, a space velocity of 262 $\mu\text{mol}/\text{m}^2\text{-hr}$ and a feed ratio of 2.0-2.1, WO_3/ZrO_2 converts 85% of the methanol to sulfur products. On $\text{La}_2\text{O}_3/\text{Al}_2\text{O}_3$ at the same temperature and a similar feed ratio, only 72% of the methanol is converted to sulfur products at a space velocity of 40 $\mu\text{mol}/\text{m}^2\text{-hr}$, so at this

Table 3.4. Performance of WO_3/ZrO_2 at 360°C with increasing feed ratio. To convert to WHSV, divide space velocities by 401. Three runs per data point.

Feed Ratio	$\mu\text{mol}/\text{m}^2\text{-hr}$	X, MeOH	X, H_2S	Y, SP	S, MT	A
1.97 ± 0.17	106 ± 9	99 ± 1	97 ± 3	95 ± 3	4 ± 3	-0.4 ± 1.2
2.00 ± 0.09	256 ± 12	100 ± 1	97 ± 5	89 ± 3	9 ± 1	1.3 *
2.06 ± 0.14	101 ± 7	98 ± 1	94 ± 3	90 ± 3	1 ± 1	-3.4 ± 0.4

* standard deviation could not be calculated due to infinite value for one or more samples

Table 3.5. Performance of WO_3/ZrO_2 at 340°C with increasing feed ratio. To convert to WHSV, divide space velocities by 401. Three runs per data point.

Feed Ratio	$\mu\text{mol}/\text{m}^2\text{-hr}$	X, MeOH	X, H_2S	Y, SP	S, MT	A
1.30 ± 0.08	253 ± 16	100 ± 1	77 ± 2	94 ± 4	26 ± 1	1.2 ± 0.1
1.35 ± 0.62	143 ± 66	100 ± 1	80 ± 35	98 ± 3	21 ± 6	1.0 *
1.35 ± 0.10	272 ± 20	100 ± 1	82 ± 4	96 ± 1	27 ± 1	1.5 ± 0.2
1.52 ± 0.31	461 ± 94	94 ± 6	74 ± 15	77 ± 19	27 ± 5	1.1 ± 0.6
1.62 ± 0.22	262 ± 36	100 ± 1	90 ± 9	91 ± 2	21 ± 2	1.7 ± 0.8
1.66 ± 0.41	116 ± 29	100 ± 1	93 ± 23	99 ± 2	14 ± 6	1.3 *
1.94 ± 0.07	149 ± 5	100 ± 1	96 ± 2	91 ± 1	9 ± 1	1.1 ± 0.5
1.99 ± 0.17	107 ± 9	99 ± 1	97 ± 2	91 ± 5	7 ± 2	0.8 ± 0.4
2.05 ± 0.12	262 ± 15	100 ± 1	99 ± 5	85 ± 1	14 ± 1	3.7 *
2.18 ± 0.17	159 ± 12	99 ± 1	98 ± 1	84 ± 5	7 ± 1	1.0 ± 0.3
2.20 ± 0.28	108 ± 14	98 ± 1	96 ± 3	84 ± 8	3 ± 1	-1.1 ± 0.9
2.39 ± 0.16	167 ± 11	98 ± 1	98 ± 4	79 ± 3	5 ± 1	0.5 *

temperature WO_3/ZrO_2 is more active. At 360°C , WO_3/ZrO_2 converted 1.6-2.0% of the methanol to hydrocarbons (mostly methane), so temperatures above this were not examined. As with $\text{La}_2\text{O}_3/\text{Al}_2\text{O}_3$, the selectivity to DMS increases when the temperature increases from 340 to 360°C . This selectivity decreases with space velocity (107 - $262 \mu\text{mol}/\text{m}^2\text{-h}$) and increases with feed ratio from 1.3 to 2.4 .

As can be seen in Figures 3.3 and 3.4, the yields to sulfur products and DME behave in the same way at longer residence times as for $\text{La}_2\text{O}_3/\text{Al}_2\text{O}_3$. There is still no correlation between MeOH conversion and the sulfur product selectivities at these high conversions, although the DMS and MT yields generally increase with MeOH conversion at constant feed rate. As the yield to sulfur products increases from 77 - 99% , the average DMS yield increases from 70 - 83% and the MT yield increases from 7 - 15% . When 77% of the methanol has been converted to sulfur products, the yield of DME and conversion of methanol are 17 and 94% , respectively. The DME yield decreases linearly with sulfur product yield. When 99% of the methanol has been converted to sulfur products, the DME yield is 1% . At sulfur product yields greater than 80% , the affinity of this reaction is less than -2 , indicating that the rate of this reaction relative to the rates of reactions forming C-S bonds is lower for this catalyst than for the other catalysts that show high activity for DMS production. At 340°C , the affinity of MT disproportionation is positive but close to zero for most conditions. This affinity decreases when the temperature rises to 360°C .

The trends in the results for a $\gamma\text{-Al}_2\text{O}_3$ catalyst are similar to those of the previous two catalysts, but the activity is lower. At a temperature of 400°C , and a feed ratio of 2.0 - 2.1 , 86% conversion of methanol to sulfur products is achieved at a space velocity of $32 \mu\text{mol}/\text{m}^2\text{-hr}$. At the same temperature and a similar feed ratio on $\text{La}_2\text{O}_3/\text{Al}_2\text{O}_3$, the conversion is 91% at a space

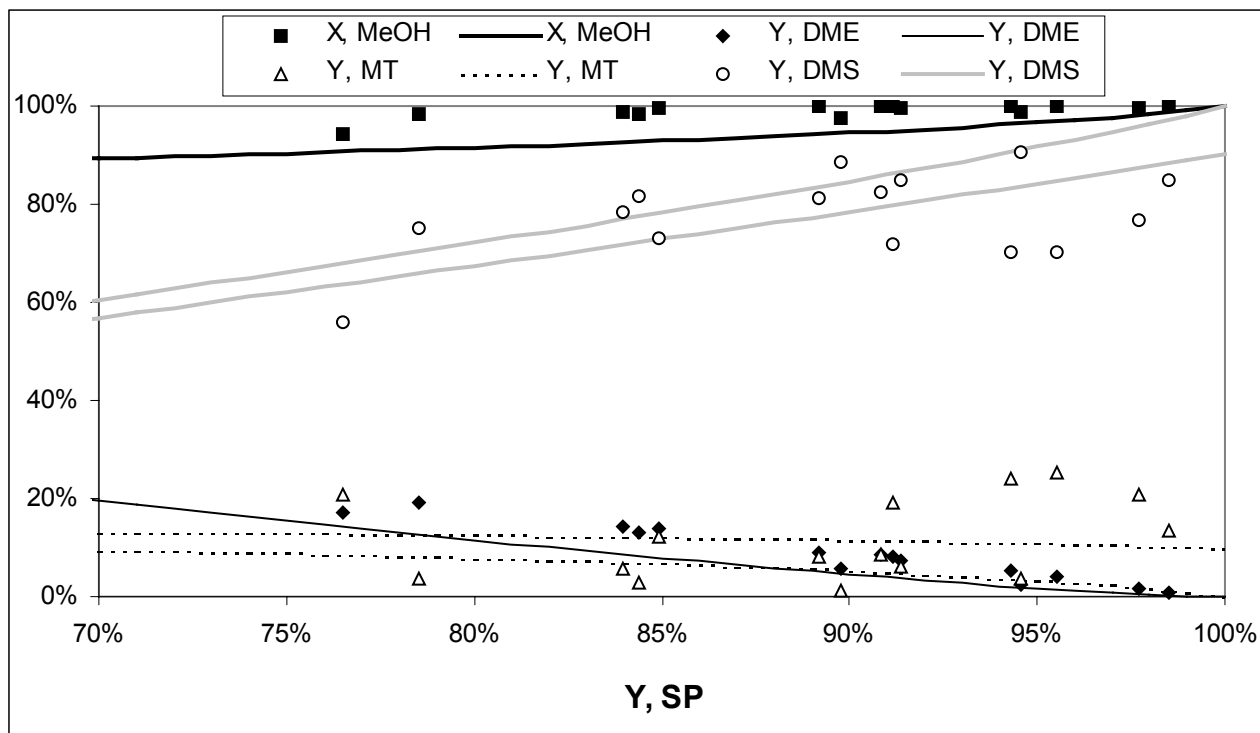


Figure 3.3. Yields and conversion on WO_3/ZrO_2 versus yield to sulfur products at 340°C . The equilibrium lines have the same meaning as in Figure 3.1 but are drawn at 340°C .

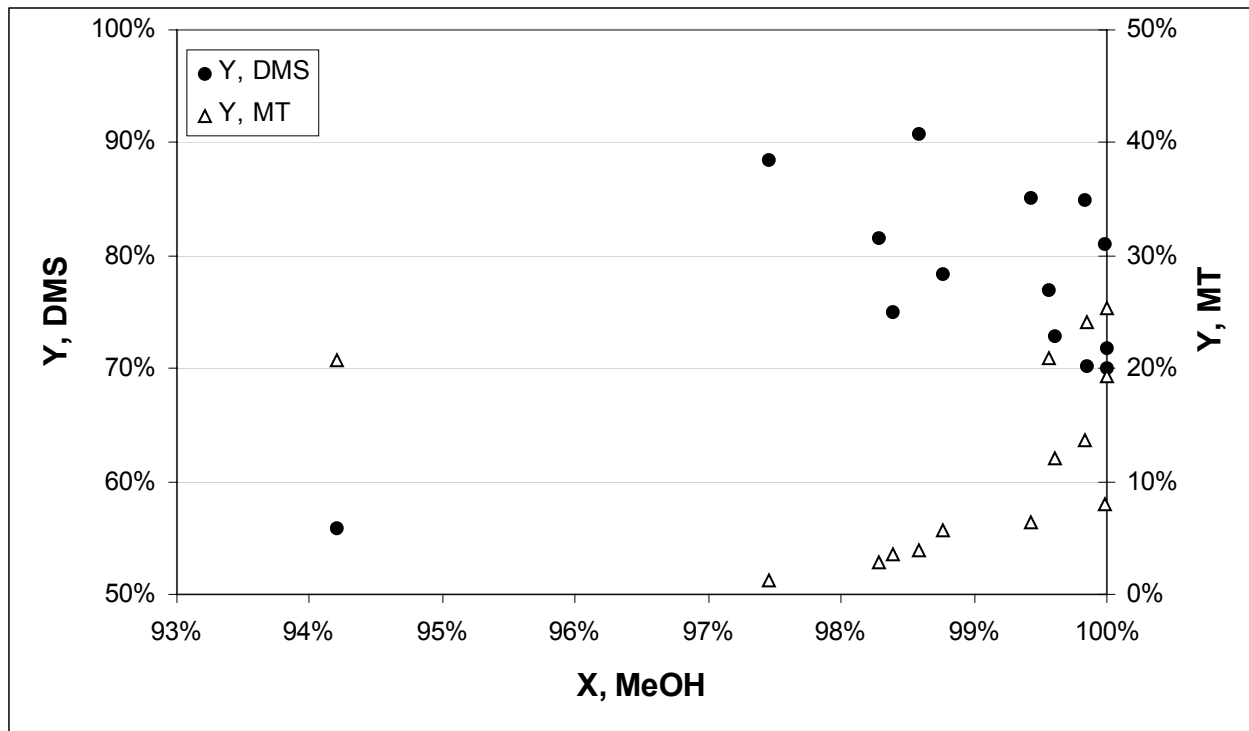


Figure 3.4. Yield to DMS and MT versus methanol conversion on WO_3/ZrO_2 .

velocity of 79 $\mu\text{mol}/\text{m}^2\text{-hr}$. The results for this catalyst are given in Tables 3.6 and 3.7. The affinity (A) in the Tables again refers to reaction (3) at exit conditions. At 340°C and a feed ratio of 2.3-2.4, this catalyst converted 57% of the methanol to sulfur products at a space velocity of 89 $\mu\text{mol}/\text{m}^2\text{-hr}$ compared to 79% at 167 $\mu\text{mol}/\text{m}^2\text{-hr}$ for WO_3/ZrO_2 at the same temperature and a similar feed ratio. Like the other two catalysts, the selectivity to DMS increases with temperature, decreases with space velocity, and increases slightly with feed ratio.

Table 3.6. Performance of $\gamma\text{-Al}_2\text{O}_3$ with increasing temperature from 340-400°C. Space velocity is 32-36 $\mu\text{mol}/\text{m}^2\text{-h}$ (WHSV 0.18-0.20 h^{-1}). Three runs per data point.

Temp. (°C)	Feed Ratio	X, MeOH	X, H ₂ S	Y, SP	S, MT	A
340	2.34 ± 0.24	89 ± 1	74 ± 3	57 ± 3	11 ± 1	-0.8 ± 0.1
360	2.15 ± 0.10	91 ± 1	82 ± 1	72 ± 3	6 ± 1	-1.6 ± 0.2
380	2.10 ± 0.03	93 ± 1	88 ± 1	82 ± 1	3 ± 1	-2.8 ± 0.1
400	2.07 ± 0.06	94 ± 1	90 ± 1	86 ± 2	1 ± 1	-4.4 ± 0.5

Table 3.7. Performance of $\gamma\text{-Al}_2\text{O}_3$ at 400°C with increasing feed ratio. Divide space velocity by 184 to give WHSV. Three runs per data point.

Feed Ratio	$\mu\text{mol}/\text{m}^2\text{-hr}$	X, MeOH	X, H ₂ S	Y, SP	S, MT	A
1.52 ± 0.44	57 ± 17	96 ± 1	81 ± 15	94 ± 2	13 ± 12	-0.2 ± 0.8
1.75 ± 0.10	65 ± 4	97 ± 1	90 ± 1	94 ± 3	9 ± 3	-0.1 ± 0.7
1.87 ± 0.10	34 ± 2	96 ± 2	89 ± 2	92 ± 5	3 ± 1	-2.7 ± 1.2
1.87 ± 0.02	46 ± 1	95 ± 2	89 ± 1	92 ± 1	4 ± 1	-2.0 ± 0.6
2.07 ± 0.06	32 ± 1	94 ± 1	90 ± 1	86 ± 2	1 ± 1	-4.4 ± 0.5
2.39 ± 0.17	40 ± 3	92 ± 1	94 ± 2	78 ± 3	1 ± 1	-4.3 ± 0.6

Trends in methanol conversions and DME yields vs. sulfur product yields for $\gamma\text{-Al}_2\text{O}_3$ are also similar to those of the previous two catalysts, as seen in Figures 3.5-3.6. When 57% of the methanol has been converted to sulfur products, the DME yield is 32% and the methanol conversion is 89%. As the yield to sulfur products increases to 94%, the yield of DME decreases linearly to 2% and the conversion of methanol increases to 96%. Under all conditions investigated, the affinity is negative for the reaction to DME, although it is close to equilibrium ($-1 < A < 0$). For all conditions investigated, affinity is negative for the reaction to DME, although it is close to equilibrium ($-1 < A < 0$). For all conditions investigated, the affinity for MT disproportionation is negative, indicating that this reaction produces MT from DMS near the reactor exit. Figure 3.6 shows that DMS yield increases while the MT yield remains relatively constant as methanol conversion increases from 89-97%. As the sulfur product yield increases from 57-94%, the average DMS yield increases from 54-89%, but the MT yield only increases from 3-5%.

HZSM-5 was the least active of the four catalysts in the first group. Compared to $\gamma\text{-Al}_2\text{O}_3$ at 400°C and a feed ratio of 1.7-1.8, 77% of the methanol is converted to sulfur products over HZSM-5 at a WHSV of 0.37 h⁻¹, compared to 94% for $\gamma\text{-Al}_2\text{O}_3$ at the same conditions. However, HZSM-5 was the least selective catalyst to MT, with this selectivity being less than 5% at 400°C for most conditions. Looking at the results in Tables 3.8 and 3.9, it is seen that just as for the other catalysts in this group, this selectivity to DMS increases with temperature and decreases with space velocity. Unlike most of the other catalysts examined, the selectivity to DMS decreases slightly with increasing feed ratio.

As the yield to sulfur products increases from 51 to 77%, the DME yield decreases from 21 to 14% and the methanol conversion increases from 72 to 91% (Figure 3.7). It appears that at

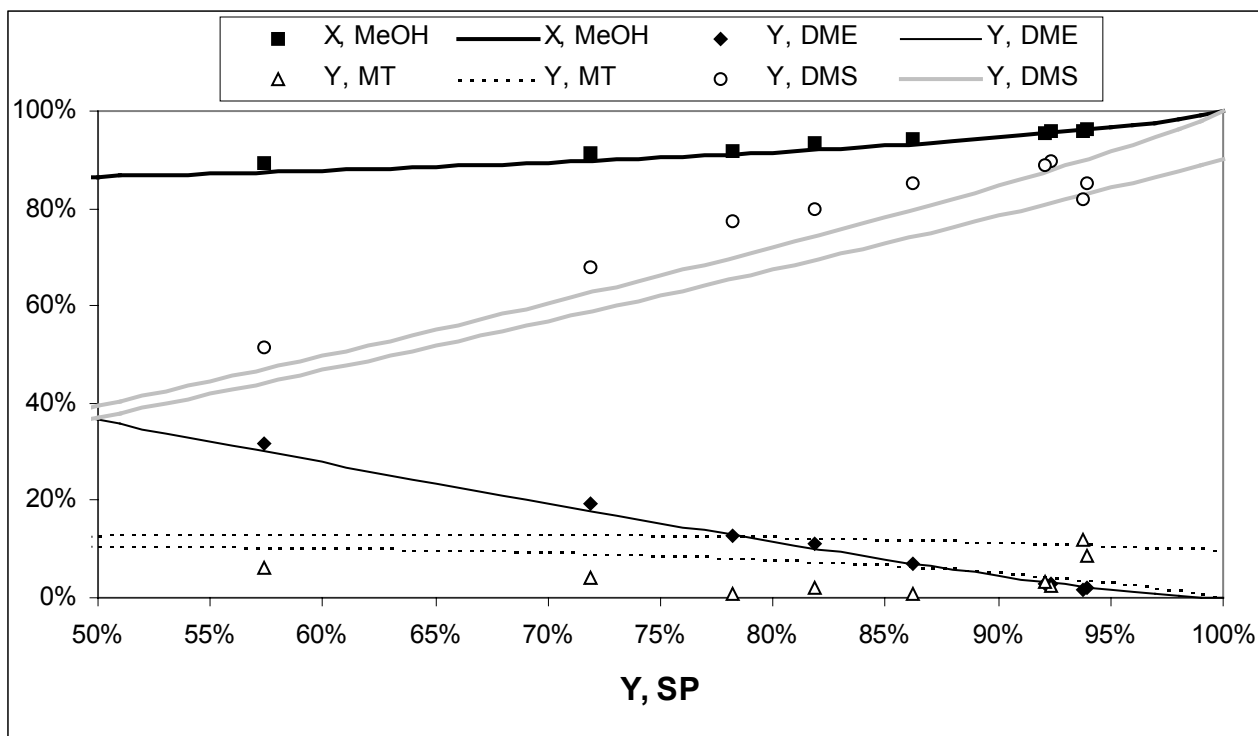


Figure 3.5. Yields and conversion on $\gamma\text{-Al}_2\text{O}_3$ versus yield to sulfur products at 340-400°C. The equilibrium lines have the same meaning as in Figure 3.1.

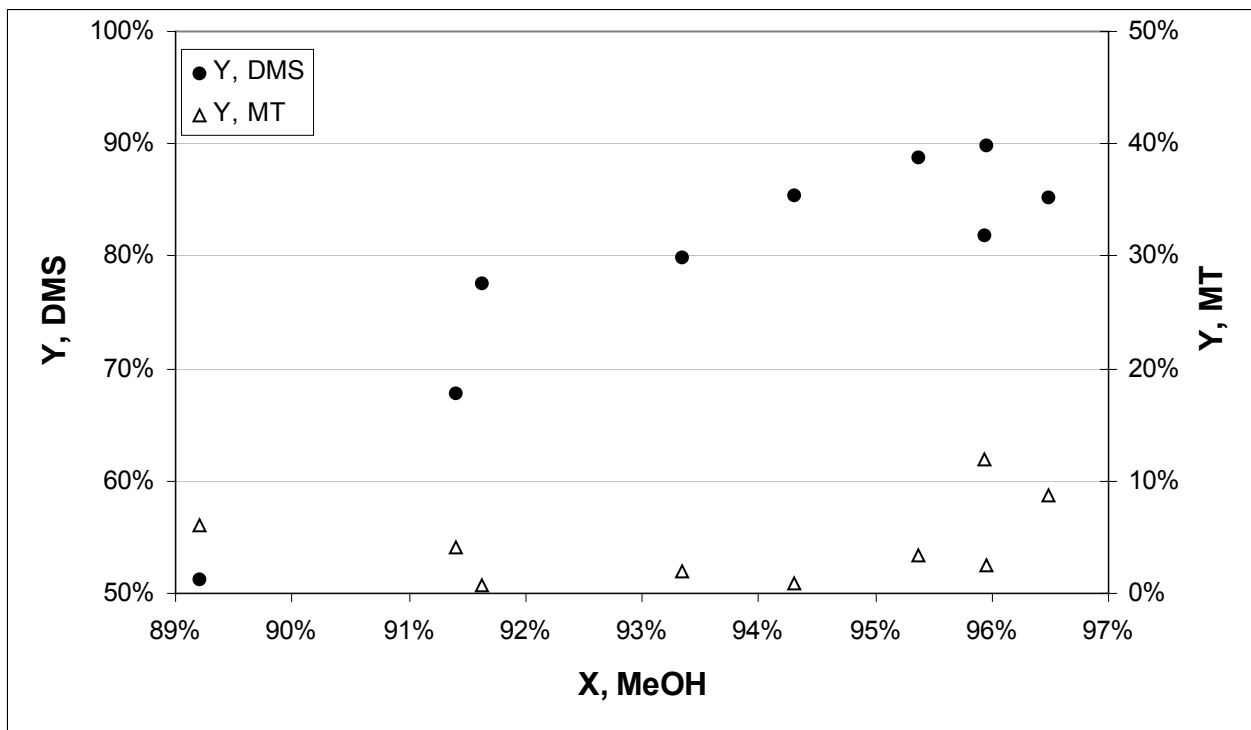


Figure 3.6. Yield to DMS and MT versus methanol conversion on $\gamma\text{-Al}_2\text{O}_3$.

Table 3.8. Performance of HZSM-5 with increasing temperature from 340-400°C. Space velocity for first four entries is 27-30 $\mu\text{mol}/\text{m}^2\text{-h}$ (WHSV 0.38-0.42 h^{-1}) and 51-54 $\mu\text{mol}/\text{m}^2\text{-h}$ (WHSV 0.73-0.76 h^{-1}) for last three. Three runs per data point.

Temp. (°C)	Feed Ratio	X, MeOH	X, H ₂ S	Y, SP	S, MT	A
340	1.92 ± 0.10	72 ± 3	55 ± 3	51 ± 5	12 ± 3	-1.4 ± 0.5
360	1.73 ± 0.03	80 ± 1	58 ± 1	62 ± 2	8 ± 1	-2.2 ± 0.2
380	1.77 ± 0.09	85 ± 2	64 ± 1	69 ± 4	5 ± 1	-2.8 ± 0.2
400	1.82 ± 0.19	89 ± 2	70 ± 2	74 ± 6	4 ± 1	-3.1 ± 0.3
360	2.04 ± 0.04	78 ± 1	64 ± 3	56 ± 1	12 ± 4	-1.0 ± 0.8
380	1.95 ± 0.05	84 ± 1	67 ± 1	63 ± 1	9 ± 1	-1.5 ± 0.1
400	1.95 ± 0.03	88 ± 1	71 ± 1	69 ± 1	7 ± 1	-2.0 ± 0.5

Table 3.9. Performance of HZSM-5 at 400°C with increasing feed ratio. To convert space velocity to WHSV, divide by 71. Three runs per data point.

Feed Ratio	$\mu\text{mol}/\text{m}^2\text{-hr}$	X, MeOH	X, H ₂ S	Y, SP	S, MT	A
1.72 ± 0.11	26 ± 2	91 ± 2	69 ± 1	77 ± 4	4 ± 1	-3.2 ± 0.2
1.82 ± 0.19	28 ± 3	89 ± 2	70 ± 2	74 ± 6	4 ± 1	-3.1 ± 0.3
1.86 ± 0.15	26 ± 2	91 ± 2	73 ± 1	76 ± 5	4 ± 1	-3.1 ± 0.3
1.95 ± 0.03	51 ± 1	88 ± 1	71 ± 1	69 ± 1	7 ± 1	-2.0 ± 0.5
2.03 ± 0.06	35 ± 1	90 ± 1	74 ± 1	70 ± 3	4 ± 1	-2.8 ± 0.3

lower sulfur product yield (50-65%) the yield of DME is constant and the affinity for its production is positive. At higher yields, the yield to DME decreases and closely follows the equilibrium value with an affinity close to zero. Like the $\gamma\text{-Al}_2\text{O}_3$ catalyst, the affinity for MT

disproportionation is negative (Tables 3.8 and 3.9), so MT is produced from DMS near the reactor exit. But Figure 3.8 shows clearly that the yield to DMS increases and the yield to MT decreases or remains constant as methanol conversion increases from 70-90%. As the sulfur product yield increases from 51-74%, the average DMS yield increases from 44-71%, and the average MT yield decreases from 7 to 3%.

The second group of catalysts consists of $\text{WO}_3/\text{Al}_2\text{O}_3$, $\text{MoO}_3/\text{SiO}_2$, SAPO-18 and AlPO-18. These are less active than those of the first group for the sulfidation of methanol, but are more selective to MT.

$\text{WO}_3/\text{Al}_2\text{O}_3$ is the most selective catalyst to MT that was examined; reaction results are shown in Figures 3.9 and 3.10. Over a wide range of conditions, with feed ratios between 0.3 and 0.7, the selectivity of MT is greater than 80%. Temperatures from 340-400°C and space velocities from 14-59 $\mu\text{mol}/\text{m}^2\text{-h}$ (WHSV 0.07-0.30) were investigated. Under all conditions, increasing the temperature and feed ratio as well as decreasing the space velocity decreased the MT selectivity; this is also evident from the large positive affinity values for MT disproportionation given in Table 3.10. The highest selectivity to MT of 93% was obtained at 340°C, a feed ratio of 0.33 and a space velocity of 74 $\mu\text{mol}/\text{m}^2\text{-hr}$. At 400°C, a feed ratio of 0.31 and a space velocity of 26 $\mu\text{mol}/\text{m}^2\text{-h}$, 94% of the methanol is converted to sulfur products with 91% of this amount being MT.

At sulfur product yields less than 90%, the affinity for DME production is positive; at higher sulfur product yields the DME and methanol are close to equilibrium. As the sulfur product yield increases from 40 to 96%, the DME yield decreases from 17 to 1% and the methanol conversion increases from 55 to 99%. Figure 3.10 shows that both DMS and MT yields increase with methanol conversion increasing from 50-100%. As the sulfur product yield

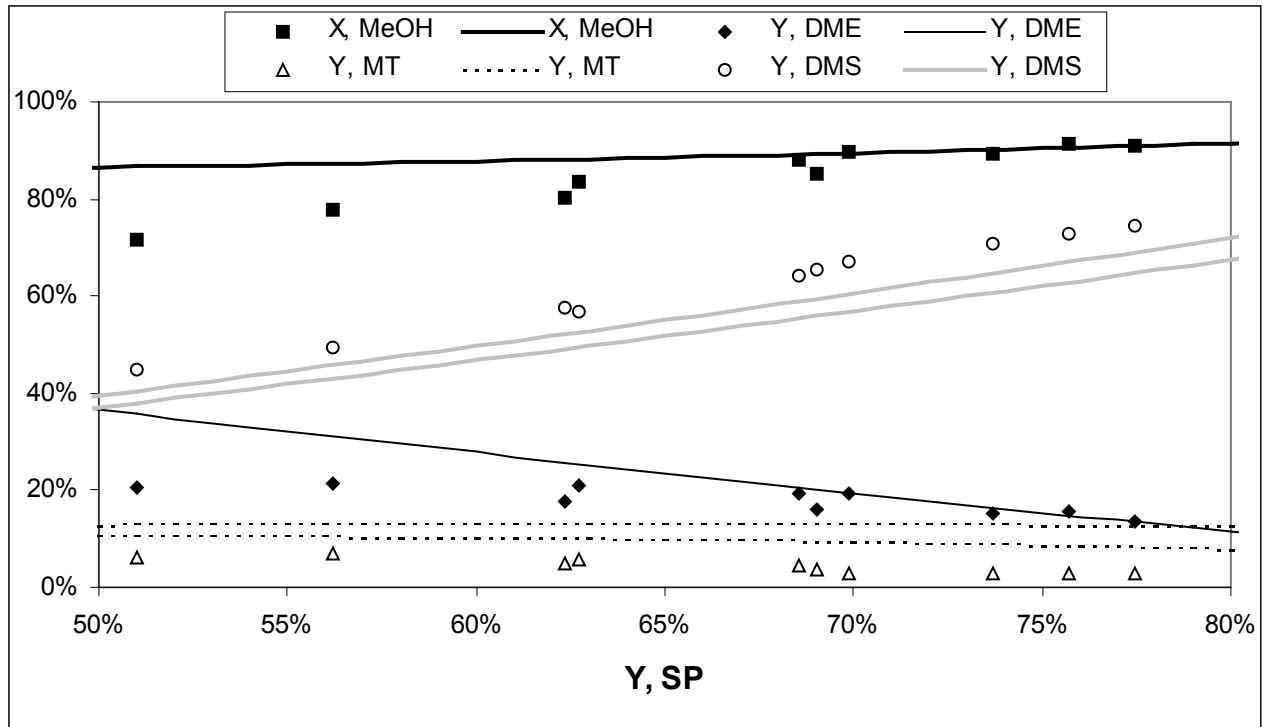


Figure 3.7. Yields and conversion on HZSM-5 versus yield to sulfur products at 340-400°C. The equilibrium lines have the same meaning as in Figure 3.1.

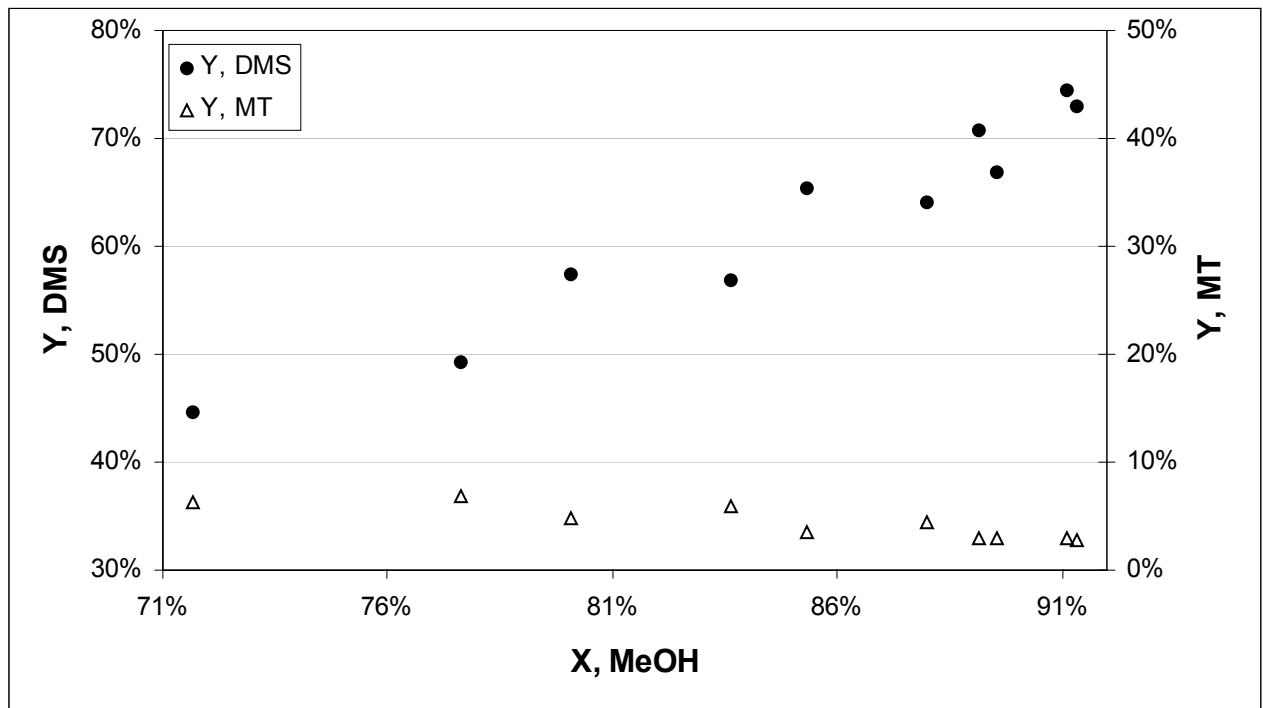


Figure 3.8. Yield to DMS and MT versus methanol conversion on HZSM-5.

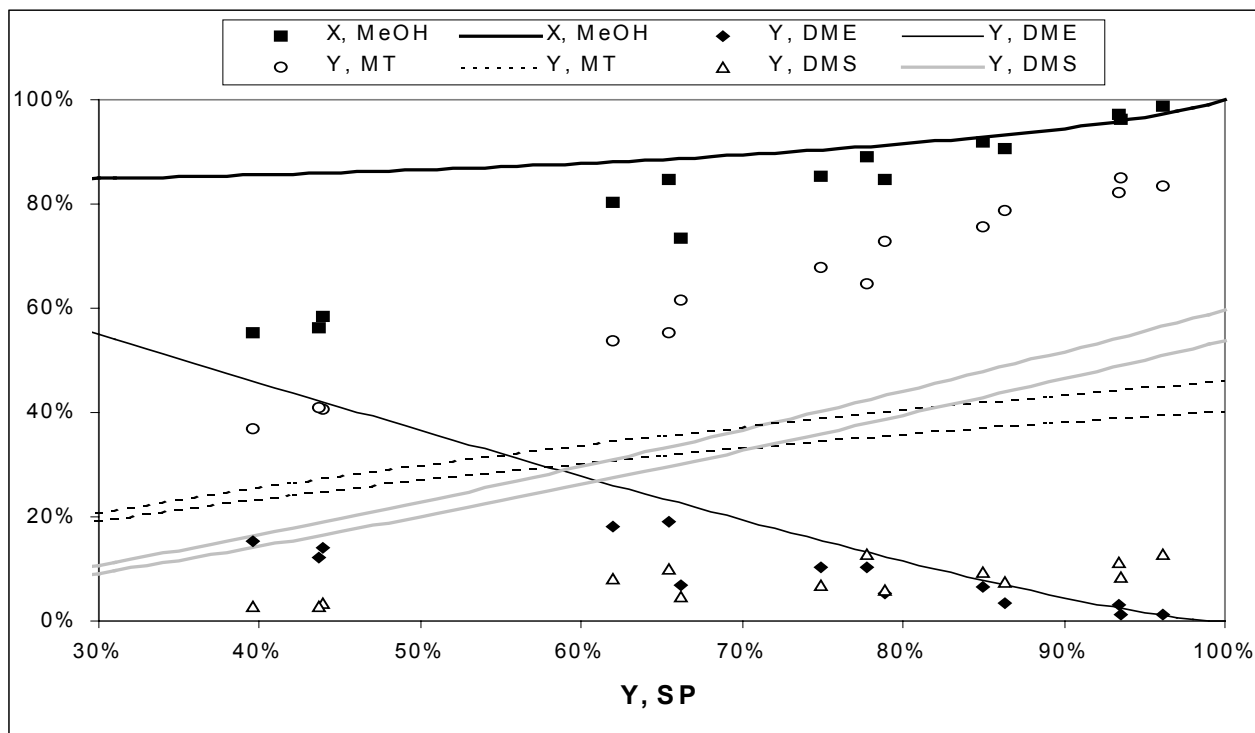


Figure 3.9. Yields and conversion on $\text{WO}_3/\text{Al}_2\text{O}_3$ versus yield to sulfur products at 340-400°C. Equilibrium lines have same meaning as in Figure 3.1 but are drawn at feed ratios of 0.3 (lower curve, DMS and upper curve, MT) and 0.4.

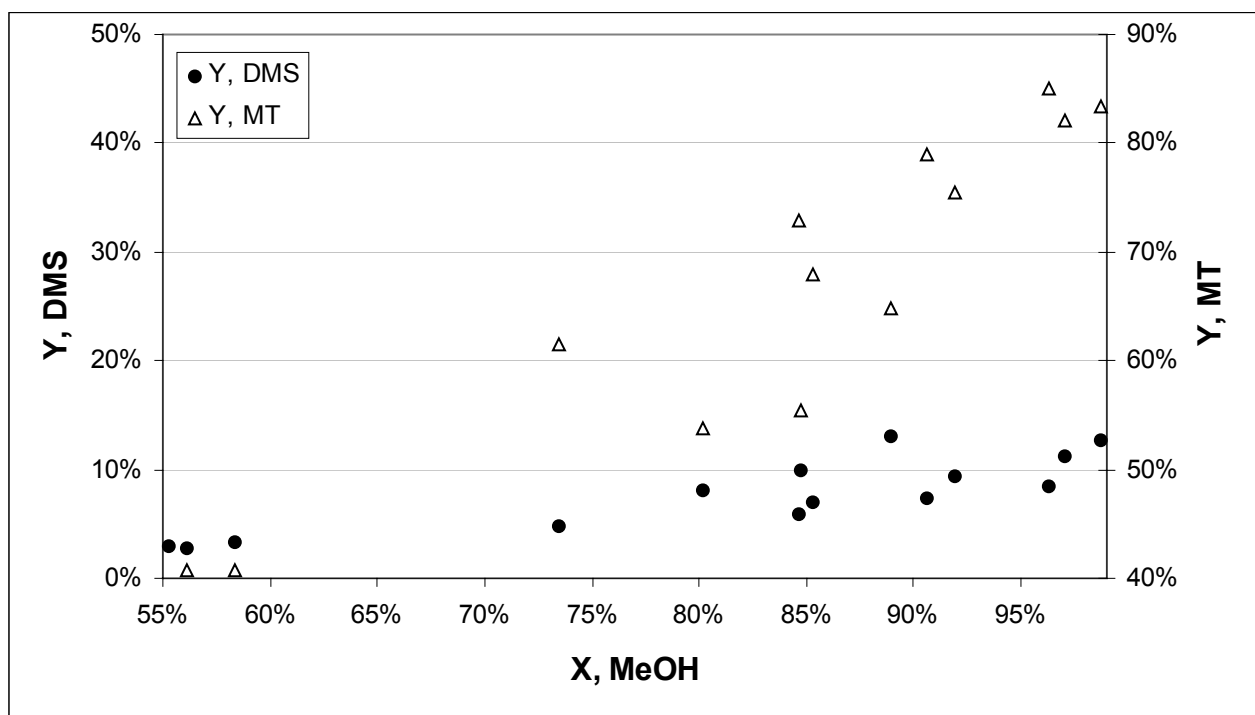


Figure 3.10. Yield to DMS and MT versus methanol conversion on $\text{WO}_3/\text{Al}_2\text{O}_3$.

Table 3.10. Performance of $\text{WO}_3/\text{Al}_2\text{O}_3$ with increasing temperature from 340-400°C. Space velocity for first four entries is 36-44 $\mu\text{mol}/\text{m}^2\text{-h}$, for second four it is 26-28 $\mu\text{mol}/\text{m}^2\text{-h}$ and for last four it is 14-16 $\mu\text{mol}/\text{m}^2\text{-h}$. To convert to WHSV, divide space velocity by 194. Three runs per data point.

Temp. (°C)	Feed Ratio	X, MeOH	X, H ₂ S	Y, SP	S, MT	A
340	0.70 ± 0.09	58 ± 5	29 ± 1	44 ± 4	93 ± 1	3.5 ± 0.1
360	0.61 ± 0.14	80 ± 9	35 ± 3	62 ± 10	87 ± 1	3.1 ± 0.1
380	0.74 ± 0.04	85 ± 3	45 ± 2	65 ± 1	85 ± 1	3.3 ± 0.1
400	0.66 ± 0.01	89 ± 1	47 ± 1	78 ± 1	83 ± 1	3.2 ± 0.1
340	0.33 ± 0.04	74 ± 5	21 ± 1	66 ± 5	93 ± 1	3.2 ± 0.1
360	0.32 ± 0.01	85 ± 2	25 ± 1	79 ± 2	92 ± 1	3.2 ± 0.1
380	0.34 ± 0.06	91 ± 5	28 ± 3	86 ± 6	91 ± 1	3.2 ± 0.1
400	0.31 ± 0.01	96 ± 2	28 ± 1	94 ± 2	91 ± 1	3.2 ± 0.1
340	0.47 ± 0.05	85 ± 5	34 ± 1	75 ± 5	91 ± 1	3.5 ± 0.1
360	0.46 ± 0.07	92 ± 5	37 ± 3	85 ± 7	89 ± 1	3.4 ± 0.1
380	0.42 ± 0.08	97 ± 2	37 ± 6	93 ± 3	88 ± 1	3.2 ± 0.1
400	0.43 ± 0.04	99 ± 1	38 ± 3	96 ± 2	87 ± 1	3.2 ± 0.1

increases from 40-96%, the average MT yield increases from 36-85%, and the average DMS yield increases from 3-11%.

At temperatures from 340-400°C, a feed ratio of 0.3-0.4, and space velocities from 6-8 $\mu\text{mol}/\text{m}^2\text{-h}$ (WHSV 0.05-0.06), $\text{MoO}_3/\text{SiO}_2$ produced MT at a selectivity of only 60-80%. Figure 3.11 shows that as the temperature increases over this range, the sulfur product yield varies from 45 to 68% and is highest at 360°C. Carbonyl sulfide is produced in varying amounts

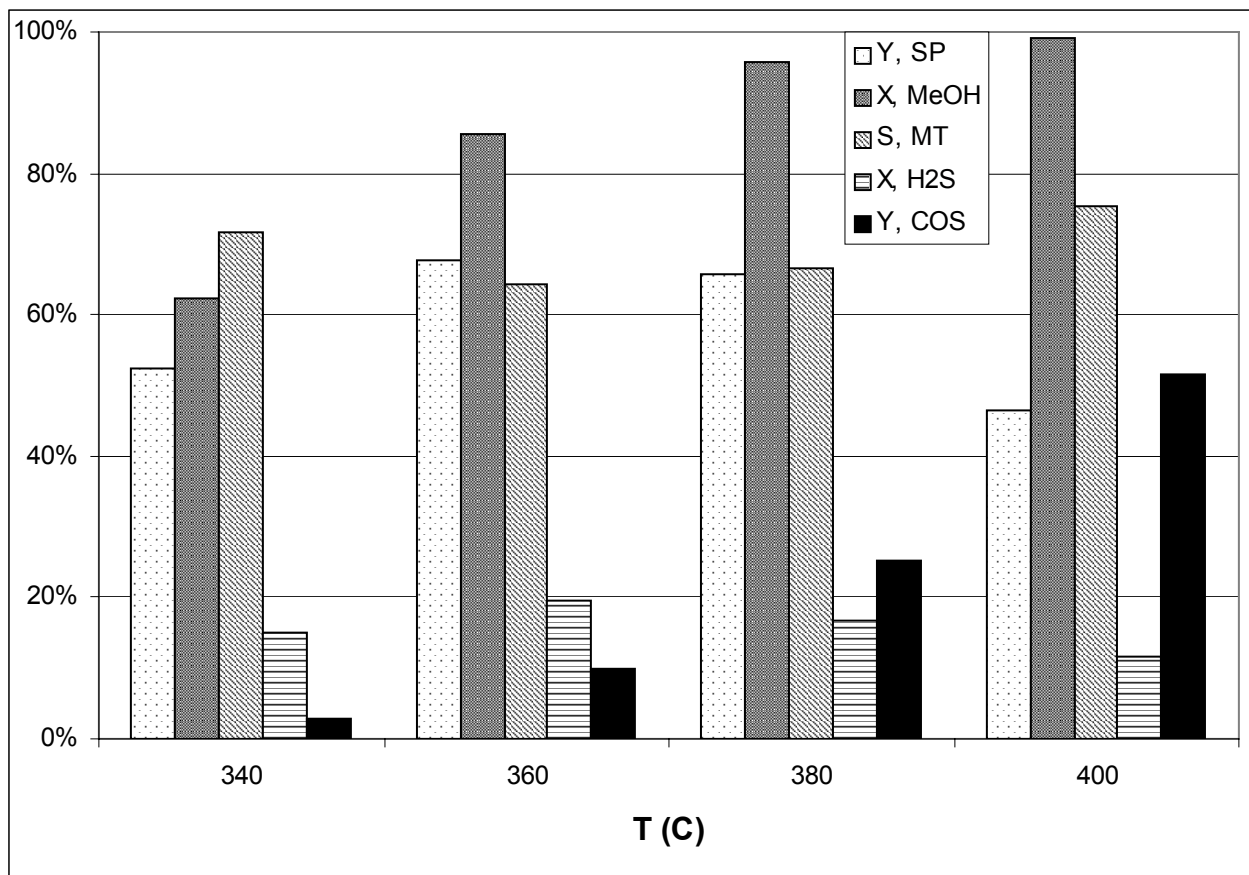


Figure 3.11. Performance of $\text{MoO}_3/\text{SiO}_2$ at different temperatures. Space velocity is 5 – 6 $\mu\text{mol}/\text{m}^2\text{-h}$. Feed ratio is 0.28 – 0.35.

and increases from 3 to 53% over this temperature range. Carbon disulfide and ethanethiol are also produced, and their yields increase with temperature. Since individual calibration curves for these compounds were not prepared, the carbon balance could be significantly in error when they are present in high concentrations in the effluent. Therefore, the quantities calculated from the carbon balance (space velocity, feed ratio, H_2S conversion) could also be significantly in error. But the obvious conclusion remains that supported MoO_3 is a poor catalyst for either MT or DMS production.

SAPO-18 and AIPO-18 were chosen to match the pore size of the catalyst (3.8 Å for these materials) to the molecular diameter of DMS (4.1 Å) in an attempt to achieve shape

selectivity to this product. The results for SAPO-18 are given in Table 3.11; SAPO-18 makes mostly DME. At 360-400°C, the catalyst converted 6-43% of the methanol to sulfur products at feed ratios of 1.0-2.2 and space velocities of 32-39 $\mu\text{mol}/\text{m}^2\text{-h}$ (WHSV 0.48-0.58). When the sulfur product yield was 6%, the MT selectivity was 63%. This selectivity decreased to 11% as the yield increased to 43%. The affinity for MT disproportionation (Table 3.11) is negative for feed ratios less than 1.4. At a sulfur product yield of 6%, 86% of the methanol had been converted to DME. The sulfur product yield increased with decreasing space velocity and increasing temperature, but the methanol conversion remained constant at 94-95%. At higher temperatures and feed ratios, the catalyst became very active for C3-C4 olefins after being on stream for about an hour. But after regeneration, this activity disappeared and the original activity was restored.

AlPO-18 was even less active to sulfur products, but more selective to DMS, than SAPO-18. From Table 3.12, the highest yield to sulfur products was 32% at a temperature of 400°C, a feed ratio of 2.9 and a space velocity of 16 $\mu\text{mol}/\text{m}^2\text{-h}$ (WHSV 0.24). The selectivity to MT was 47% when the sulfur product yield was 10% and dropped to 17% when the yield was 32%. Similar activity to DME was observed as for SAPO-18. The affinity for MT disproportionation (Table 3.12) was negative close to the reactor exit under all conditions.

Less than 1% of the methanol was converted to sulfur products by $\text{TiO}_2/\text{SiO}_2$, making it the least active catalyst among those studied. Reaction conditions were a temperature of 400°C, a feed ratio of 2.5 and a space velocity of 21 $\mu\text{mol}/\text{m}^2\text{-h}$ (WHSV 0.26). Some DME was produced, but it could not be accurately quantified due to the close proximity of the large methanol peak.

Table 3.11. Data for SAPO-18 with yield to hydrocarbons less than 10% at space velocities of 32-39 $\mu\text{mol}/\text{m}^2\text{-h}$ (0.48-0.58 h^{-1}). Three to six runs per data point.

Temp. ($^{\circ}\text{C}$)	Feed Ratio	X, MeOH	X, H ₂ S	Y, SP	S, MT	A
360	1.16 \pm 0.17	94 \pm 1	16 \pm 1	24 \pm 3	16 \pm 1	-2.7 \pm 0.2
360	1.40 \pm 0.18	94 \pm 1	14 \pm 2	13 \pm 2	59 \pm 2	0.2 \pm 0.2
360	2.09 \pm 0.20	94 \pm 1	11 \pm 1	6 \pm 1	63 \pm 3	0.1 \pm 0.2
380	0.96 \pm 0.19	95 \pm 1	23 \pm 2	43 \pm 5	11 \pm 1	-3.1 \pm 0.3
400	2.16 \pm 0.20	93 \pm 1	26 \pm 3	16 \pm 2	50 \pm 4	0.4 \pm 0.4

Table 3.12. Data for AlPO-18 at space velocities of 26-29 $\mu\text{mol}/\text{m}^2\text{-h}$ (WHSV 0.39-0.43 h^{-1}). Three runs per data point.

Temp. ($^{\circ}\text{C}$)	Feed Ratio	X, MeOH	X, H ₂ S	Y, SP	S, MT	A
360	1.24 \pm 0.07	93 \pm 1	9 \pm 1	10 \pm 1	47 \pm 1	-1.0 \pm 0.1
360	2.08 \pm 0.17	93 \pm 1	12 \pm 1	8 \pm 1	44 \pm 3	-0.8 \pm 0.2
400	1.21 \pm 0.08	94 \pm 1	19 \pm 1	25 \pm 2	28 \pm 1	-1.4 \pm 0.1
400	1.53 \pm 0.17	93 \pm 1	30 \pm 1	30 \pm 3	29 \pm 1	-0.7 \pm 0.1

3.2 Catalyst Deactivation

Catalysts were kept on-stream for two days, 8-10 hours a day, at typical operating conditions. After this, catalysts were regenerated overnight in 20-50 mL/min of air (STP) at temperatures of 400 $^{\circ}\text{C}$ for the mixed metal oxides and 500 $^{\circ}\text{C}$ for HZSM-5 (higher thermal stability than some of the mixed metal oxides). La₂O₃/Al₂O₃ and γ -Al₂O₃ did not show any sign of deactivation over the two-day period. HZSM-5 and WO₃/Al₂O₃ deactivated by about 8%

DMS/MT yield but were completely regenerated. WO_3/ZrO_2 deactivated by 10% DMS yield and was regenerated to within 5% of the original yield. The deactivation behavior of the other catalysts was not examined because they were not suitable for either DMS or MT production in the first place.

3.3 Acid Site Characterization

Data from the TGA experiments were normalized to the weight of the dry catalyst and the time derivative of weight was determined. By analyzing the derivative, the distribution of acid site strengths could be approximated by assuming that desorption of 1-propanamine or its Hoffmann elimination products propene and ammonia occurs on stronger sites at higher temperatures (Kanazirev et al., 1994). It should be noted that this method does not distinguish between LCs and PCs, since 1-propanamine can adsorb on both types of sites. All of the samples that were analyzed showed a low temperature desorption peak centered between 50 and 150°C, while HZSM-5, SAPO-18 and WO_3/ZrO_2 showed other peaks centered between 250 and 400°C. Any propanamine that did not desorb below 400°C was considered to be bound to strong acid sites that would definitely catalyze the elimination reaction based on previous studies. All catalysts had 2-6 mmol/m² of weak sites characterized by desorption below 200°C. $\text{TiO}_2/\text{SiO}_2$ showed a large number of sites at below 150°C, but it was inactive in the presence of MeOH and H₂S. Furthermore, the catalysts showing low activity had a large number of sites between 150 and 200°C, so weak sites characterized by propanamine desorption below 200°C are probably not active for any of the reactions studied here.

The number of acid sites desorbing 1-propanamine or its Hoffmann elimination products at >200°C is shown in Figure 3.12 for each catalyst. Comparing $\gamma\text{-Al}_2\text{O}_3$, $\text{La}_2\text{O}_3/\text{Al}_2\text{O}_3$, WO_3/ZrO_2 and HZSM-5 catalysts, it can be seen that they all have roughly the same number of

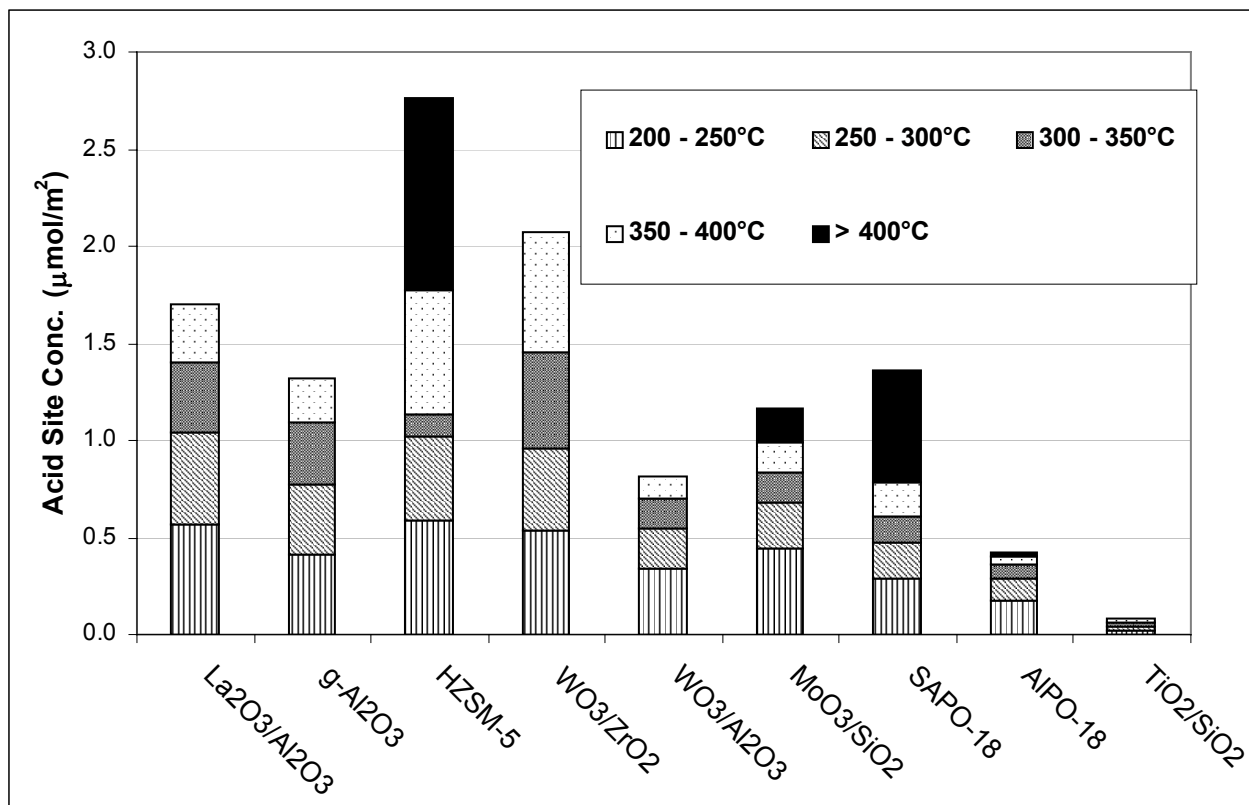


Figure 3.12. Concentration of acid sites determined by the desorption of propanamine in different temperature ranges.

sites that desorb between 200 and 400°C, the concentration being 1-2 $\mu\text{mol}/\text{m}^2$. Roughly 0.5 mmol/m^2 of sites are characteristic of the 200-250°C and 250-300°C ranges, although $\gamma\text{-Al}_2\text{O}_3$ has slightly fewer ($0.4 \mu\text{mol}/\text{m}^2$) in each range. HZSM-5 has a desorption peak centered in this region and it was found by Kanazirev et al. (1994) that this peak is due to the desorption of one molecule of propanamine from an acid site where two were initially adsorbed. Because there is no Hoffmann elimination associated with this desorption, the concentration of these sites probably does not correlate directly to reactivity.

Among the four active (to DMS) catalysts, the number of sites in the 300-350°C regime vary from 0.3 to 0.5 $\mu\text{mol}/\text{m}^2$, decreasing in the order $\text{WO}_3/\text{ZrO}_2 > \text{La}_2\text{O}_3/\text{Al}_2\text{O}_3 > \gamma\text{-Al}_2\text{O}_3 > \text{HZSM-5}$. This is the same order as was found for the activity of these catalysts for sulfur

products, indicating that sites desorbing in this range are probably the most active for DMS production. The number of sites in the 350-400°C range is between 0.2 and 0.6 $\mu\text{mol}/\text{m}^2$, decreasing in the order HZSM-5 > WO_3/ZrO_2 > $\text{La}_2\text{O}_3/\text{Al}_2\text{O}_3$ > $\gamma\text{-Al}_2\text{O}_3$. WO_3/ZrO_2 showed a desorption peak centered in this region while for HZSM-5 a desorption peak began in this region. Of this group, only HZSM-5 retains the reaction products of 1-propanamine at above 400°C, at a concentration of 1.0 $\mu\text{mol}/\text{m}^2$.

The group of catalysts $\text{WO}_3/\text{Al}_2\text{O}_3$, $\text{MoO}_3/\text{SiO}_2$, SAPO-18 and AIPO-18 have fewer sites desorbing between 200 and 400°C, ranging from 0.4-1.0 mmol/m^2 . The number of sites desorbing between 200 and 300°C ranges from 0.3-0.7 mmol/m^2 and decreases in the order $\text{MoO}_3/\text{SiO}_2$ > $\text{WO}_3/\text{Al}_2\text{O}_3$ > SAPO-18 > AIPO-18. These sites make up a larger fraction of the 200-400°C sites than for the previous group of four catalysts (60-70% compared with 50-60%). The number of sites desorbing from 300-350°C ranges from 0.1-0.2 mmol/m^2 , decreasing in the order $\text{MoO}_3/\text{SiO}_2 \sim \text{WO}_3/\text{Al}_2\text{O}_3$ > SAPO-18 > AIPO-18. Except for $\text{MoO}_3/\text{SiO}_2$, this follows the order of activity of these catalysts towards sulfur products. The number of sites desorbing from 350-400°C lies in the same range and decreases in the order SAPO-18 > $\text{MoO}_3/\text{SiO}_2$ > $\text{WO}_3/\text{Al}_2\text{O}_3$ > AIPO-18. SAPO-18 and $\text{MoO}_3/\text{SiO}_2$ both retained reaction products of 1-propanamine at above 400°C, 0.6 and 0.2 mmol/m^2 of propanamine respectively.

The $\text{TiO}_2/\text{SiO}_2$ catalyst desorbed very little 1-propanamine between 200 and 400°C, with 0.1 mmol/m^2 total sites distributed evenly among the temperature ranges. Nothing was retained at above 400°C.

CHAPTER 4

XAS CHARACTERIZATION OF METAL-DOPED SUPPORTED CERIUM OXIDE CATALYSTS

4.1 Background / Literature Review

Metal-doped supported cerium oxide catalysts are known to be active for the formation of ketones by the condensation of two carboxylic acids or an acid and aldehyde (Bhat, 2004). Similar catalysts are active for the condensation of methanol and H₂S (see Ch. 3). The acid condensation reaction is thought to proceed by adsorption of the carboxyl oxygens onto exposed cerium atoms at the catalyst surface. The alpha C-H bond is weakened by donating electron density to another or the same exposed cerium atom, and the bond dissociates to form a ketene-like intermediate where electron density is transferred from the pi bond with the alpha carbon to the cerium atom. It is then thought that the electrons in the pi bond of the ketene intermediate attack the carboxyl carbon atom of another adsorbed acid molecule to form a C-C bond. This species then decomposes to form the ketone, CO₂, and water.

Since the doping of cerium oxide with certain transition metal atoms alters the activity and selectivity of the catalysts for these reactions (Bhat, 2004), it was desired to determine the location of dopant atoms in the catalyst, and their effect on the formation of oxygen vacancies in the cerium oxide lattice, which are necessary for ketonization. This was investigated by X-ray absorption spectroscopy (XAS) using synchrotron radiation provided by the XMP and DCM beamlines operating off the electron storage ring at the Center for Advanced Microstructures and Devices (CAMD) in Baton Rouge, Louisiana. Characterization of the catalysts was done using the XANES and EXAFS regions of the spectra.

The techniques of Extended X-ray Absorption Fine Structure (EXAFS) and X-ray Absorption Near Edge Structure (XANES), together called XAS, can be used for ex-situ and in-

situ study of the electronic and structural properties of catalysts. XANES describes excitations of core electrons on the absorbing atom into low-lying unoccupied states. In insulating materials, such as the ones examined in this work, the potential arising from the core hole is not screened like it is in metals and localized orbitals arise in the final state that are bound to this potential. These states have sharply defined energies and when the core electron is excited to these orbitals, an intense peak occurs in the absorption spectra – this is called a white line (Fernandez-Garcia, 2002). XANES excitations obey the usual dipole selection rules in which the orbital angular momentum quantum number changes by ± 1 . Transitions allowed by quadrupole coupling (the orbital angular momentum quantum number changes by ± 2) are also allowed but have much weaker cross sections (intensities) than the dipole allowed transitions.

It is a general feature of XANES that the position of the absorption edge decreases as electron density (corresponding to oxidation state) on the absorbing atom increases (Fernandez-Garcia, 2002). In the K-edge XANES spectra of insulating materials, a white line appears that corresponds to an electron being excited from a 1s orbital to a localized p orbital (Fernandez-Garcia, 2002). A weak pre-edge peak appears corresponding to the quadrupole allowed $1s \rightarrow d$ transition. The intensity of this peak is proportional to the density of unoccupied d states on the absorbing atom. If the absorbing atom is in a tetrahedral crystal field, the $1s \rightarrow d$ transition becomes dipole-allowed and the absorption cross section increases significantly. In the L_{III} edge XANES of insulating materials, a white line appears that corresponds to an electron being excited from a $2p_{3/2}$ orbital to a localized d orbital (Fernandez-Garcia, 2002). As with the pre-edge peak of K-edge XANES, the intensity of this white line is proportional to the density of unoccupied d states on the absorbing atom.

EXAFS describes how core electrons excited into the continuum scatter off nearby atoms. From this scattering, the structure of the coordination shell around the absorbing atom can be determined. In contrast to classical scattering techniques, EXAFS does not require long range ordering, making it suitable for the investigation of doped rare earth oxides, since both the rare earth ion and the corresponding dopant ion can be investigated separately.

The L_{III} XANES of CeO_2 shown in Figure 4.1 arises from the excitation of a $2p_{3/2}$ core electron to an empty $5d$ orbital. The two white lines in the spectrum reflect the mixed valence initial state of Ce with formal valence IV (Bianconi et al., 1987). In this state, the energy of a singly occupied $4f$ orbital is only 0.1 eV above the top of the valence band, which is primarily of O $2p$ character (Figure 4.2). There is hybridization between the two states, giving a valence band of mixed Ce $4f$ and O $2p$ character. This hybridization only occurs for one spin state

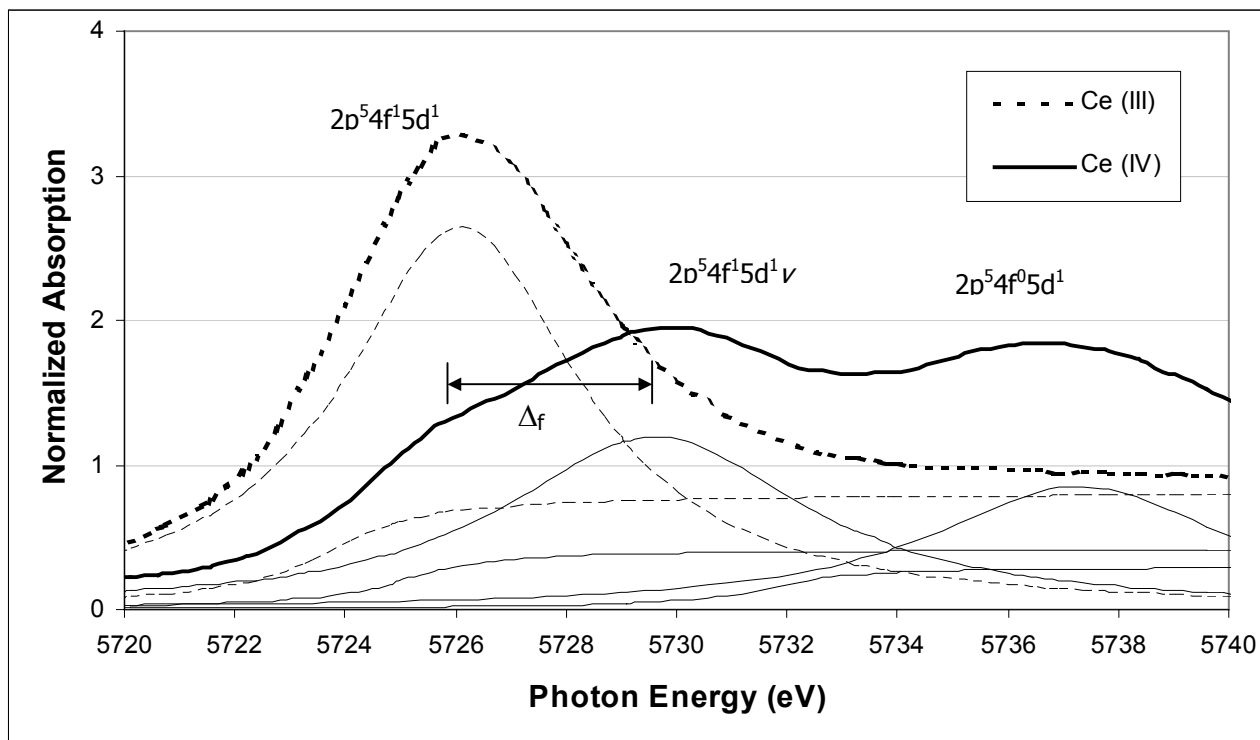


Figure 4.1. Ce L_{III} XANES spectra of CeO_2 and Ce_{III} acetate. The peaks are labeled with the corresponding excitation and the crystal field splitting of the d orbitals is shown as Δ_f . The Lorentzian and arctangent functions used in the Takahashi method are also shown for each peak.

because of a large Hubbard U term (10.5 eV) (Bianconi et al., 1987). When the 4f orbitals of one spin are partially occupied, the energy of the 4f orbitals of the opposite spin are increased by an amount that is proportional to the occupancy of the former, the constant of proportionality being the Hubbard U . Thus the orbitals of the opposite spin are much higher in energy than the top of the valence band and do not hybridize with it.

The perturbation of the core hole decreases the energy of the 4f orbitals by an amount $Q_{hf} = -12.5$ eV (Bianconi et al., 1987), putting them 4.4 eV below the bottom of the valence band when repulsion with the excited electron in a 5d orbital is considered. Since there is no longer hybridization between the 4f orbital and the valence band, two final states exist that couple to the

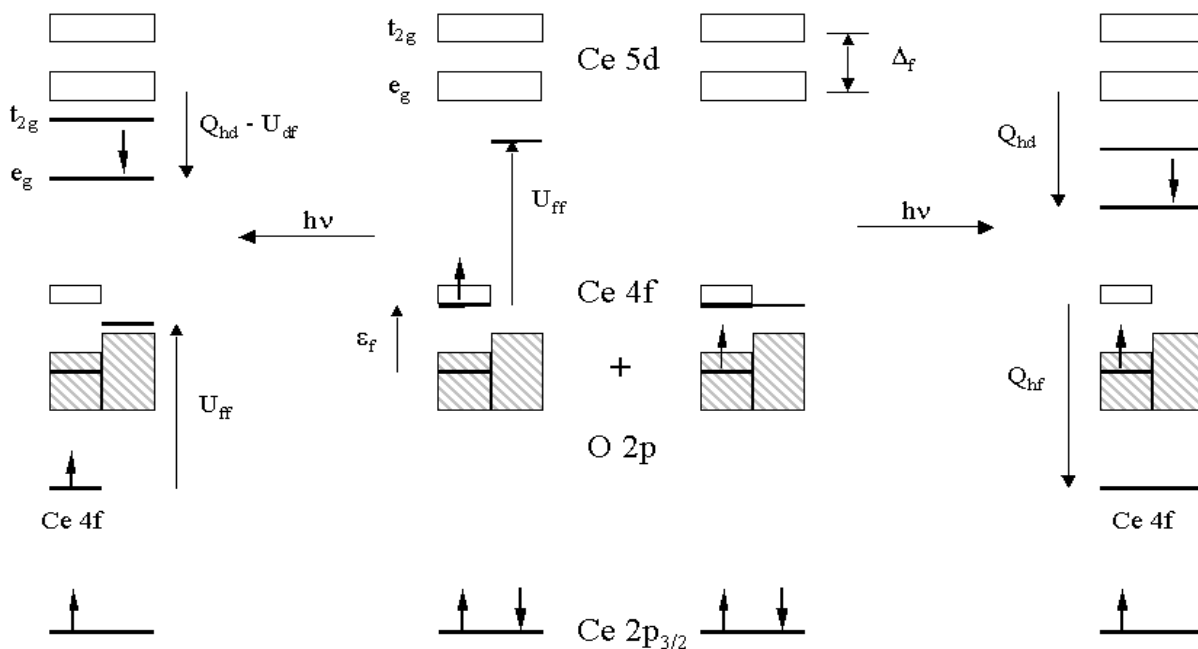


Figure 4.2. Initial and final states of a Ce(IV) atom corresponding to an L_{III} transition. Boxes represent filled and unfilled bands. Lines represent states localized at the absorbing atom. The initial state is a combination of the two states in the center. Two of the final states are shown at the edges. Note that two other final states are possible with the core electron excited to the higher energy t_{2g} d orbital. U_{ff} (10.5 eV) is the Hubbard U for the f-orbital, Q_{hd} (-6 eV) and Q_{hf} (-12.5 eV) are the attractions between the core hole and the d and f orbitals, respectively. U_{df} (5 eV) is the repulsion between the d- and f- orbitals on an excited Ce atom. ϵ_f (1.6 eV) is the energy difference between the unhybridized f-orbital and the center of the valence band, which has a bandwidth of 3 eV.

initial state by the excitation. In the lower energy state, labeled in Figure 4.1 as $2p^5 4f^1 5d^1 \underline{\nu}$, an electron occupies the 4f orbital and a hole is present in the valence band. The other state, $2p^5 4f^0 5d^1$, is higher in energy by 7.4 eV and arises from an empty 4f orbital and an additional electron in the valence band. In addition to these two features, a shoulder is present due to the crystal field splitting (3.7 eV) of the Ce 5d orbitals (Soldatov et al., 1994). This splitting manifests itself by allowing four final states, since the excited electron can now go into two 5d orbitals for each of the two states that exist without the crystal field.

When an oxygen vacancy exists in the CeO_2 lattice, an additional electron must occupy the 4f orbital on two of the four Ce atoms neighboring the vacancy. In order to accommodate the extra electron, the 4f orbital on the Ce atom dehybridizes and the electron that partially occupied it excites to the valence band to avoid repulsion with the new electron. Since the initial state of the Ce atom is no longer of mixed valence character, only one final state couples with it and only one white line is present in its XANES spectrum, labeled $2p^5 4f^1 5d^1$ in Figure 4.1. This excitation requires approximately 4 eV less energy than the excitation in Ce_{IV} to the $2p^5 4f^1 5d^1 \underline{\nu}$ state.

Nachimuthu et al. (2000) studied the effect of crystal size on the XANES spectra of CeO_2 nanoparticles. They found that as the particle size increases, the two main white lines shift to higher energy and the amplitude of the peak corresponding to the $2p^5 4f^1 5d^1 \underline{\nu}$ final state increases relative to the peak corresponding to the $2p^5 4f^0 5d^1$ final state. In addition to this, the shoulder arising from crystal field splitting shifts to lower energy and increases in intensity. They attribute these differences to an increase in O 2p-Ce 4f hybridization in the initial state with increasing crystal size. The increase in hybridization lowers the energy of the initial state

relative to those of the final states (since hybridization is not present in the final states), increasing the photon energy required to make this transition.

There are several studies in the literature where XAS was used to characterize CeO₂ doped with transition metals. Skarman et al. (2002) have used XANES and EXAFS to characterize nonstoichiometric CuO_x/CeO₂ composite particles, 4.9-29.4% Cu. The pre-edge in the XANES spectrum, specific to Cu(I) species (Kau et al., 1987), was used to evaluate the ratio of Cu⁺¹ to Cu²⁺, which varied from 0.36 in fresh samples to less than 0.05 in the activated samples. EXAFS showed a Cu-Cu distance varying from 2.89 to 2.85 Å, corresponding to a low coordination number between 0.4 and 0.3. This showed that the copper was very dispersed. Also the EXAFS analysis showed that in the activated catalysts the Cu species were generally in lower coordination, suggesting that Cu ions migrate to the surface.

El Fallah et al. (1994) studied the reducibility of pure and rhodium doped CeO₂ catalysts with Ce L_{III} XANES, thermogravimetric analysis (TGA), and N₂O adsorption. They found that the degree of reduction determined by XANES agreed well with TGA data. By using all three methods of analysis, the reduction kinetics of CeO₂ and Rh/CeO₂ catalysts in H₂ at temperatures of 400 – 500°C were determined. Ceria reduction occurs through a surface step, probably H₂ dissociation, followed by a much slower bulk diffusion step. The presence of rhodium greatly accelerated the rate of the surface step. At 400°C, about 20% of the cerium was reduced to the Ce(III) state in both samples, but while this occurred almost instantaneously for the rhodium doped sample, it took 30 min for the undoped catalyst.

Priolkar et al. (2002) used EXAFS, XPS, and XRD to characterize a palladium doped CeO₂ catalyst synthesized by the combustion method. High resolution XRD showed that no Pd metal or PdO phases were present in the 1 at. % Pd/CeO₂ catalyst, indicating that the two

components form a solid solution at this composition. By the same method, 3 at.% metallic Pd was detected in 5 at.% Pd/CeO₂, indicating that about 2 at.% Pd is soluble in CeO₂. Rietveld analysis suggested that the undoped CeO₂ has 3.5% oxygen vacancies, 1 at.% Pd/CeO₂ has 5% vacancies, and 5 at.% Pd/CeO₂ has 6.5% vacancies. XPS of Pd (3d) and Pd K XANES showed that Pd was in a highly ionic Pd(II) state in the 1 at.% Pd/CeO₂ catalyst, while in the 5 at.% Pd/CeO₂ catalyst, Pd is present in both the Pd(II) and metallic states. EXAFS of the 1 at.% Pd/CeO₂ catalyst shows that Pd²⁺ ions are substituted for Ce⁴⁺ sites with an oxide vacancy near the Pd²⁺ ion necessary to maintain charge neutrality.

Norman et al. (2001) studied the reducibility of ceria-zirconia catalysts doped with platinum or palladium using XANES of the Ce (L_{III}) edge along with magnetic susceptibility measurements. Measurements of the extent of Ce(IV) reduction to Ce(III) by both methods agreed. It was found that at less than 500°C the addition of a noble metal accelerated reduction in hydrogen. Reduction occurred at room temperature for Pd and at 200°C for Pt because the PtO_x itself was not reduced below this temperature. The reduction that occurred at these temperatures was attributed to the dissociation of H₂ to form surface hydroxyls. At higher temperatures, water desorbs from the surface leaving vacancies that irreversibly migrate into the bulk. At these temperatures, the reduction behavior of doped and undoped catalysts was similar except for a monolayer of hydroxyls on the surface of the doped catalysts. When the catalysts were heated in vacuum to high temperatures, doped and undoped catalysts reduced similarly.

4.2 Experimental

All catalyst samples were mixed with boron nitride as a filling agent and pressed into wafers giving a baseline absorbance of 4–5. The wafers were placed into an XAS cell and heated to 420°C in nitrogen, at which point a scan was taken. A mixture of 10% H₂/N₂ was then

introduced into the cell for 15 min and another scan taken. These conditions were chosen to reflect the operating conditions of the catalyst. For the Co-containing samples, the cell was then cooled to room temperature in nitrogen and Co K-edge EXAFS spectra collected. A XANES scan was taken at room temperature in fluorescence mode of the Pd L_{III} edge for the Pd-containing samples, supported on Kapton tape. The spectra in transmission mode were obtained using ionization chambers measuring the incident beam intensity before and the transmitted beam intensity after the sample cell. In fluorescence mode, a 13-element Ge detector array and Si (111) double-crystal monochromator were used to obtain K K-edge, Pd L_{III}-edge, and Ce L_{III}-edge spectra, while a Si (311) monochromator was used for Co K-edge spectra. The raw data were first reduced to $\mu(E)$, the absorption coefficient. It was calculated using the following equations.

$$\mu(E) = \log(I_0 / I) \quad - \text{Transmission mode,}$$

$$\mu(E) = I_f / I_0 \quad - \text{Fluorescence mode,}$$

where I_0 is the incident X-ray intensity, I the transmitted intensity, and I_f the averaged intensity of a fluorescence line. Parameters for all runs are shown in Table 4.1.

4.3 Analysis

Two methods were used to determine the number of oxygen vacancies from the XANES data: (1) the method of Takahashi et al. (2002); (2) linear fits using the WinXAS package (Ressler, 2004). Takahashi et al. used physical mixtures of Ce_{III} oxalate and Ce(SO₄)₂ to derive a linear correlation relating the relative amount of Ce(III) in the mixture to the XANES spectrum. This was done by fitting each white line (one for Ce_{III} and two for Ce_{IV}) with a Lorentzian and an arctangent as shown in Fig. 4.1. The centers of each function were fixed relative to each other, and the width of each function was also set according to the pure standards. The relative

Table 4.1. Experimental parameters for all XANES and EXAFS runs.

	Resolution (eV)	Range (eV)
Cerium L _{III} -edge (Transmission)		
XANES	3.0	5525-5710
	0.3	5710-5785
	3.0	5785-5985
EXAFS	3.0	5525-5710
	2.0	5710-6145
XANES + EXAFS	3.0	5525-5710
	0.3	5710-5785
	2.0	5785-6164
Cobalt K-edge (Transmission)		
XANES + EXAFS	3.0	7550-7695
	0.3	7695-7770
	2.0	7770-8700
Cobalt K-edge (Fluorescence)		
XANES	3.0	7559-7689
	0.3	7689-7739
	3.0	7739-8000
EXAFS	3.0	7559-7690
	2.0	7690-8700
Palladium L _{III} -edge (Fluorescence)		
XANES	3.0	3050-3160
	0.3	3160-3240
	3.0	3240-3400

amplitudes of the two white lines in Ce_{IV} were also fixed. Three parameters were varied during the fit, the edge position and the amplitudes of Ce_{III} and Ce_{IV}. The correlation fit the relative amount of each valence state to the area under the corresponding Lorentzians. It is assumed that the XANES spectrum of a Ce_{III} atom adjacent to an oxygen vacancy in reduced CeO₂ is similar to Ce_{III} in the oxalate, and that the spectrum of Ce_{IV} in CeO₂ is the same as in Ce(SO₄)₂. It is difficult to assess the first assumption without performing theoretical calculations on a defective CeO₂ lattice. The second assumption can be evaluated by comparing the spectra of CeO₂ to Ce(SO₄)₂. When this is done, it is seen that the shoulder present in CeO₂ due to the crystal field

splitting is not present in $\text{Ce}(\text{SO}_4)_2$, so the amount of Ce_{III} in supported cerium oxides will be overestimated by the Takahashi et al. method.

WinXAS (Ressler, 2004) was also used to calculate the relative amounts of the two valence states by matching the XANES spectra to linear combinations of the spectra of CeO_2 and Ce_{III} acetate standards. The assumption here is the same as the first assumption of the Takahashi et al. method. Additionally, it is assumed that Ce atoms in the catalyst, which are mostly present on or near the surface, give the same spectra as in the bulk. Since it was found that both the shoulder and the lower energy white line are more intense in larger crystals (Nachimuthu et al., 2000), this method underestimates the amount of $\text{Ce}(\text{III})$ in the catalysts, where CeO_2 is present in almost monolayer coverage. Recall that these features are at energies close to that of the $\text{Ce}(\text{III})$ white line. Therefore, the number of oxygen vacancies predicted by the Takahashi et al. and WinXAS methods should bound the actual number.

EXAFS data for the Co K-edge were fitted using WinXAS and Artemis (Ravel and Newville, 2004) to theoretical spectra of a Co atom substituted into a CeO_2 lattice generated by the FEFF6 package (Zabinski et al., 1995). The standard EXAFS scattering equation (Thomas and Thomas, 1997) was used for the fitting, given by

$$\chi(k) = \sum_j \frac{N_j}{kR_j^2} \cdot F_j(k) \cdot \exp(-2k^2\sigma_j^2) \cdot \sin[2kR_j + 2\delta_j(k)]$$

where the sum is over all coordination shells j , N_j is the coordination number, R_j is the distance, σ_j is the Debye-Waller factor of the j^{th} shell. $F_j(k)$ is a factor that accounts for electron back-scattering and inelastic scattering and $\delta_j(k)$ is the phase shift of the scattered wave – both of these depend on the atomic number of the scattering atom. $\chi(k)$ is the EXAFS function defined as

$$\chi(k) = \frac{\mu - \mu_0}{\mu_0}$$

where μ is the absorption coefficient of an atom in the material, μ_0 is the absorption coefficient of an atom in the free state, and k is the wave vector given by

$$k = \frac{(2mE)^{1/2}}{\hbar} = \left[\frac{2m(\hbar\omega - E_b)}{\hbar} \right]^{1/2}$$

where E is the electron kinetic energy, m is the electron mass, $\hbar\omega$ is the energy of the absorbed photon, and E_b is the initial binding energy of the electron.

Data were fitted in the R-space range of 0.9–4.8 Å derived from the Fourier-transformed region of k-space from 3.0–9.4 Å⁻¹. The EXAFS function, $\chi(k)$, was determined from the absorbance, $\mu(E)$, by subtracting background Fourier components of less than 1.0 Å. In the fit done in Artemis, the spectra were further refined by including background parameters in the fitting process. The k-, k²- and k³-weighted spectra of each set were simultaneously fit to reduce correlation between coordination number and Debye-Waller factors in Artemis. In WinXAS, only k- and k²-weighted spectra were used. In Artemis, the goodness of the fit was determined by the r-factor; in WinXAS the residual was used. These are defined as follows:

$$r - factor = \sum_{i=1}^{N_{pts}} \frac{[\text{Re}(\chi_{dat}(R_i) - \chi_{th}(R_i))]^2 + [\text{Im}(\chi_{dat}(R_i) - \chi_{th}(R_i))]^2}{[\text{Re}(\chi_{dat}(R_i))]^2 + [\text{Im}(\chi_{dat}(R_i))]^2}$$

$$residual = \sum_{i=1}^{N_{pts}} [\text{Re}(\chi_{dat}(R_i) - \chi_{th}(R_i))]^2 + [\text{Im}(\chi_{dat}(R_i) - \chi_{th}(R_i))]^2$$

where the sum runs over all N_{pts} data points in R-space, $\chi_{dat}(R)$ is the experimental EXAFS function in R-space, and $\chi_{th}(R)$ is the theoretical EXAFS function.

The fitting model included parameters for the radial distances, Debye-Waller factors of the first five shells, and the coordination numbers in the first oxygen shell. For the initial theoretical model, half of the Ce atoms in the second shell were substituted with Co atoms; the

numbers of each atom were allowed to vary during the fit. A different radial distance was used for the Ce and Co sub-shells but the same Debye-Waller factor was used. The coordination number of oxygen atoms in the third shell was highly correlated with the Debye-Waller factor. To produce a reasonable fit for this shell, the coordination number was fixed at 21 (3 vacancies) during the fitting procedure since XANES indicates approximately this number in the bulk. The coordination numbers of the fourth and fifth shells were fixed at 6 and 24 respectively. The electron amplitude reduction factor (0.9) was determined by fitting a Co foil standard in WinXAS.

Scattering paths with up to four coplanar legs were included in the model. WinXAS automatically correlates the parameters for the multiple scattering (MS) paths to those of the single scattering (SS) paths. In Artemis, the amplitudes of the MS paths were assumed to vary proportionally with the coordination number for each atom in the path. The path lengths for MS paths were determined from the SS path lengths by assuming the scattering angle does not change with path length. The Debye-Waller factors for MS paths were taken as the average of the Debye-Waller factors for each atom in the path.

4.4 Results and Discussion

Normalized Ce L_{III} XANES of the 0.8% Co doped catalyst are shown in Figure 4.3 at room temperature, at 420°C in N_2 , and at 420°C in the H_2/N_2 mixture. It can be seen that at room temperature, the spectrum is similar to that of the CeO_2 standard. When the catalyst is heated in N_2 to 420°C, the intensity of the lower energy white line increases and that of the higher energy white line decreases. When the catalyst is reduced in H_2/N_2 at this temperature, the spectrum changes little compared to the changes caused by heating in N_2 . From these

spectra, it appears that the number of oxygen vacancies is mainly affected by temperature and doping, but not significantly by the gas atmosphere.

Normalized Ce L_{III} XANES of the reduced (at 420°C) CeO₂ catalysts are shown in Figure 4.4. These catalysts contained 17 wt.% CeO₂ supported on Al₂O₃. The parent catalyst was a 1.59 mm extrudate of BET surface area 158 m²/g, and was prepared by incipient wetness impregnation (Hendren and Dooley, 2003). The doping was also by impregnation and further details are found in Bhat (2004). It can be seen that the catalyst containing 0.8% Co has a higher peak corresponding to the Ce(III) state than does the undoped sample, but the catalyst containing 2.4% Co has a lower peak. Bhat (2004) could not find a general correlation between the number of vacancies as determined by Ce L_{III} XANES and the catalyst activity for a difficult ketonization reaction such as the condensation of isobutyric acid to diisopropylketone, although he did find that for a given dopant metal such as Co an increased number of vacancies resulted in increased ketonization activity.

This trend in the XANES data is also reflected in the average number of oxygen vacancies in the coordination shell adjacent to each Ce atom (8 maximum oxygen atoms) shown in Figure 4.5. It can also be seen that the two methods of quantification (Takahashi vs. WinXAS) agree closely. The sample doped with 3% K₂O showed the least amount of reduction, at these conditions, having 0.2–0.4 oxygen vacancies in the cerium coordination shell. The catalyst doped with 2.4% Co had 0.4–0.6 oxygen vacancies, still less than the undoped sample which had 0.7–0.9 vacancies. This corresponds to an empirical formula of ~CeO_{1.8} for the cerium oxide phase at these conditions, which corresponds closely to empirical formulas determined under similar reducing conditions for CeO₂/Al₂O₃ in TGA experiments (Randery et al., 2002). Doping with 0.8% Pd slightly increased the extent of reduction, giving 0.9–1.0

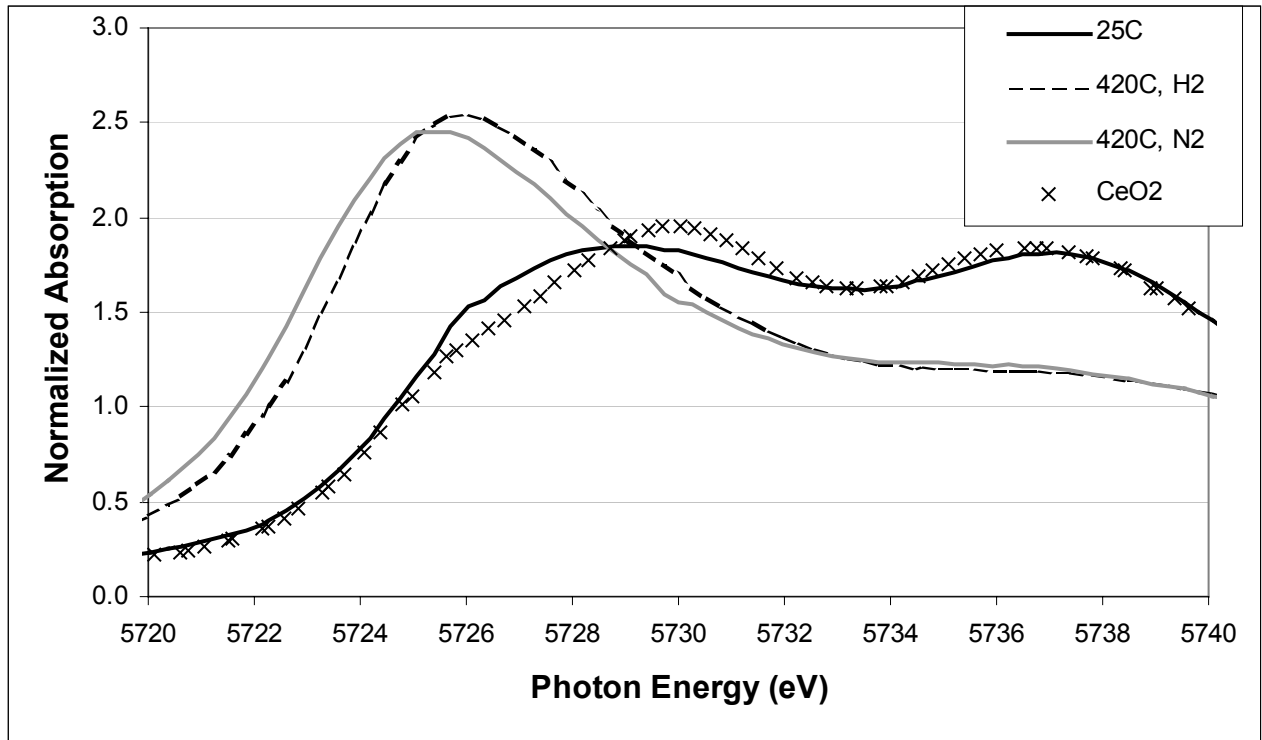


Figure 4.3. Normalized Ce L_{III} XANES of pure and doped catalysts at different stages of reduction.

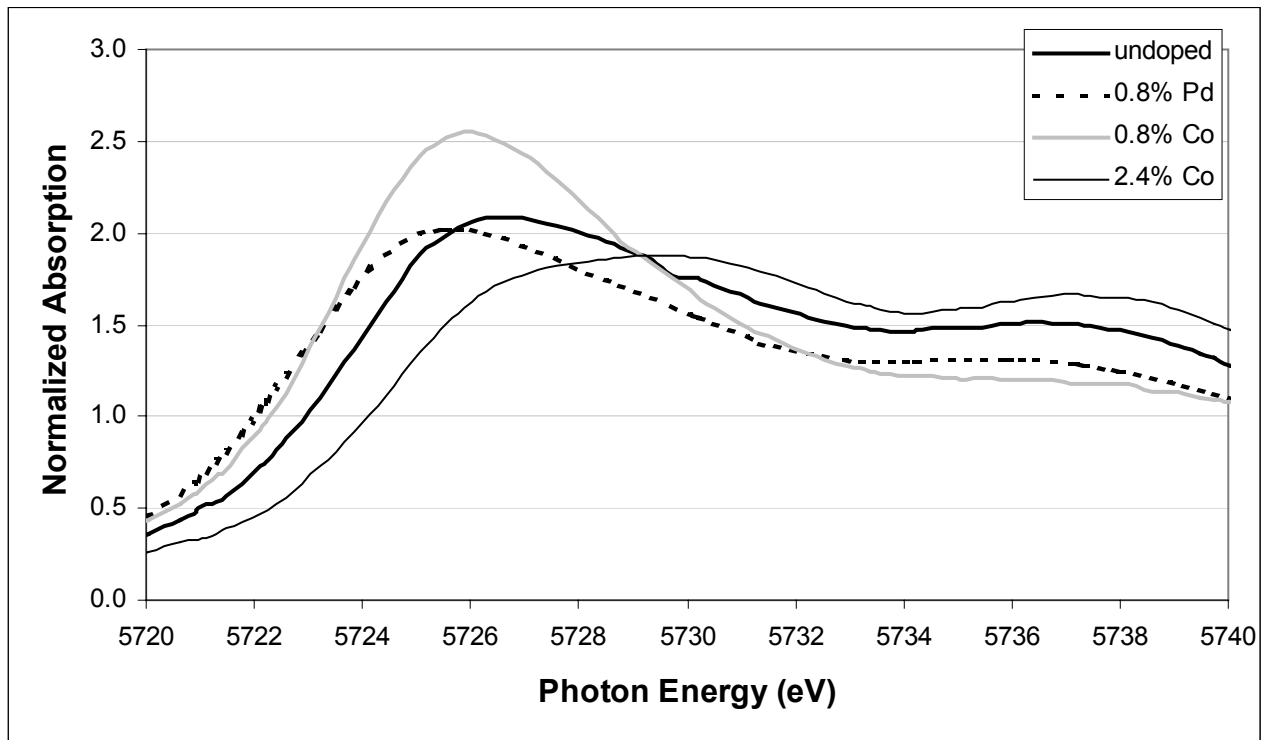


Figure 4.4. Normalized Ce L_{III} XANES of pure and doped CeO₂/Al₂O₃ catalysts reduced in 10% H₂/N₂ at 420°C for 15 min.

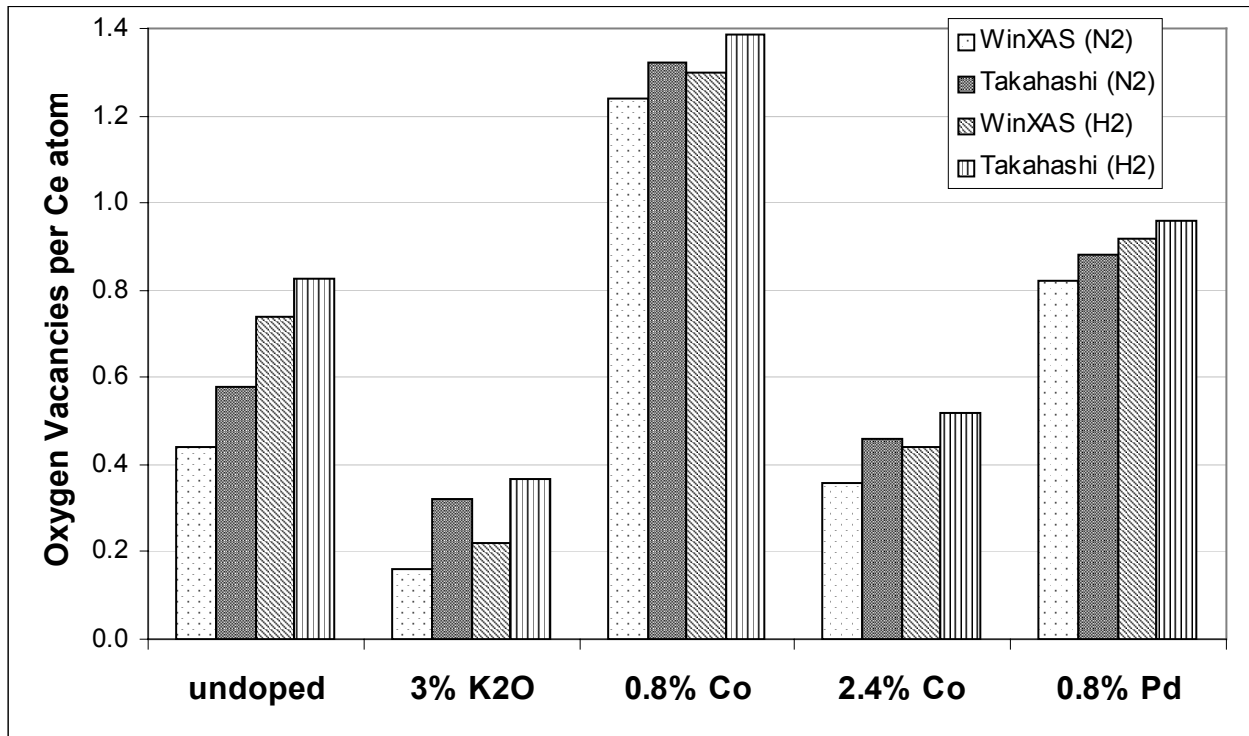


Figure 4.5. Average number of oxygen vacancies around each cerium atom as determined by XANES using the Takahashi and WinXAS methods.

vacancies, and doping with 0.8% Co resulted in the greatest extent of reduction with 1.2–1.4 vacancies. This catalyst was the most active ketonization catalyst of all those tested by Bhat (2004), at least in the short term (first few days). Since samples were reduced in H₂ for only 15 min and probably not brought to equilibrium, it is more likely that the changes in reducibility are kinetic in origin, although there are insufficient kinetics data to confirm this.

The XANES spectra taken at the Co K-edge for both the 0.8% and 2.4% Co-doped catalysts are shown in Figure 4.6. There is a main peak at 7728 eV and one shoulder about 4 eV lower and another about 8 eV lower. The main peak corresponding to the 1s → 4p white line in CoO (Huffman et al., 1995) is less intense in the spectra of the catalysts. These deviations from the CoO spectrum indicate that the cobalt is in a different electronic state in the catalyst, probably due to substitution of Co for Ce in the CeO₂ lattice with tetrahedral oxygen

coordination. Analysis of the EXAFS rules out the possibility that a significant portion of the cobalt is in a separate CoO or metallic phase. Bhat (2004) found that hydrogen does not adsorb on these catalysts at 150°C, also ruling out the existence of a separate CoO or metallic phase.

Ab-initio calculations (see section 1.5 for details) carried out using Gaussian 03 (Frisch et al., 2004) were performed on a Ni^{3+} ion (to model a Co^{2+} ion with a core hole) placed in both tetrahedral and octahedral crystal fields to determine if the differences between the catalyst and CoO spectra could be explained by crystal field effects (CoO has octahedral coordination). The crystal field was modeled by placing four or six negative point charges (each having one atomic unit of charge) in tetrahedral or octahedral positions 2.0 Å from the nickel ion. Calculations were performed using the Hartree-Fock method and the STO-3G basis set. In octahedral coordination, there were three nearly degenerate unoccupied orbitals with 4p character at 23 eV. This would result in the single white line observed in the CoO spectrum. When placed in the tetrahedral crystal field, the energies of the three orbitals with 4p character split evenly over a range from 7-11 eV. Errors in the wavefunction that arise from ignoring electron correlation and errors associated with using the minimal STO-3G basis set should not influence the order of magnitude of the crystal field splitting which is mainly determined by the symmetry and strength of the crystal field potential. While the crystal field potential in the real crystal probably has a different strength than the one in the model, the order of magnitude should be the same. Since the splitting of the 4p orbitals is expected to be roughly proportional to the strength of this potential, it is a reasonable conclusion that the splitting in the tetrahedral field is of the same order of magnitude as the predicted splitting.

It can also be seen in the expanded inset of Figure 4.6 that the pre-edge peak associated with the dipole forbidden $1s \rightarrow 3d$ transition is more pronounced in the catalysts than in the CoO

standard. This could arise from a lower occupancy of d states or from increased coupling with the initial state due to tetrahedral (compared to octahedral in CoO) oxygen coordination (Fernandez-Garcia, 2002). The second explanation is supported by EXAFS that show the Co atom to be substituted for a Ce atom in the CeO₂ lattice coordinated by four oxygen atoms.

The XANES spectra for the Pd L_{III} edge shown in Figure 4.7 indicate that Pd in 0.8% Pd/CeO₂/Al₂O₃ is in the II formal valence state. Since the catalyst had been previously calcined at high temperature where Pd would be expected to reduce to the metal, the Pd would not be in this state unless it was substituted into the CeO₂ lattice. It is also seen that the white line due to the 2p → 4d transition (Priolkar et al., 2002) is more intense for this catalyst than for a PdO standard, possibly arising from an increased density of unoccupied d-states that would indicate less hybridization of these states with the valence band (Fernandez-Garcia, 2002).

The Co EXAFS spectra in k- and R-space for the Co-doped CeO₂/Al₂O₃ catalysts are shown in Figures 4.8 and 4.9; the fitting parameters are given in Tables 4.2 and 4.3. The first five coordination shells expected for Co doped into a CeO₂ lattice appear in the spectra. It was found that close to half of the Ce atoms in the second shell are substituted by Co, indicating that the dispersion of Co within the lattice is not homogeneous. This is in agreement with the XANES results suggesting at least some CoO phase. Also, there appear to be about four oxygen atoms in the first coordination shell of Co, compared to six for CoO. For both samples, fitting using either the WinXAS or Artemis packages gave similar numbers. For 0.8% Co, Artemis gave E₀ (edge shift) of -2.8 ± 4.4 eV and an r-factor of 0.0020; WinXAS gave E₀ of -5.8 ± 0.1 eV and a residual of 6.4. For 2.4% Co, Artemis gave E₀ of -2.4 ± 5.4 eV and an r-factor of 0.0036; WinXAS gave E₀ of -6.4 ± 0.02 eV and a residual of 10.0. It is not clear why the

uncertainties for the parameters fitted by Artemis are more than an order of magnitude higher than those computed by WinXAS, while the fitting results are so similar.

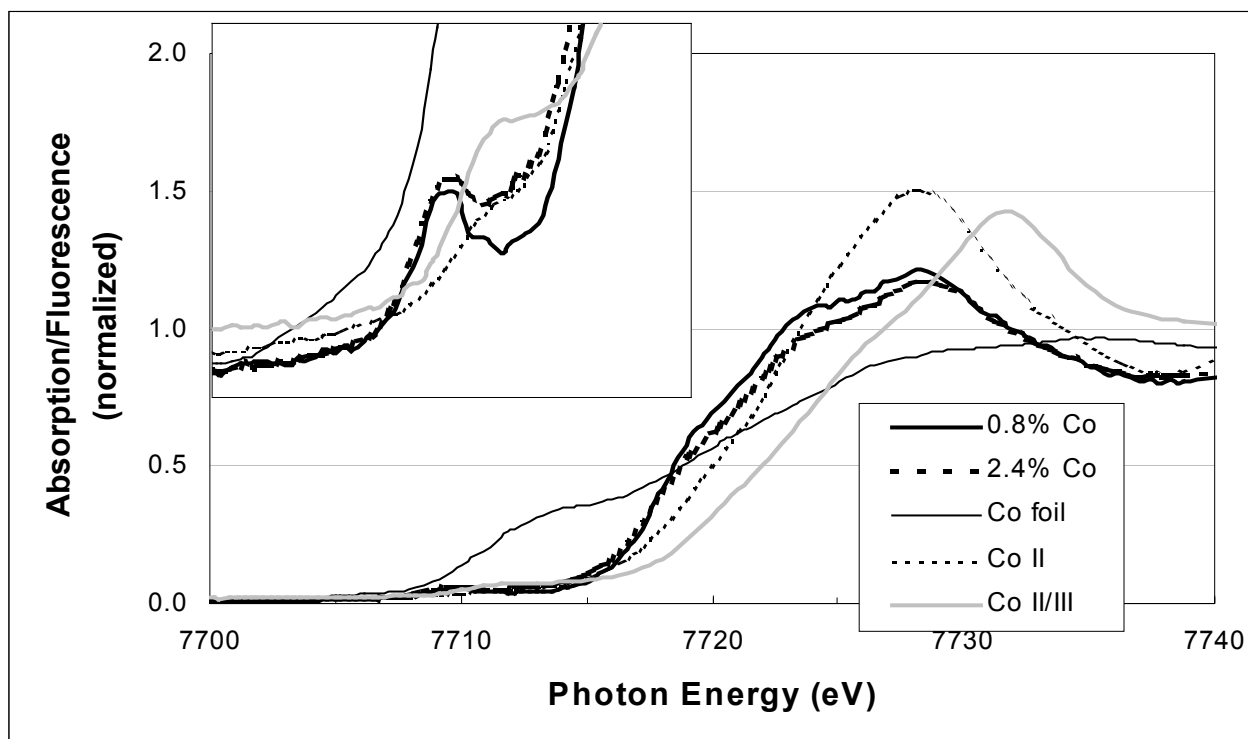


Figure 4.6. XANES spectra at Co K-edge for cobalt containing $\text{CeO}_2/\text{Al}_2\text{O}_3$ catalysts and standards. The inset shows the pre-edge features from 7700 – 7720 eV with an absorbance scale extending to 0.1.

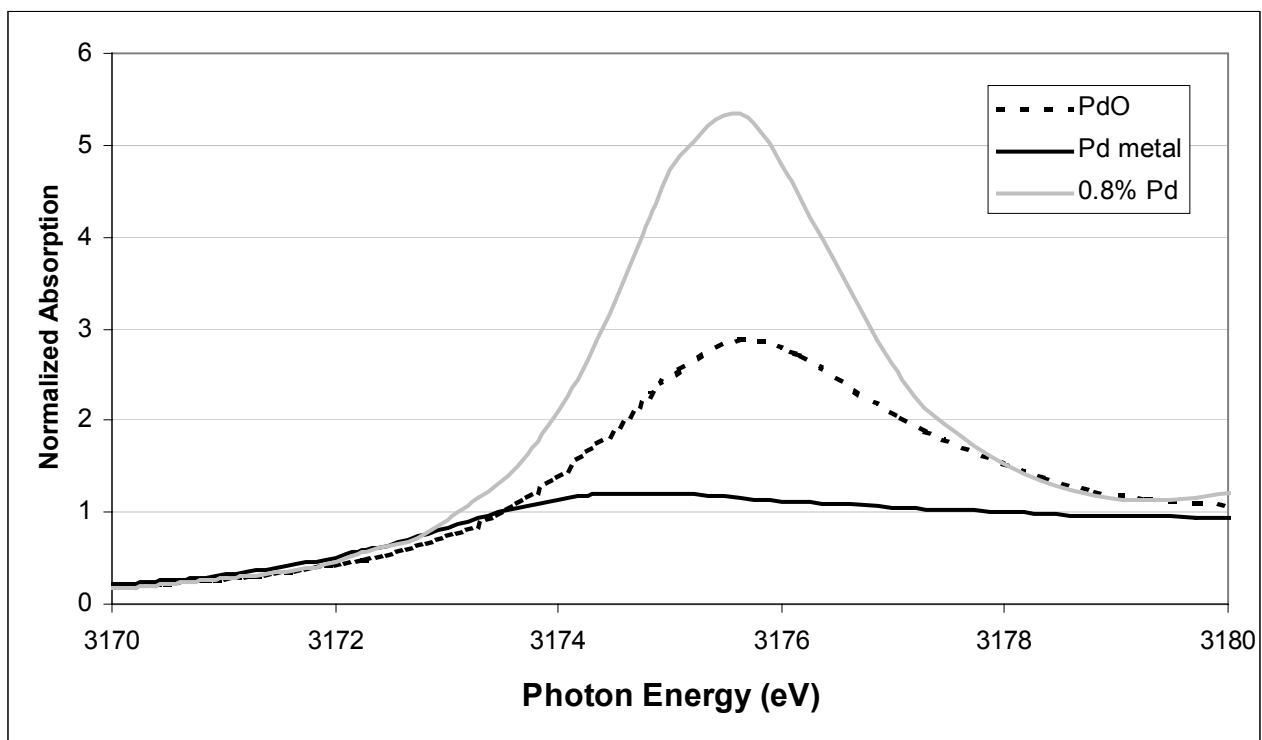


Figure 4.7. Pd L_{III} XANES of Pd/ $\text{CeO}_2/\text{Al}_2\text{O}_3$ catalyst and Pd standards, ambient conditions (PdO spectrum courtesy of H. Modrow, Bonn University, Germany).

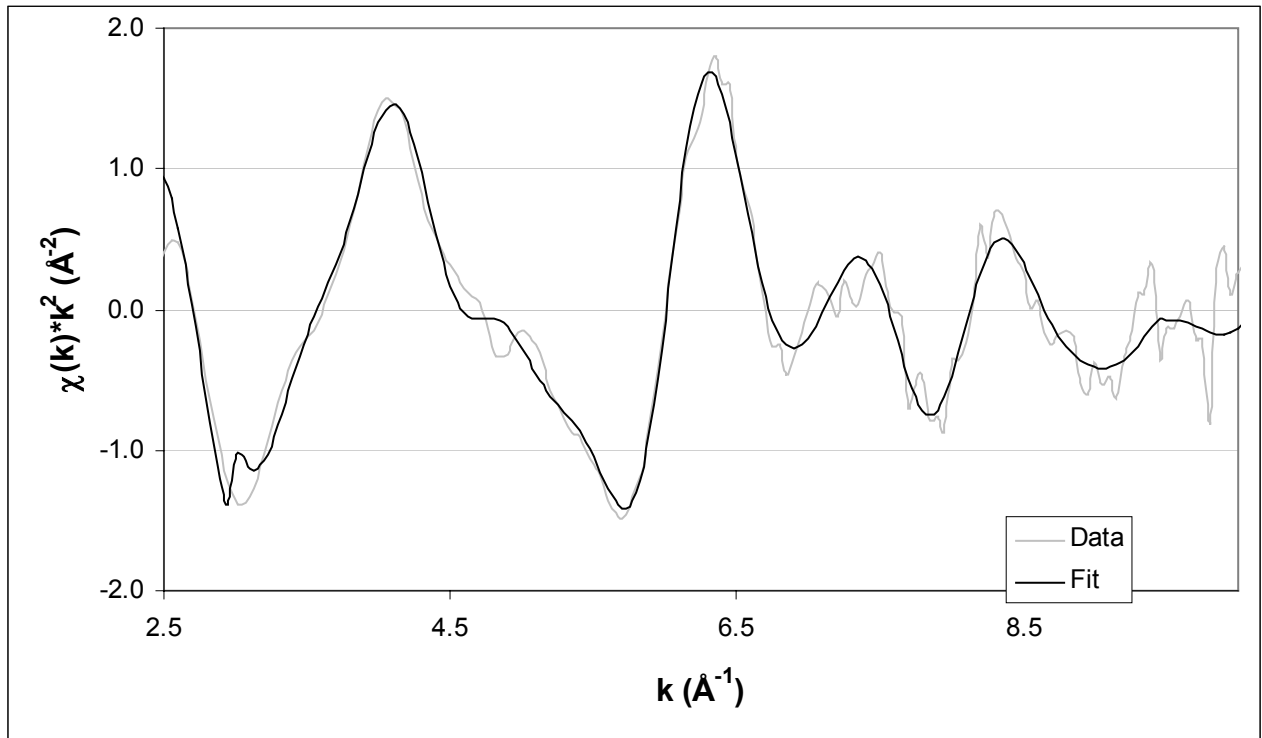
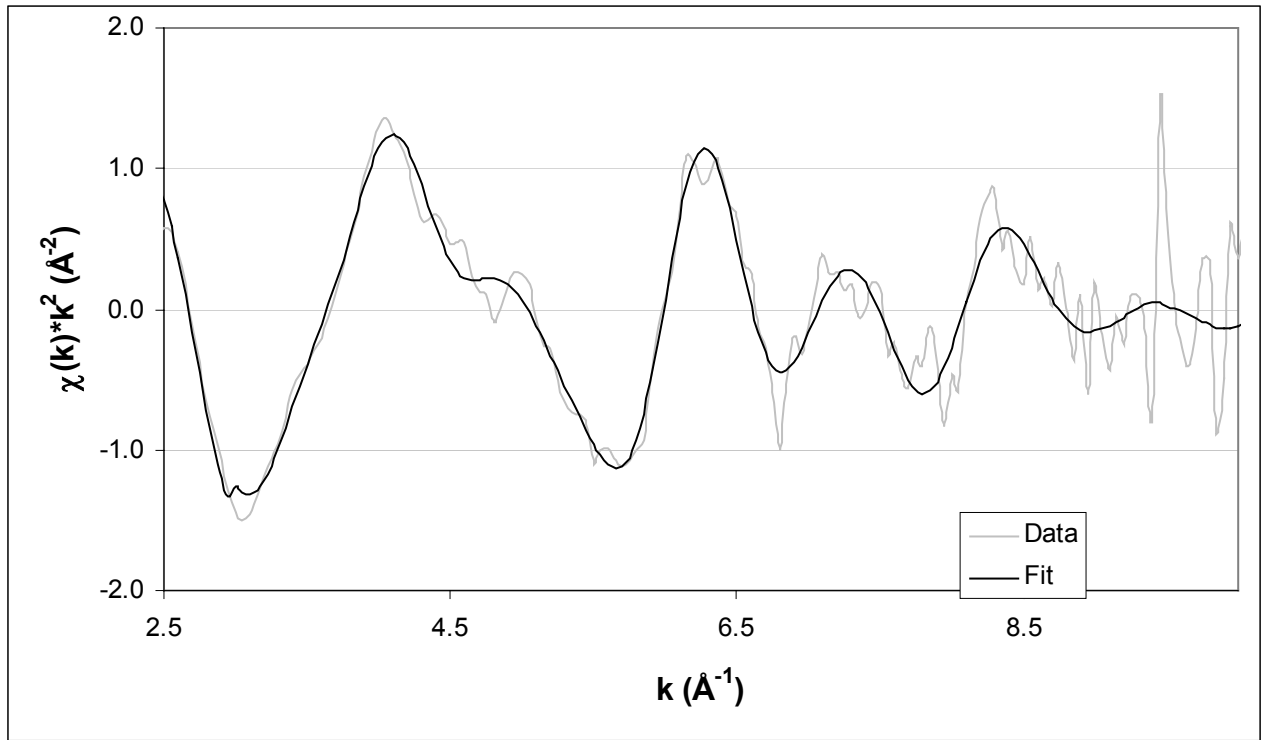


Figure 4.8. EXAFS for Co K of 0.8% Co (top) and 2.4% Co (bottom) doped CeO₂/Al₂O₃. The fit obtained using Artemis (Ravel and Newville 2004) is shown.

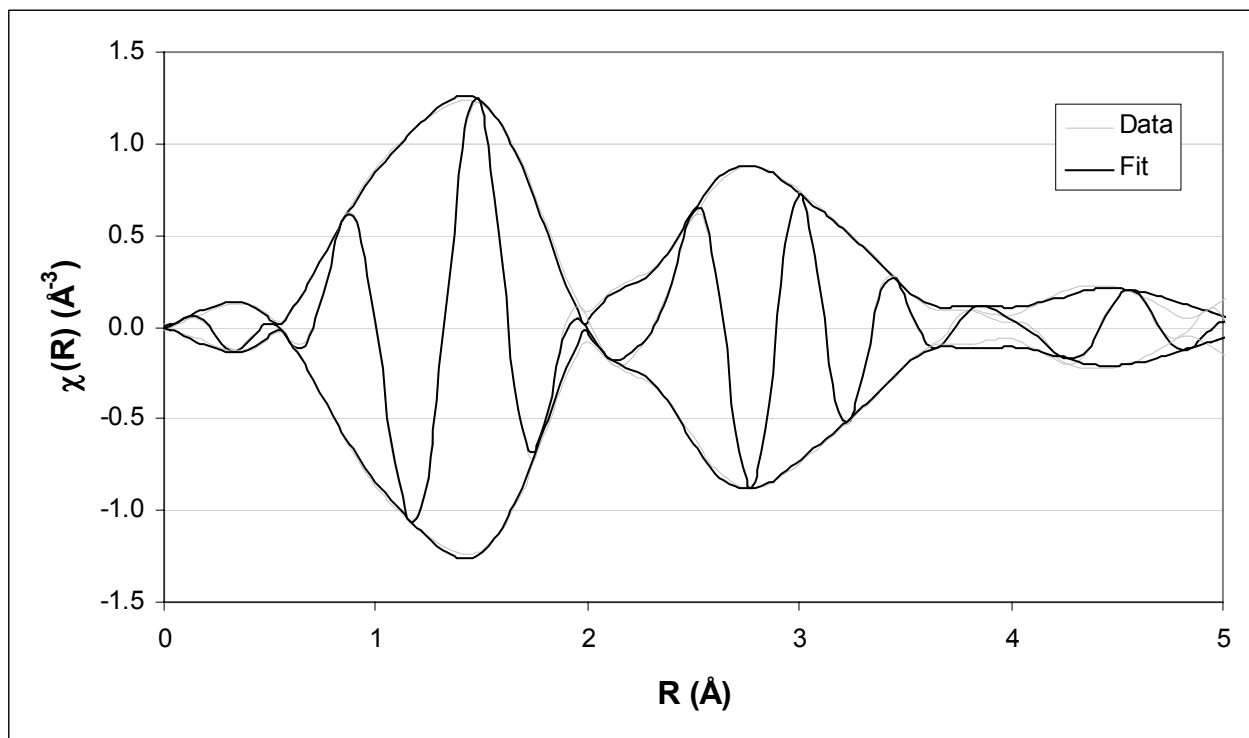
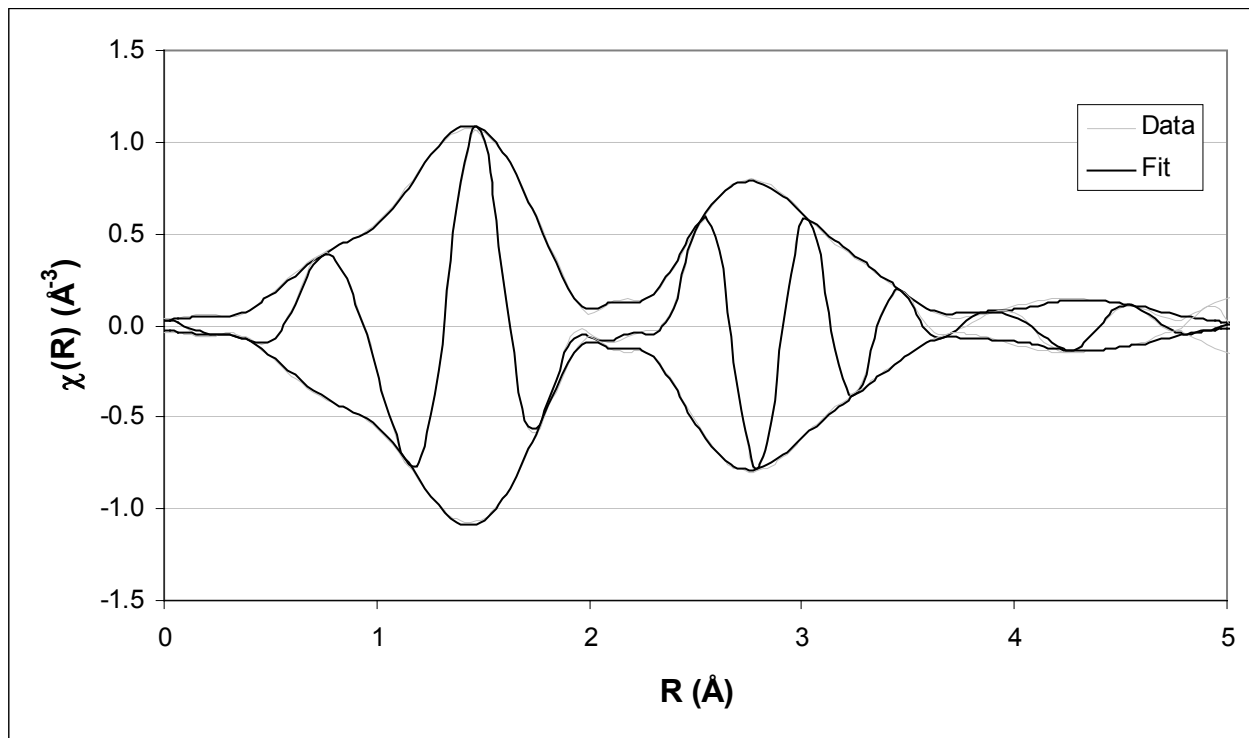


Figure 4.9. Fourier transformed (k^2 weighted magnitude and real parts) EXAFS for Co K of 0.8% Co (top) and 2.4% Co (bottom) doped $\text{CeO}_2/\text{Al}_2\text{O}_3$. The fit obtained using Artemis (Ravel and Newville 2004) is shown

Table 4.2. Fitted EXAFS parameters for 0.8% Co catalyst using Artemis (top) and WinXAS (bottom).

Shell	CN	R (Å)	σ (Å)
O (1)	4.4 ± 1.9	1.95 ± 0.04	0.009 ± 0.008
Co (2)	5.2 ± 3.3 ²	3.07 ± 0.05	0.014 ± 0.003 ³
Ce (2)	6.8 ± 3.3 ²	3.20 ± 0.07	0.014 ± 0.003 ³
O (3)	21 ¹	3.88 ± 0.13	0.031 ± 0.026
Ce (4)	6 ¹	4.70 ± 0.21	0.020 ± 0.030
O (5)	24 ¹	5.41 ± 0.57	0.050 ± 0.140

O (1)	4.5 ± 0.04	1.93 ± 0.01	0.0078 ± 0.0001
Co (2)	4.8 ²	3.05 ± 0.01	0.0153 ± 0.0001 ³
Ce (2)	7.2 ²	3.17 ± 0.01	0.0153 ± 0.0001 ³
O (3)	21 ¹	3.86 ± 0.01	0.0207 ± 0.0003
Ce (4)	6 ¹	4.63 ± 0.01	0.0189 ± 0.0005
O (5)	24 ¹	5.23 ± 0.01	0.0355 ± 0.001

¹ Value fixed during fitting

² Sum of Co (2) and Ce (2) constrained to 12 during fitting

³ Set equal during fitting

Table 4.3. Fitted EXAFS parameters for 2.4% Co catalyst using Artemis (top) and WinXAS (bottom).

Shell	CN	R (Å)	σ (Å)
O (1)	4.4 ± 2.4	1.95 ± 0.05	0.006 ± 0.009
Co (2)	7.2 ± 4.4^2	3.03 ± 0.08	0.012 ± 0.005^3
Ce (2)	4.8 ± 4.4^2	3.19 ± 0.09	0.012 ± 0.005^3
O (3)	21^1	3.85 ± 0.16	0.028 ± 0.031
Ce (4)	6^1	4.72 ± 0.21	0.013 ± 0.027
O (5)	24^1	5.45 ± 0.47	0.029 ± 0.082

O (1)	4.7 ± 0.005	1.92 ± 0.01	0.0056 ± 0.0001
Co (2)	4.1^2	3.01 ± 0.01	0.014 ± 0.0002^3
Ce (2)	7.9^2	3.17 ± 0.01	0.014 ± 0.0002^3
O (3)	21^1	3.84 ± 0.01	0.0160 ± 0.0001
Ce (4)	6^1	4.66 ± 0.01	0.0164 ± 0.0001
O (5)	24^1	5.30 ± 0.01	0.0317 ± 0.0001

¹ Value fixed during fitting

² Sum of Co (2) and Ce (2) constrained to 12 during fitting

³ Set equal during fitting

CHAPTER 5

DISCUSSION AND CONCLUSIONS

5.1 Reactor Experiments and Acid Site Characterization

The fixed bed reactor experiments show that $\text{La}_2\text{O}_3/\text{Al}_2\text{O}_3$, $\gamma\text{-Al}_2\text{O}_3$, WO_3/ZrO_2 , and HZSM-5 are active and selective for DMS. WO_3/ZrO_2 was the most active of these at 340°C , although it was not suitable for DMS production at higher temperatures due to a significant conversion of methanol to methane. At 360°C on this catalyst, 1.6-2.0% of the methanol was converted to methane compared to less than 1% at 340°C . At 400°C , the activities of the other three catalysts decreased in the order $\text{La}_2\text{O}_3/\text{Al}_2\text{O}_3 > \gamma\text{-Al}_2\text{O}_3 > \text{HZSM-5}$ and the yield to hydrocarbons was less than 1%. Conditions could be found for all of these catalysts, except for HZSM-5 (340°C for WO_3/ZrO_2 , 400°C for the other two), at which more than 90% of the methanol was converted to sulfur products at a WHSV greater than 0.35 h^{-1} . At these conditions, the selectivity to MT was less than 10% for molar feed ratios of methanol to H_2S greater than 1.8. On HZSM-5, greater than 75% sulfur product yield was achieved along with an MT selectivity less than 5% at conditions similar to those of the other catalysts.

On all of these catalysts, it was observed that MT yield decreased slightly or remained constant with increased contact time, while the DMS yield increased. The yields of both sulfur products were close to the equilibrium values calculated at a given total sulfur product yield (see section 3.1 for calculation details). These observations are not consistent with a purely serial mechanism ($\text{H}_2\text{S} \rightarrow \text{MT} \rightarrow \text{DMS}$), but instead suggest that MT disproportionation is fast and close to equilibrium. Since the disproportionation reaction is fast, MT in the product stream can be separated and recycled to the feed to be converted to DMS. It was also observed that MT selectivity decreases with increased feed ratio.

For all four of these catalysts, the DME yield decreased with contact time, with DME decomposing predominantly to sulfur products. It was observed that for $\text{La}_2\text{O}_3/\text{Al}_2\text{O}_3$ and $\gamma\text{-Al}_2\text{O}_3$, DME and methanol are close to their equilibrium concentrations at a given yield of sulfur products. For WO_3/ZrO_2 , the DME yield is slightly greater than the calculated equilibrium value (see section 3.1 for details of this calculation); for HZSM-5, it is slightly less. This indicates that the reaction forming DME from methanol is also fast and close to equilibrium. Thus, DME in the product stream can also be separated and recycled to the feed to be converted to DMS.

Characterization of the acid sites on these catalysts by thermal desorption of 1-propanamine indicates that sites desorbing in the range of 300-350°C are responsible for most of the activity to sulfur products. The number of sites in this range for these catalysts decreases in the same order as the activity ($\text{WO}_3/\text{ZrO}_2 > \text{La}_2\text{O}_3/\text{Al}_2\text{O}_3 > \gamma\text{-Al}_2\text{O}_3 > \text{HZSM-5}$). HZSM-5 was the only catalyst of this group to retain the reaction products of 1-propanamine above 400°C.

Fixed bed reactor experiments showed $\text{WO}_3/\text{Al}_2\text{O}_3$ to be active and selective to MT, with DMS selectivity less than 15%. Conversions of methanol to sulfur products greater than 90% could be achieved only at a low WHSV of 0.14 h^{-1} , so $\text{WO}_3/\text{Al}_2\text{O}_3$ is less active than the four catalysts in the first group. Yields to MT and DMS are far from their calculated equilibrium values, indicating that the disproportionation reaction is slower on this catalyst. The DME yield is slightly below its calculated equilibrium value at a given sulfur product yield and decreases with contact time, indicating the reaction forming DME from methanol is fast and close to equilibrium. Therefore, DME can be recycled, and it may also be possible to recycle DMS for conversion back to MT via the disproportionation reaction.

For all of the catalysts discussed above, the selectivity to sulfur products does not decrease as the partial pressure of methanol decreases by orders of magnitude. This indicates

that the rate of methanol-H₂S condensation is close to zero order in methanol. Also, the Weisz-Prater analysis shows that mass transport of reactants in the catalyst pores does not limit the overall rate.

The other catalysts that were studied (Mo₃/SiO₂, TiO₂/SiO₂, SAPO-18, and AlPO-18) were found to be unsuitable for either MT or DMS production. Mo₃/SiO₂ had low selectivity to sulfur products and produced a large amount of carbonyl sulfide. SAPO-18 and AlPO-18 had low activity and TiO₂/SiO₂ had almost no activity. For these catalysts and WO₃/Al₂O₃, it was also found that acid sites desorbing reaction products of 1-propanamine in the range 300-350°C were probably responsible for the formation of most sulfur products.

5.2 Reaction Mechanisms

Based on experimental results in this and previous work, along with the catalytic chemistry associated with metal oxides, a possible mechanism emerged that explained the activity of the catalyst in sulfidation of methanol and the distribution of products. By examining experimental results for this reaction from the relevant literature, it can be seen that the activity is highest for catalysts with LCs of moderate strength [Q_{CO} of 30-40 kJ/mol (Mashkina et al., 1988)]. Alumina falls in this range and the activity sharply decreases when the cation is replaced with a neighboring element on the periodic table (Mg and Si). It is also apparent that strongly basic and acidic catalysts are selective to MT while more amphoteric catalysts favor DMS.

In order to examine the mechanism that leads to these trends, details about the coverage of the catalyst surface must first be considered. If it is assumed that dissociative adsorption of methanol and H₂S is not rate limiting, then the surface should be in equilibrium with these two components and H₂O in the gas phase. It is expected that methanol and water have roughly the same adsorption energy on an LC/BC pair since the O-H bonds that are broken in the adsorption

of both molecules have similar acidity. As discussed below, H₂O has a higher adsorption energy on alumina than does H₂S. At low conversion, methanol should be the most abundant surface species, and at high conversion, water.

Ab-initio calculations (see section 1.5 for details) were performed in this work using Gaussian 03 (Frisch et al., 2004) to determine the difference in binding energies of hydroxyl and bisulfide species with an LC. Clusters consisted of a cation (Na⁺, Mg²⁺, Al³⁺, and Si⁴⁺) coordinated to O²⁻ and OH⁻ ligands to balance the charge. Clusters were optimized using the B3LYP density functional and the 6-31G basis set and energies were calculated using the 6-311G(d) basis set. The same calculation was performed on a cluster with one OH⁻ ligand replaced by an SH⁻ ligand. It was found that on Al³⁺ and Si⁴⁺, H₂O was bound more strongly than H₂S by about 30 kJ/mol. On Na⁺ and Mg²⁺, H₂S was bound more strongly by 23 and 8 kJ/mol respectively. It therefore seems that on alumina, H₂S coverage should be significantly below a monolayer, and this coverage should increase with the basicity of the catalyst.

One important consequence of surface acidity/basicity is the effect it has on surface bond strengths. On acidic catalysts, the valence band energy is low and the negatively charged species (oxygen and sulfur) are more strongly bound to the lattice than they are to the positively charged surface species (protons and methyl groups). As the surface becomes basic, this trend reverses; the binding of oxygen and sulfur with the lattice weakens and their binding to protons and methyl groups strengthens. Due to these effects, the reactivity of surface protons and methyl groups increases with acidity and decreases with basicity; the reactivity of adsorbed sulfur and oxygen follows the opposite trend.

Ab-initio calculations using Gaussian 03 (Frisch et al., 2004) were performed in this work on H₂S, H₂O, MT, MeOH, DMS, and DME to determine heterolytic bond dissociation

energies. Structure optimization and energy calculations of the molecules and ions were done using the B3LYP density functional and the 6-311+G(d) basis set. It was found that the bond energy decreased in the order O-H (1610-1640 kJ/mol) > S-H (1470-1500 kJ/mol) > C-O (1160-1180 kJ/mol) > C-S (1040-1070 kJ/mol).

In the mechanism that is proposed below, it is assumed that the transfer of a methyl group between two surface atoms is slower than the analogous transfer of a proton. Therefore, methyl transfer is the rate determining step of each pathway. The activation barrier for this process is affected by both the binding energy of the methyl group to the surface and the binding energy of the electron donor atom (oxygen or sulfur) to the surface. Since methyl groups are bound more weakly on acidic surfaces and sulfur and oxygen atoms are bound more weakly on basic surfaces, it is expected that the activation barrier is lowest somewhere in the middle of the acidity scale (measured, for instance, by LC Q_{CO} or by the desorption temperature of the Hoffmann elimination products of 1-propanamine). At higher acid strengths, the increase in oxygen and sulfur binding energy increases the barrier height. At lesser acid strengths, the increased binding energy of the methyl groups increases the barrier height. This finding is confirmed experimentally in that more acidic oxide catalysts (PO_4^{3-}/SiO_2) and more basic oxide catalysts (MgO) are almost inactive in the sulfidation of methanol (Ziolek et al., 1993). This is also reflected in the finding that chemisorbed methanol is least stable on catalysts that are neither strongly basic nor acidic such as alumina and La_2O_3/Al_2O_3 . An illustration of these effects is shown in Figure 5.1. In addition to this effect, the amount of sulfur adsorbed onto a surface generally decreases with acid strength, as suggested by the ab-initio calculations.

The reaction mechanism on alumina begins with the dissociative adsorption of methanol and H_2S onto LC/BC pairs as discussed in Chapter 1. The resulting bisulfide (LC-SH) and

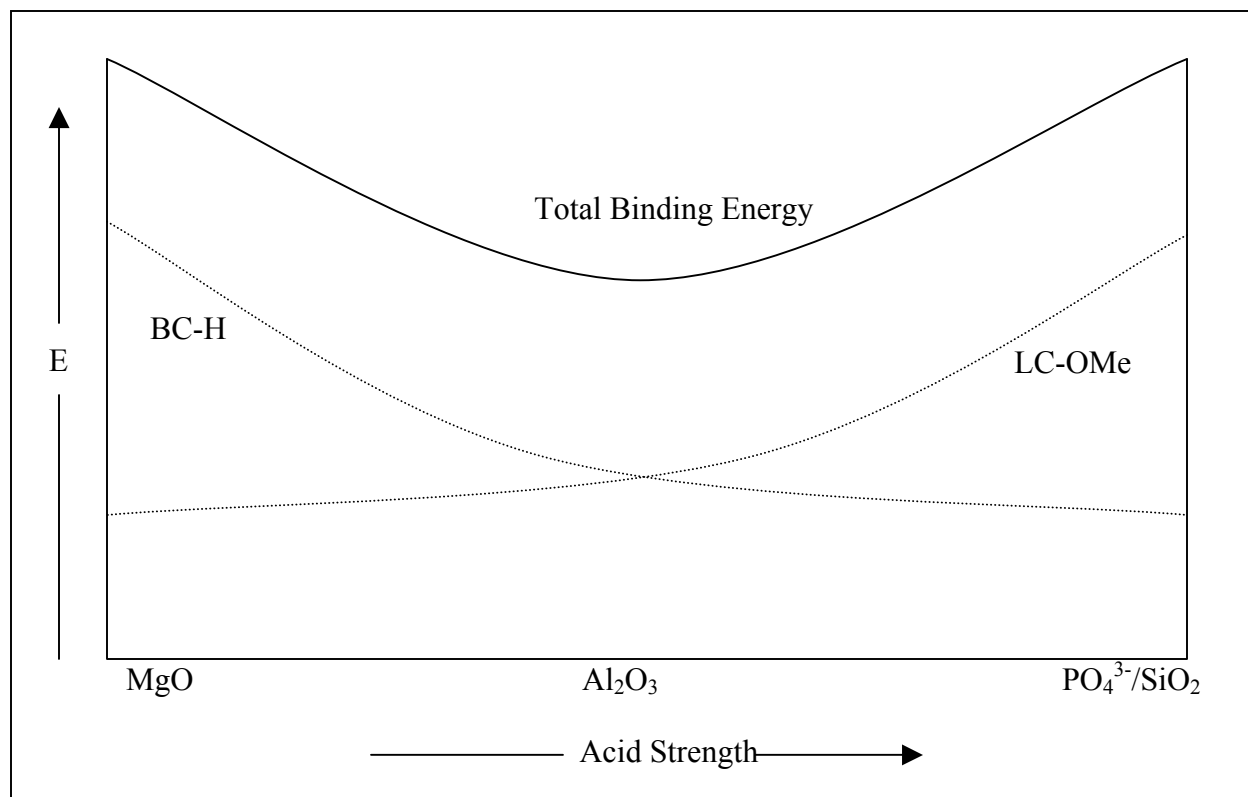


Figure 5.1. Illustration of the effect of surface acidity on the adsorption energy of methanol on LC/BC active sites. Solid line indicates the total adsorption energy. Dashed lines indicate the contribution to the adsorption energy from the LC–OMe and BC–H bonds.

methyl (BC-Me) groups can then react according to several different pathways that are shown in Figure 5.2. If a methyl species is adjacent to the bisulfide, the two species can combine and desorb as MT (1), leaving an LC/BC pair on the surface. Alternatively, the bisulfide hydrogen can desorb by combining with a neighboring hydroxyl or methoxy group to form water, resulting in a sulfide (LC-S) and LC on the surface. The sulfide is expected to be more reactive than the bisulfide and a neighboring methyl group can transfer to it to form a mercaptide species (2). The mercaptide (LC-S-Me) can then be protonated by a neighboring hydroxyl and desorb as MT (2b). Both of these paths should be first order in H_2S and irreversible. Because the surface coverage by methanol is expected to be close to a monolayer at low conversion, the kinetics of these pathways should be less than first order in methanol, as observed.

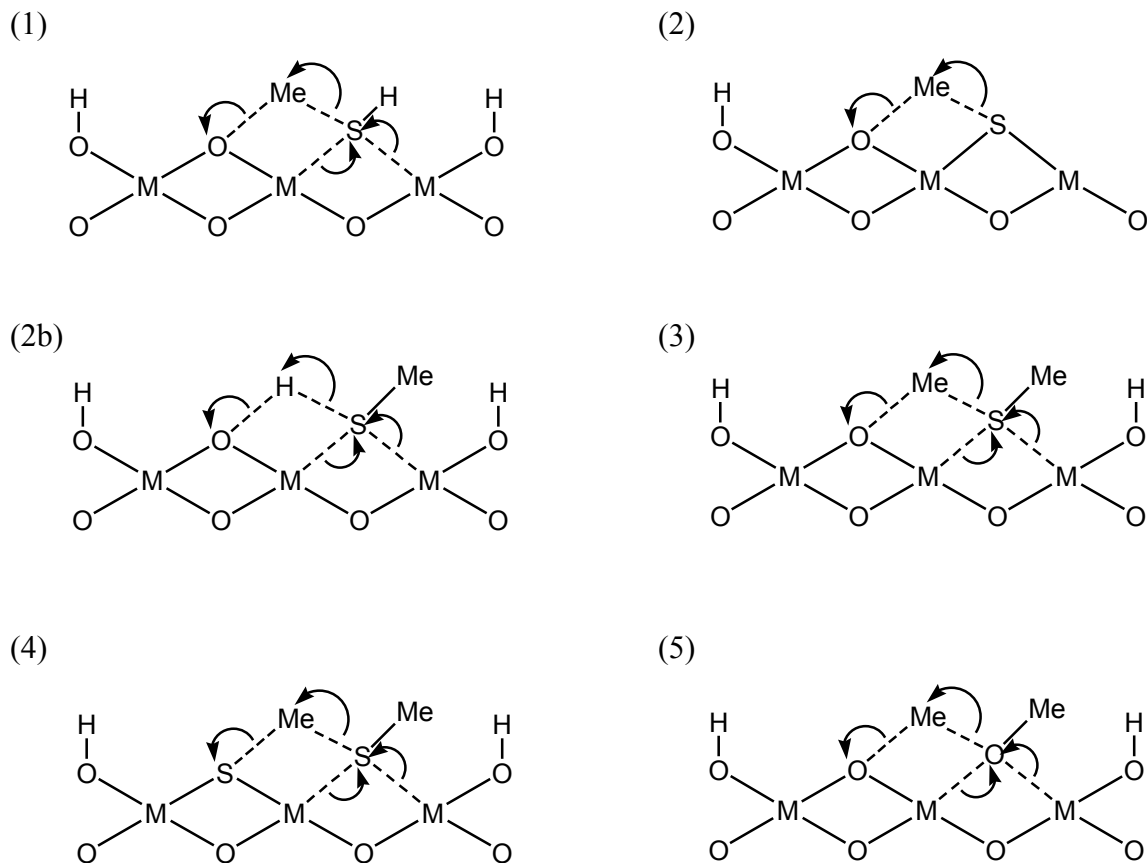


Figure 5.2. Steps of the proposed mechanism. M is a metal cation acting as a Lewis acid site.

Once formed, MT will dissociatively adsorb onto LC/BC pairs in a way similar to H_2S and will react with other surface species. The adsorbed mercaptide species can react with a neighboring methyl species and desorb as DMS (3). This reaction is expected to be first order in MT and irreversible. The disproportionation reaction will also occur to produce DMS and H_2S from MT. This reaction can occur when a methyl group is transferred from one surface mercaptide to another to desorb DMS (4), leaving a sulfide and LC on the surface. This reaction is similar to (3), but should have a lower activation barrier because the methyl group that is transferred is more weakly bound to sulfur than it is to oxygen. This path is reversible and expected to be second order in MT. A diagram of paths 1-4 is shown in Figure 5.3. In a

mechanism similar to (4), a methyl group can transfer between two neighboring methoxy groups to desorb DME (5), this path being fast and reversible.

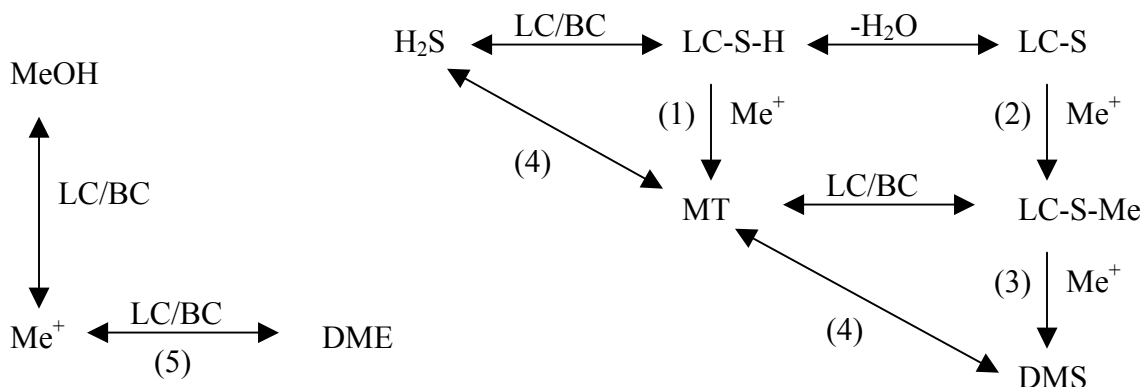


Figure 5.3. Diagram showing the relations between paths 1-5 in the overall mechanism.

Insight into the effects of surface acidity on the proposed mechanistic pathways can be gained by taking into account the trends in activity and selectivity in the experimental data. As mentioned earlier, the rate determining step of each path will have a minimum activation barrier at a certain level of surface acid strength. On alumina-based catalysts, the activity increases with acid strength (being highest for HF/Al₂O₃), but is lower for more acidic catalysts such as alumino-silica and PO₄³⁻/SiO₂ (Mashkina et al., 1988). The selectivity of DMS (vs. MT) is found to be highest on alumino-silica (91% selectivity), being lower for less acidic catalysts such as alumina. The activation barrier heights of paths leading to both DMS and MT appear to be lowest at acid strengths close to alumina, however, the minimum barrier height of path 3 occurs at higher acid strength, as illustrated in Figure 5.4. This would indicate that transferring the second methyl group to a sulfur atom to form DMS is more difficult than transferring the first methyl group to form MT, and requires stronger acid sites.

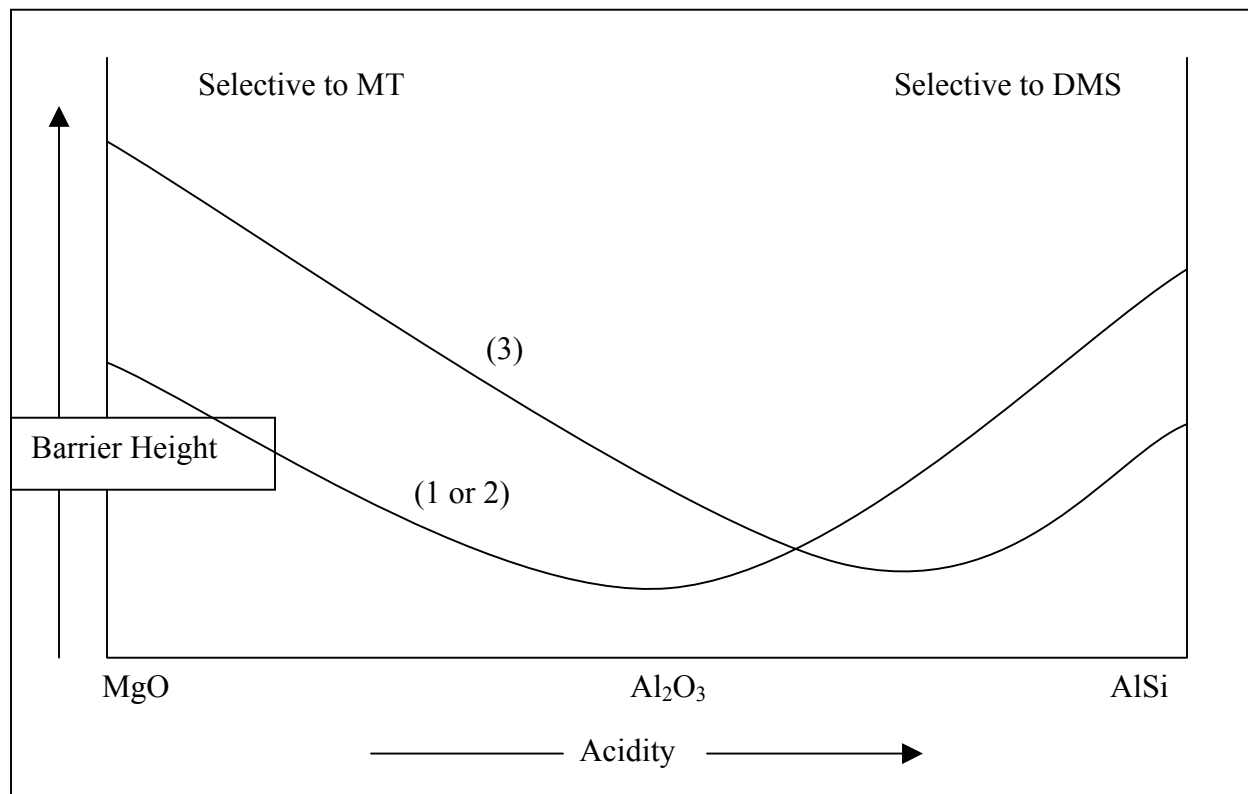


Figure 5.4. Illustration of the effect of surface acidity on the activation barrier heights of paths leading to MT (1 or 2) and DMS (3).

The following is a brief summary of the conclusions drawn in this section:

- WO_3/ZrO_2 , $\text{La}_2\text{O}_3/\text{Al}_2\text{O}_3$, $\text{g-Al}_2\text{O}_3$, and HZSM-5 are suitable catalysts for the production of DMS from methanol and H_2S while $\text{WO}_3/\text{Al}_2\text{O}_3$ is suitable for the production of MT.
- The reaction that produces DME from methanol is fast and close to equilibrium on most catalysts. Most of the methanol is converted to DME at short contact times, and at longer contact times the DME converts to sulfur products.
- For good DMS catalysts, the DMS yield increases with conversion while the MT yield remains relatively constant. This is not consistent with a purely serial mechanism and

indicates that the disproportionation reaction is fast and close to equilibrium on these catalysts.

- The selectivity to sulfur products does not decrease significantly as the methanol partial pressure decreases, indicating that the reaction is close to zero order in methanol.
- The selectivity to MT decreases with increasing feed ratio, temperature, and contact time.
- Acid sites desorbing n-propanamine between 300-350°C are the most active sites for the sulfidation reactions.
- The transfer of the second methyl group to an adsorbed sulfur atom to form DMS is more difficult than transferring the first methyl group to form MT, and requires stronger acid sites.

Recommendations for further work would be to better characterize the catalyst surfaces by determining the strength of Lewis acid sites using CO adsorption in conjunction with IR spectroscopy. It may also be useful to conduct adsorption studies on the catalysts to determine the coverage of the surface by methyl, bisulfide, sulfide, and mercaptide species under reaction conditions. This could be done by heating the catalyst in an atmosphere with a composition similar to that in the reactor long enough for the surface to come to equilibrium with the gas phase. Then IR spectra would be taken to quantify the different adsorbed species.

5.3 XAS Investigation of Metal-Doped CeO₂/Al₂O₃ Catalysts

XANES spectra of the Ce LIII edge show that the number of oxygen vacancies in a catalyst increases with temperature and is less affected by whether the atmosphere is reducing or inert. It was found that doping the CeO₂/Al₂O₃ catalyst with 0.8% Co doubled the number of oxygen vacancies present in the undoped catalysts. Doping with 2.4% Co slightly decreased the number of oxygen vacancies and doping with 0.8% Pd slightly increased this number. There does not appear to be a general correlation between the number of oxygen vacancies and activity

in the difficult isobutyric acid condensation reaction (Bhat, 2004), although in general a large number of vacancies means a more active catalyst.

Based on evidence from the Co K-edge XANES and EXAFS spectra, it appears that in both Co doped catalysts, most of the cobalt atoms are substituted for cerium atoms in the CeO₂ lattice. The cobalt atom is coordinated by four oxygen atoms in tetrahedral positions that split the energies of the Co 4p orbitals to produce the observed XANES spectra. The EXAFS fits did not show cobalt to be present in a separate CoO or metallic phase, and this is supported by H₂ chemisorption data (Bhat, 2004). The EXAFS fits did show that up to half of the cerium atoms in the second coordination shell are substituted by cobalt, indicating that cobalt is not homogeneously dispersed in the CeO₂ lattice. Palladium L_{III} XANES showed that a large portion of the Pd is dissolved in the CeO₂ lattice in a highly ionic state.

The following is a brief summary of the conclusions drawn in this section:

- No general correlation was found between the number of oxygen vacancies and the activity of a catalyst for ketonization.
- In cobalt doped catalysts, the cobalt atom is substituted for a cerium atom in the CeO₂ lattice. The cobalt atom has tetrahedral oxygen coordination.
- In palladium doped catalysts, some palladium is dissolved in the CeO₂ lattice in a highly ionic state.

A recommendation for further work would be to perform theoretical calculations to predict the XANES spectra of cobalt and palladium atoms in the proposed structures to determine if this fits experimental XANES spectra.

REFERENCES

- A.K. Bhat, Metal-Doped Rare Earth Oxide Catalysts for Condensations to Ketones, MS Thesis, Louisiana State University, Baton Rouge, LA, 2004.
- A. Bianconi, A. Marcelli, H. Dexpert, R. Karnatak, A. Kotani, T. Jo, *Phys. Rev. B* 1987, 35(2), 806-12.
- M. Boudart, *Ind. Eng. Chem. Fundam.* 1986, 25, 70-5.
- J. Chen, P.A. Wright, J.M. Thomas, S. Natarajan, L. Marchese, S.M. Bradley, G. Sankar, C.R.A. Catlow, P.L. Gai-Boyes, R.P. Townsend, C.M. Lok, *J. Phys. Chem.* 1994, 98, 10216-24.
- C.J. Cramer, *Essentials of Computational Chemistry – Theories and Models*, Wiley, Chichester, 2002, 95-120, 153-89, 233-73.
- K.M. Dooley, G.L. Price, V.I. Kanazirev, V.I. Hart, *Catal. Today* 1996, 31, 305-15.
- J.E. El Fallah, S. Boujana, H. Dexpert, A. Kiennemann, J. Majerus, O. Touret, F. Villain, F. Le Normand, *J. Phys. Chem.* 1994, 98, 5522-33.
- M. Fernandez-Garcia, *Catal. Rev.* 2002, 44(1), 59-121.
- J.B. Foresman, A. Frisch, *Exploring Chemistry with Electronic Structure Methods*, Gaussian, Inc., Pittsburgh, 1996, 97-139.
- M.J. Frisch, G.W. Trucks, H.B. Schlegel, G.E. Scuseria, M.A. Robb, J.R. Cheeseman, J.A. Montgomery Jr., T. Vreven, K.N. Kudin, J.C. Burant, J.M. Millam, S.S. Iyengar, J. Tomasi, V. Barone, B. Mennucci, M. Cossi, G. Scalmani, N. Rega, G.A. Petersson, H. Nakatsuji, M. Hada, M. Ehara, K. Toyota, R. Fukuda, J. Hasegawa, M. Ishida, T. Nakajima, Y. Honda, O. Kitao, H. Nakai, M. Klene, X. Li, J.E. Knox, H.P. Hratchian, J.B. Cross, V. Bakken, C. Adamo, J. Jaramillo, R. Gomperts, R.E. Stratmann, O. Yazyev, A.J. Austin, R. Cammi, C. Pomelli, J.W. Ochterski, P.Y. Ayala, K. Morokuma, G.A. Voth, P. Salvador, J.J. Dannenberg, V.G. Zakrzewski, S. Dapprich, A.D. Daniels, M.C. Strain, O. Farkas, D.K. Malick, A.D. Rabuck, K. Raghavachari, J.B. Foresman, J.V. Ortiz, Q. Cui, A.G. Baboul, S. Clifford, J. Cioslowski, B.B. Stefanov, G. Liu, A. Liashenko, P. Piskorz, I. Komaromi, R.L. Martin, D.J. Fox, T. Keith, M.A. Al-Laham, C.Y. Peng, A. Nanayakkara, M. Challacombe, P.M.W. Gill, B. Johnson, W. Chen, M.W. Wong, C. Gonzalez, and J.A. Pople, Gaussian, Inc., Wallingford CT, 2004. Gaussian 03, Revision C.02.
- B.C. Gates, *Catalytic Chemistry*, Wiley, New York, 1992, 269-72, 320-6, 371-3.
- T.S. Hendren, K.M. Dooley, *Catal. Today* 2003, 85(2-4), 333-51.

- V.E. Henrich, P.A. Cox, *The Surface Science of Metal Oxides*, Cambridge University Press, Cambridge, 1994, 284-5.
- G.P. Huffman, N. Shah, J. Zhao, F.E. Huggins, T.E. Hoost, S. Halvorsen, J.G. Goodwin Jr., *J. Catal.* 1995, 151, 17-25.
- Hyprotech Ltd., HYSYS.PlantNetVers v2.2.2 2000.
- V. Kanazirev, K.M. Dooley, G.L. Price, *J. Catal.* 1994, 146, 228-36.
- L.S. Kau, D.J. Spira-Solomon, J.E. Penner-Hahn, K.O. Hodgson, E.I. Solomon, *J. Am. Chem. Soc.* 1987, 109, 6433-42.
- L. Kubelkova, S. Beran, J.A. Lercher, *Zeolites* 1989, 9, 539-43.
- V.Y. Mashkin, V.M. Kudenkov, A.V. Mashkina, *Ind. Eng. Chem. Res.* 1995, 34, 2964-70.
- A.V. Mashkina, E.A. Paukshtis, V.N. Yakovleva, *React. Kinet. Catal. Lett.* 1988, 29(3), 514-20.
- A.V. Mashkina, V.N. Yakovleva, *React. Kinet. Catal. Lett.* 1991, 32(3), 636-41.
- A.V. Mashkina, V.N. Yakovleva, L.N. Khairulina, *React. Kinet. Catal. Lett.* 1991, 43(2), 405-11.
- V.M. Mastikhin, I.L. Mudrakovsky, A.V. Nosov, A.V. Mashkina, *J. Chem. Soc., Faraday Trans. 1* 1989, 85(9), 2819-25.
- P. Nachimuthu, W.C. Shih, R.S. Liu, L.Y. Jang, J.M. Chen, *J. Solid State Chem.* 2000, 149, 408-13.
- A. Norman, V. Perrichon, A. Bensaddik, S. Lemaux, H. Bitter, D. Koningsberger, *Topics in Catal.* 2001, 16, 363-8.
- A.V. Nosov, V.M. Mastikhim, A.V. Mashkina, *J. Mol. Catal.* 1991, 66, 73-83.
- T.J. Paskach, G.L. Schrader, R.E. McCarley, *J. Catal.* 2002, 211, 285-95.
- R.H. Perry, D.W. Green, J.O. Maloney, *Perry's Chemical Engineers' Handbook*, McGraw Hill, Washington, D.C., 1997, 2-329.
- K.R. Priolkar, P. Bera, P.R. Sarode, M.S. Hegde, S. Emura, R. Kumashiro, N.P. Lalla, *Chem. Mater.* 2002, 14(5), 2120-8.
- J.A. Rabo, G.J. Gajda, *Catal. Rev. Sci. Eng.* 1989, 31(4), 385-430.

- S.D. Randery, J.S. Warren, K.M. Dooley, *Appl. Catal. A* 2002, 226, 265-80.
- B. Ravel, M. Newville, *J. Synchrotron Radiation* 2005, 12, 537-41.
- T. Ressler, *WinXAS* 2004.
- B. Skarman, D. Grandjean, R.E. Benfield, A. Hinz, A. Andersson, L.R. Wallenberg, *J. Catal.* 2002, 211, 119-33.
- A.V. Soldatov, T.S. Ivanshenko, S.D. Longa, A. Kotani, Y. Iwamoto, A. Bianconi, *Phys Rev. B* 1994, 50(8), 5074-80.
- Y. Takahashi, H. Sakami, M. Nomura, *Anal. Chim. Acta* 2002, 468, 345-54.
- S.I. Zabinski, J.J., Rehr, A. Ankudinov, R.C. Albers, M.J. Eller, *Phys. Rev. B* 1995, 52, 2995-3009.
- M. Ziolek, J. Czyzniewska, J. Kujawa, A. Travert, F. Mauge, J.C. Lavalley, *Microporous Mesoporous Mat.* 1998, 23, 45-54.
- M. Ziolek, J. Kujawa, O. Saur, J.C. Lavalley, *J. Phys. Chem.* 1993, 97, 9761-6.
- M. Ziolek, J. Kujawa, O. Saur, J.C. Lavalley, *J. Mol. Catal. A* 1995, 97, 49-55.
- M. Ziolek, I. Nowak, P. Decyk, J. Kujawa, *Stud. Surf. Sci. Catal.* 1998, 117, 509-16.

APPENDIX A

GAS CHROMATOGRAPHY DETAILS

Table A.1. GC settings for product analysis

Parameter	Setting
Injector Temperature	120°C
Detector Temperature	130°C
Sampling Valve Temperature	120°C
Initial Temperature	35°C
Final Temperature	125°C
Initial Time	3.0 min
Ramp Rate	50°C/min
Final Time	1.2 min
Volumetric Flow through Column	4.7 cc/min
Column Head Pressure	62 psig

Table A.2. Retention times for reactants and products

Compound	Retention Time (min)
Methane	0.75-0.79
Carbonyl Sulfide	0.78
Unidentified Compound (probably ethylene)	0.88-0.93
Dimethyl Ether	0.98-1.03
Methanol	1.08-1.13
Methanethiol	1.25-1.30
Dimethyl Sulfide	2.14-2.33

Table A.3. Response factors for reactants and products based on a 1.0 mL injection volume. Details of calculations are given in Appendix B.

Compound	Response Factor x 10 ⁶ (mol fraction/area)
Dimethyl Ether	5.81
Methanol	7.21
Methanethiol	7.09
Dimethyl Sulfide	3.56

APPENDIX B

MASS BALANCE CALCULATIONS FOR REACTOR EXPERIMENTS AND GC CALIBRATIONS

Determination of the response factors for methanol, DME, MT, and DMS was made by injecting samples from the product stream of the reactor, for which the composition was known. For all of the following calculations, it should be noted that none of the major reactions that take place on the catalysts change the total number of moles. Therefore, mole fractions can be used instead of molar flows in analysis of the data. To calibrate methanol, 0.49 mL/h liquid methanol and 97.3 cc/min 12% H₂S/N₂ (4.71 mol% methanol) were fed into the reactor at 150°C (under these conditions no reaction occurs). Ten samples of this stream were analyzed by the FID to ensure that fluctuations in the methanol flow rate averaged out. The response factor was calculated by the formula:

$$RF_{MeOH} = \frac{x_{MeOH}^0}{A_{MeOH}}$$

where RF_i is the FID response factor (mole fraction/area) for component i based on the sampling loop volume (1.0 mL), x_i^0 is the mole fraction of component i in the feed, and A_i is the FID area measured for component i . The values of this and other response factors are given in Appendix A.

The FID response factor for DMS was determined by feeding 0.49 mL/h liquid methanol and 14.1 mL/min 12% H₂S/N₂ (8.96 mol% H₂S) into the reactor loaded with La₂O₃/Al₂O₃ at 400°C. A sample of the product stream was analyzed by MS to verify

that all of the H₂S reacted. Ten samples of the product stream were analyzed by the FID and the response factor was calculated by

$$RF_{DMS} = \frac{x_{H_2S}^0 - x_{MT}}{A_{DMS}}$$

where x_i is the mole fraction of component i in the product stream and $x_{MT} = RF_{MT}A_{MT}$.

The FID response factor for MT was calibrated by feeding 0.49 mL/h liquid methanol and 97.3 cc/min 12% H₂S/N₂ (4.71 mol% methanol) to the reactor loaded with WO₃/Al₂O₃ at 400°C. No DME was detected in the product stream. Ten samples of the product stream were analyzed by the FID and the response factor was calculated by

$$RF_{MT} = \frac{x_{MeOH}^0 - x_{MeOH} - 2 \cdot x_{DMS}}{A_{MT}}$$

where $x_{DMS} = RF_{DMS}A_{DMS}$.

The FID response for DME was calibrated by feeding 0.49 mL/h liquid methanol and 39.7 cc/min N₂ (10.57 mol% methanol) into the reactor loaded with La₂O₃/Al₂O₃ at 400°C. In the FID response, the methanol and DME peaks are convoluted, so an accurate measurement of the individual peak areas is difficult. To avoid this problem, the combined peak area was measured and the two components are assumed to be at their equilibrium concentrations given by

$$K = \frac{x_{DME} \cdot x_{H_2O}}{x_{MeOH}^2} = \left[\frac{x_{DME}}{x_{MeOH}} \right]^2 = \left[\frac{A_{DME} \cdot RF_{DME}}{A_{MeOH} \cdot RF_{MeOH}} \right]^2$$

where K is equal to 4.93 (calculated by HYSYS Plant 2000), the equilibrium constant of the reaction $2 \text{ MeOH} \rightarrow \text{DME} + \text{H}_2\text{O}$ at 400°C. Ten samples of the product stream were analyzed by the FID and the response factor was calculated by the formula:

$$RF_{DME} = \frac{x_{MeOH}^0 - x_{MeOH}}{2 \cdot A_{DME}}$$

Since all of the above equations are coupled to each other by the response factors needed to calculate mole fractions from measured FID areas, they must be solved iteratively.

The equations used to compute methanol conversion (X_{MeOH}), sulfur product yield (Y_{SP}), MT selectivity (S_{MT}), and DME yield (Y_{DME}) are given by

$$X_{MeOH} = 1 - \frac{x_{MeOH}}{x_{MeOH}^0}$$

$$Y_{SP} = \frac{2 \cdot x_{DMS} + x_{MT}}{x_{MeOH}^0}$$

$$S_{MT} = \frac{x_{MT}}{2 \cdot x_{DMS} + x_{MT}}$$

$$Y_{DME} = \frac{2 \cdot x_{DME}}{x_{MeOH}^0}$$

where x_{MeOH}^0 is calculated from the composition of the product stream as

$$x_{MeOH}^0 = x_{MeOH} + 2 \cdot x_{DME} + x_{MT} + 2 \cdot x_{DMS}$$

The molar feed ratio (MeOH/H₂S) is computed from the mole fractions determined by FID analysis of the product stream since large fluctuations in the methanol flow rate make the value calculated based on the syringe pump set point inaccurate. The molar feed ratio (FR) is given by

$$FR = \frac{x_{MeOH}^0}{x_{H_2S}^0}$$

where $x_{H_2S}^0$ is the mole fraction of H₂S in the feed given from the product composition by

$$x_{H_2S}^0 = 0.12 \cdot (1 - x_{MeOH}^0)$$

The number 0.12 is the mole fraction of H₂S in the H₂S/N₂ feed. The conversion of H₂S (X_{H_2S}) can be computed by

$$X_{H_2S} = \frac{x_{MT} + x_{DMS}}{x_{H_2S}^0}$$

The weight hourly space velocity ($WHSV$) can be calculated from the feed ratio by

$$WHSV = \frac{FR \cdot F_{H_2S}^0 \cdot 32}{m_{cat}}$$

where $F_{H_2S}^0$ is the hourly molar feed of H₂S measured by the mass flow meter, m_{cat} is the weight of the dry catalyst in grams, and the number 32 is the molecular weight of methanol in grams/mole.

APPENDIX C

DATA FROM REACTOR EXPERIMENTS AND ACID CHARACTERIZATION

FIXED BED REACTOR RESULTS

Reactor Data

Gray boxes indicate catalyst regeneration in air at temperature given in section

Last three or four runs of each catalyst that are surrounded by a separate border are the runs examining deactivation

La₂O₃/Al₂O₃

Feed Ratio MeOH/H ₂ S	Temp °C	WHSV h ⁻¹	mol% in product (N ₂ free basis)				X, MeOH %	X, H ₂ S %	Y, SP %	S, MT %	Y, DME %	Y, HC %
			MeOH	DME	MT	DMS						
1.99 ± 0.33	340	0.416	5.4%	6.7%	12.9%	17.4%	91.8%	90.8%	71.7%	27.0%	20.0%	0.2%
1.46 ± 0.62	360	0.304	3.5%	2.3%	13.4%	18.9%	94.2%	79.5%	86.3%	26.1%	7.6%	0.2%
2.13 ± 0.24	380	0.420	3.3%	3.6%	4.1%	26.6%	95.2%	95.8%	84.2%	7.1%	10.6%	0.4%
2.00 ± 0.11	400	0.394	2.8%	1.6%	2.2%	29.0%	95.7%	93.5%	90.4%	3.7%	4.7%	0.7%
1.42 ± 0.66	400	0.319	1.3%	0.3%	7.9%	24.3%	97.8%	77.9%	96.5%	14.0%	0.9%	0.5%
1.89 ± 0.06	400	0.871	1.7%	0.3%	5.1%	29.0%	97.4%	98.5%	96.3%	8.0%	0.9%	0.3%
1.74 ± 0.04	400	1.435	1.5%	0.2%	10.7%	25.4%	97.6%	99.0%	96.9%	17.4%	0.6%	0.2%
2.06 ± 0.29	380	3.734	4.6%	4.9%	13.6%	19.7%	93.2%	101.9%	78.7%	25.7%	14.5%	0.1%
2.12 ± 0.11	400	0.855	4.6%	2.1%	2.9%	28.0%	93.2%	96.4%	86.7%	4.9%	6.2%	0.3%
1.93 ± 0.08	400	0.802	2.3%	0.8%	5.7%	28.1%	96.5%	99.1%	93.9%	9.3%	2.3%	0.3%
1.73 ± 0.13	400	0.705	3.8%	0.7%	2.2%	27.8%	93.9%	81.8%	91.2%	3.9%	2.1%	0.6%
2.02 ± 0.07	400	0.826	4.7%	0.7%	3.5%	28.5%	92.9%	96.9%	90.5%	5.8%	2.1%	0.3%
1.88 ± 0.08	400	1.398	2.5%	0.4%	6.7%	27.6%	96.2%	98.5%	94.8%	10.8%	1.2%	0.3%
1.91 ± 0.06	400	1.399	2.4%	0.4%	6.2%	28.0%	96.4%	99.4%	94.8%	9.9%	1.3%	0.2%
2.10 ± 0.28	400	1.540	2.6%	2.6%	6.0%	26.9%	96.2%	101.9%	88.2%	10.0%	7.7%	0.3%
1.84 ± 0.11	400	1.349	2.5%	0.9%	8.2%	26.0%	96.1%	97.2%	93.0%	13.7%	2.9%	0.2%
1.87 ± 0.04	400	1.370	2.6%	0.8%	6.8%	27.0%	96.0%	96.9%	93.3%	11.2%	2.5%	0.2%
1.85 ± 0.05	400	1.355	2.3%	0.8%	4.1%	28.3%	96.5%	92.2%	93.6%	6.7%	2.5%	0.3%

γ-Al₂O₃

Feed Ratio MeOH/H ₂ S	Temp °C	WHSV h ⁻¹	mol% in product (N ₂ free basis)				X, MeOH %	X, H ₂ S %	Y, SP %	S, MT %	Y, DME %	Y, HC %
			MeOH	DME	MT	DMS						
2.34 ± 0.24	340	0.198	7.6%	11.1%	4.2%	18.0%	89.2%	74.2%	57.4%	10.6%	31.7%	0.1%
2.15 ± 0.10	360	0.182	5.9%	6.6%	2.8%	23.1%	91.4%	81.7%	71.9%	5.8%	19.3%	0.3%
2.10 ± 0.03	380	0.178	4.5%	3.7%	1.4%	27.0%	93.3%	88.2%	81.8%	2.5%	11.0%	0.5%
2.07 ± 0.06	400	0.175	3.8%	2.4%	0.6%	28.8%	94.3%	90.0%	86.2%	1.0%	7.0%	1.1%
2.39 ± 0.17	400	0.218	5.9%	4.4%	0.4%	27.3%	91.6%	94.1%	78.2%	0.8%	12.6%	0.9%
1.87 ± 0.10	400	0.187	2.6%	1.0%	1.6%	29.3%	95.9%	88.7%	92.3%	2.7%	3.0%	0.6%
1.87 ± 0.02	400	0.252	3.0%	0.9%	2.2%	28.9%	95.4%	89.0%	92.1%	3.7%	2.8%	0.5%
1.52 ± 0.44	400	0.312	2.5%	0.5%	7.2%	24.7%	95.9%	80.5%	93.8%	12.8%	1.8%	0.4%
1.75 ± 0.10	400	0.355	2.2%	0.7%	5.6%	27.1%	96.5%	89.6%	94.0%	9.3%	2.2%	0.3%
1.93 ± 0.16	400	0.261	3.9%	1.9%	2.4%	27.7%	94.1%	88.5%	87.8%	4.2%	5.7%	0.6%
1.90 ± 0.12	400	0.257	3.4%	1.4%	2.7%	28.1%	94.9%	89.4%	89.9%	4.6%	4.4%	0.5%
1.86 ± 0.07	400	0.251	3.7%	1.0%	3.8%	27.6%	94.3%	89.7%	90.8%	6.5%	3.1%	0.4%

HZSM-5

Feed Ratio MeOH/H ₂ S	Temp °C	WHSV h ⁻¹	mol% in product (N ₂ free basis)				X, MeOH %	X, H ₂ S %	Y, SP %	S, MT %	Y, DME %	Y, HC %
			MeOH	DME	MT	DMS						
2.04 ± 0.04	360	0.762	15.0%	7.2%	4.6%	16.6%	77.6%	64.4%	56.2%	12.3%	21.4%	0.1%
1.95 ± 0.05	380	0.728	10.8%	6.9%	3.9%	18.8%	83.6%	66.9%	62.7%	9.3%	20.8%	0.1%
1.95 ± 0.03	400	0.730	7.9%	6.4%	3.0%	21.2%	88.0%	71.4%	68.5%	6.6%	19.3%	0.2%
2.03 ± 0.06	400	0.500	7.0%	6.5%	2.0%	22.4%	89.6%	73.8%	69.9%	4.2%	19.5%	0.2%
1.86 ± 0.15	400	0.366	5.6%	5.0%	1.8%	23.7%	91.3%	72.8%	75.7%	3.6%	15.4%	0.2%
1.72 ± 0.11	400	0.375	5.6%	4.3%	1.9%	23.5%	91.1%	69.2%	77.4%	3.9%	13.5%	0.2%
1.92 ± 0.10	340	0.418	18.6%	6.8%	4.1%	14.7%	71.7%	55.1%	51.0%	12.3%	20.6%	0.1%
1.77 ± 0.03	360	0.377	12.6%	5.6%	3.1%	18.2%	80.1%	58.2%	62.3%	7.9%	17.6%	0.1%
1.73 ± 0.09	380	0.384	9.4%	5.2%	2.3%	20.9%	85.3%	64.1%	69.0%	5.2%	16.2%	0.1%
1.82 ± 0.19	400	0.395	7.0%	4.9%	1.9%	22.8%	89.1%	69.5%	73.7%	4.0%	15.3%	0.2%
1.88 ± 0.24	400	0.405	10.2%	4.9%	2.2%	21.4%	84.3%	68.0%	68.9%	5.0%	15.1%	0.3%
1.89 ± 0.20	400	0.408	13.3%	6.4%	2.1%	18.5%	79.6%	59.5%	59.8%	5.3%	19.6%	0.1%
1.84 ± 0.12	400	0.396	13.1%	5.7%	2.1%	19.0%	79.8%	60.0%	62.1%	5.3%	17.6%	0.1%
1.79 ± 0.12	400	0.387	9.6%	4.3%	2.0%	21.9%	85.0%	67.0%	71.5%	4.5%	13.3%	0.2%

WO₃/ZrO₂

Feed Ratio MeOH/H ₂ S	Temp °C	WHSV h ⁻¹	mol% in product (N ₂ free basis)				X, MeOH %	X, H ₂ S %	Y, SP %	S, MT %	Y, DME %	Y, HC %
			MeOH	DME	MT	DMS						
1.66 ± 0.41	340	0.288	0.1%	0.3%	8.5%	26.5%	99.8%	93.0%	98.5%	13.9%	0.9%	0.4%
1.35 ± 0.62	340	0.356	0.2%	0.4%	12.0%	22.1%	99.6%	80.1%	97.7%	21.4%	1.4%	0.4%
1.30 ± 0.08	340	0.632	0.1%	1.5%	13.6%	19.8%	99.8%	76.8%	94.3%	25.6%	5.1%	0.4%
1.52 ± 0.31	340	1.150	3.5%	5.2%	12.5%	16.9%	94.2%	74.0%	76.5%	27.0%	17.3%	0.4%
1.35 ± 0.10	340	0.678	0.0%	1.1%	14.6%	20.1%	100.0%	81.5%	95.5%	26.6%	4.0%	0.5%
1.62 ± 0.22	340	0.654	0.0%	2.5%	11.9%	22.2%	100.0%	89.6%	91.2%	21.2%	8.1%	0.7%
2.05 ± 0.12	340	0.654	0.3%	4.6%	8.1%	24.5%	99.6%	99.3%	84.9%	14.2%	13.8%	0.9%
2.00 ± 0.09	360	0.638	0.0%	3.0%	5.4%	27.0%	100.0%	97.2%	89.2%	9.0%	9.1%	1.7%
2.39 ± 0.16	340	0.418	1.1%	6.7%	2.5%	26.4%	98.4%	98.3%	78.5%	4.6%	19.1%	0.7%
2.18 ± 0.17	340	0.396	0.8%	4.9%	3.9%	26.8%	98.8%	97.7%	83.9%	6.7%	14.2%	0.7%
1.94 ± 0.07	340	0.373	0.0%	2.8%	5.7%	27.1%	100.0%	96.2%	90.8%	9.4%	8.6%	0.6%
2.20 ± 0.28	340	0.269	1.2%	4.5%	1.9%	28.1%	98.3%	95.9%	84.4%	3.3%	13.0%	0.9%
2.06 ± 0.14	360	0.251	1.7%	1.9%	0.8%	29.8%	97.5%	93.5%	89.7%	1.3%	5.8%	1.9%
1.97 ± 0.17	360	0.264	0.9%	0.8%	2.5%	30.1%	98.6%	96.7%	94.5%	4.1%	2.5%	1.6%
1.99 ± 0.17	340	0.267	0.4%	2.5%	4.2%	28.3%	99.4%	97.1%	91.4%	6.9%	7.4%	0.7%
2.03 ± 0.11	340	0.272	0.2%	2.2%	3.5%	29.1%	99.6%	98.7%	92.0%	5.7%	6.7%	0.9%
2.11 ± 0.09	340	0.283	0.0%	4.3%	4.3%	27.2%	100.0%	97.9%	86.4%	7.3%	12.7%	1.0%
2.06 ± 0.14	340	0.276	0.0%	5.0%	5.4%	25.4%	100.0%	94.2%	83.6%	9.6%	14.8%	1.6%
2.02 ± 0.10	340	0.272	0.7%	3.8%	4.6%	26.7%	98.9%	94.8%	86.8%	7.9%	11.4%	0.8%

WO₃/Al₂O₃

Feed Ratio MeOH/H ₂ S	Temp °C	WHSV h ⁻¹	mol% in product (N ₂ free basis)				X, MeOH %	X, H ₂ S %	Y, SP %	S, MT %	Y, DME %	Y, HC %
			MeOH	DME	MT	DMS						
0.61 ± 0.14	360	0.184	7.5%	3.4%	20.4%	1.5%	80.2%	35.4%	61.9%	86.9%	18.0%	0.3%
0.74 ± 0.04	380	0.224	6.5%	4.1%	23.7%	2.1%	84.8%	45.0%	65.4%	84.8%	19.0%	0.4%
0.66 ± 0.01	400	0.198	4.4%	2.1%	25.7%	2.6%	88.9%	46.8%	77.7%	83.3%	10.5%	0.7%
0.70 ± 0.09	340	0.209	17.1%	2.9%	16.7%	0.7%	58.4%	29.4%	44.0%	92.5%	14.2%	0.2%
0.86 ± 0.14	340	0.258	20.6%	3.6%	16.9%	0.7%	55.2%	32.7%	39.6%	92.7%	15.5%	0.2%
0.62 ± 0.02	340	0.276	16.9%	2.4%	15.7%	0.5%	56.1%	26.4%	43.6%	93.5%	12.3%	0.2%
0.33 ± 0.04	340	0.143	6.6%	0.9%	15.3%	0.6%	73.5%	21.2%	66.2%	92.9%	7.0%	0.3%
0.32 ± 0.01	360	0.140	3.8%	0.6%	17.9%	0.7%	84.6%	24.6%	78.9%	92.4%	5.3%	0.4%
0.34 ± 0.06	380	0.144	2.4%	0.4%	19.8%	0.9%	90.6%	27.7%	86.3%	91.4%	3.5%	0.7%
0.31 ± 0.01	400	0.135	0.9%	0.2%	20.3%	1.0%	96.3%	28.1%	93.5%	91.0%	1.4%	1.4%
0.47 ± 0.05	340	0.082	4.7%	1.6%	21.8%	1.1%	85.3%	33.7%	74.9%	90.6%	10.2%	0.2%
0.46 ± 0.07	360	0.079	2.5%	1.0%	23.7%	1.5%	92.0%	36.6%	85.0%	88.9%	6.6%	0.4%
0.42 ± 0.08	380	0.073	0.9%	0.4%	24.2%	1.6%	97.0%	36.6%	93.4%	88.0%	3.0%	0.7%
0.43 ± 0.04	400	0.074	0.4%	0.2%	24.9%	1.9%	98.7%	38.2%	96.2%	86.7%	1.4%	1.2%
0.38 ± 0.02	400	0.165	1.0%	0.3%	23.2%	1.4%	96.6%	34.0%	93.4%	89.5%	2.4%	0.7%
0.51 ± 0.09	400	0.219	3.4%	1.1%	25.4%	1.3%	89.9%	40.3%	83.1%	90.7%	6.3%	0.6%
0.46 ± 0.03	400	0.198	3.1%	0.7%	24.5%	1.2%	90.1%	37.5%	85.2%	91.2%	4.2%	0.7%
0.41 ± 0.02	400	0.177	0.7%	0.4%	24.2%	1.6%	97.5%	36.4%	94.0%	88.0%	2.8%	0.7%

MoO₃/SiO₂

Feed Ratio MeOH/H ₂ S	Temp °C	WHSV h ⁻¹	mol% in product (N ₂ free basis)				X, MeOH %	X, H ₂ S %	Y, SP %	S, MT %	Y, DME %	Y, HC %
			MeOH	DME	MT	DMS						
1.82 ± 0.24	360	0.231	44.0%	1.9%	3.4%	5.6%	31.9%	25.3%	22.6%	23.0%	6.0%	3.3%
0.88 ± 0.88	400	0.112	11.1%	1.3%	10.9%	6.0%	76.4%	31.8%	49.0%	47.3%	5.6%	21.9%
0.33 ± 0.34	340	0.057	9.4%	0.9%	9.3%	1.9%	62.3%	14.9%	52.4%	71.6%	7.2%	2.7%
0.35 ± 0.18	360	0.061	3.7%	1.0%	11.3%	3.1%	85.7%	19.5%	67.8%	64.3%	8.0%	9.8%
0.31 ± 0.13	380	0.053	1.0%	0.6%	10.3%	2.6%	95.8%	16.8%	65.7%	66.7%	4.8%	25.3%
0.28 ± 0.06	400	0.049	0.2%	0.1%	7.7%	1.3%	99.2%	11.5%	46.4%	75.3%	1.3%	51.5%

SAPO-18

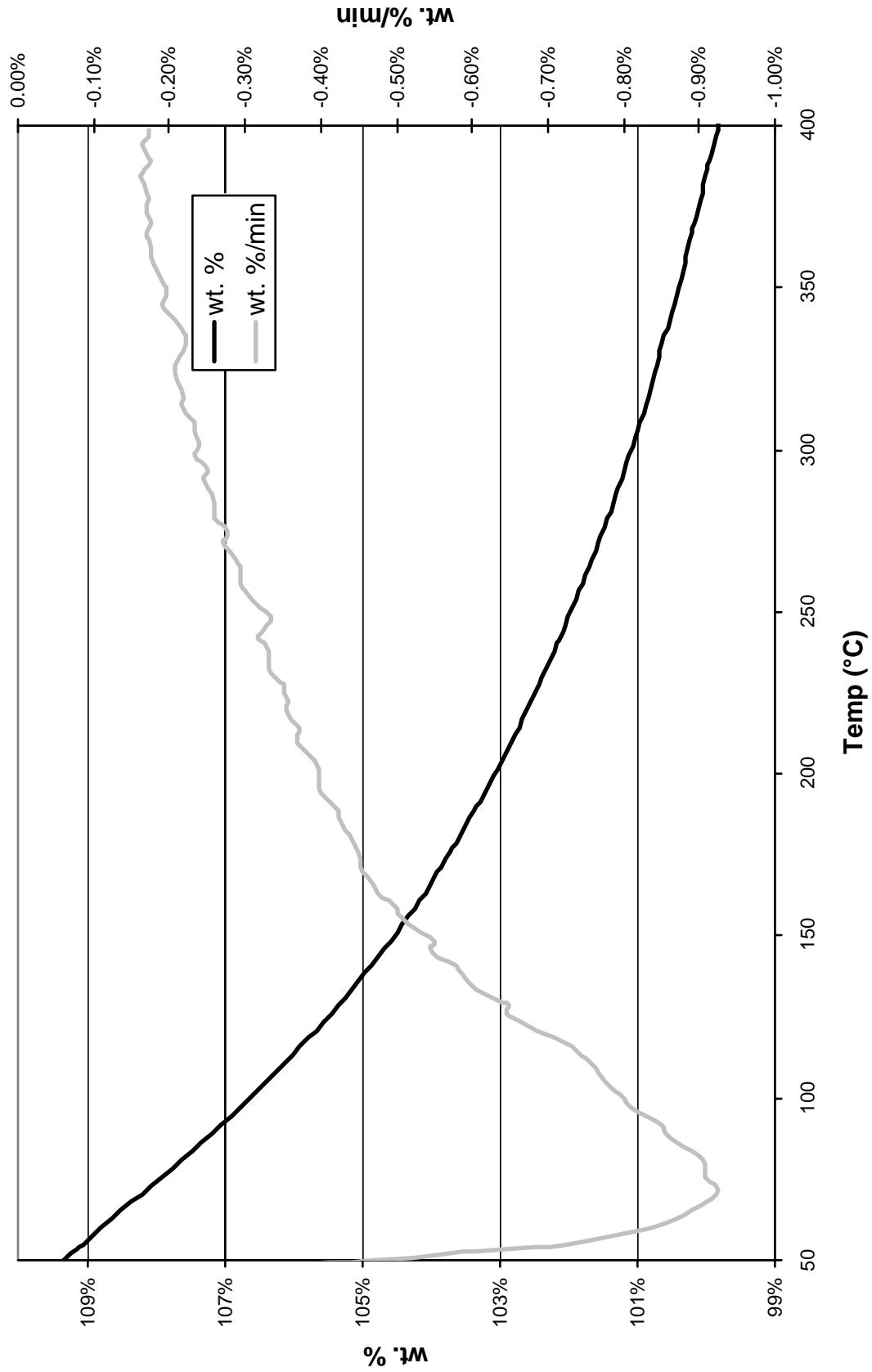
Feed Ratio MeOH/H ₂ S	Temp °C	WHSV h ⁻¹	mol% in product (N ₂ free basis)				X, MeOH %	X, H ₂ S %	Y, SP %	S, MT %	Y, DME %	Y, HC %
			MeOH	DME	MT	DMS						
2.09 ± 0.20	360	0.558	4.0%	29.1%	2.7%	0.8%	94.0%	10.8%	6.4%	62.8%	86.2%	1.5%
2.16 ± 0.20	400	0.578	4.3%	23.1%	5.5%	2.8%	93.6%	26.3%	16.2%	49.5%	67.6%	9.8%
1.40 ± 0.18	360	0.525	3.3%	21.6%	4.3%	1.5%	94.3%	14.0%	12.7%	58.7%	74.0%	7.6%
1.16 ± 0.17	360	0.584	3.1%	18.8%	2.0%	5.3%	94.2%	15.9%	23.7%	16.1%	70.0%	0.5%
0.96 ± 0.19	380	0.483	2.4%	12.3%	2.3%	9.4%	95.1%	22.9%	43.1%	11.0%	50.4%	1.6%

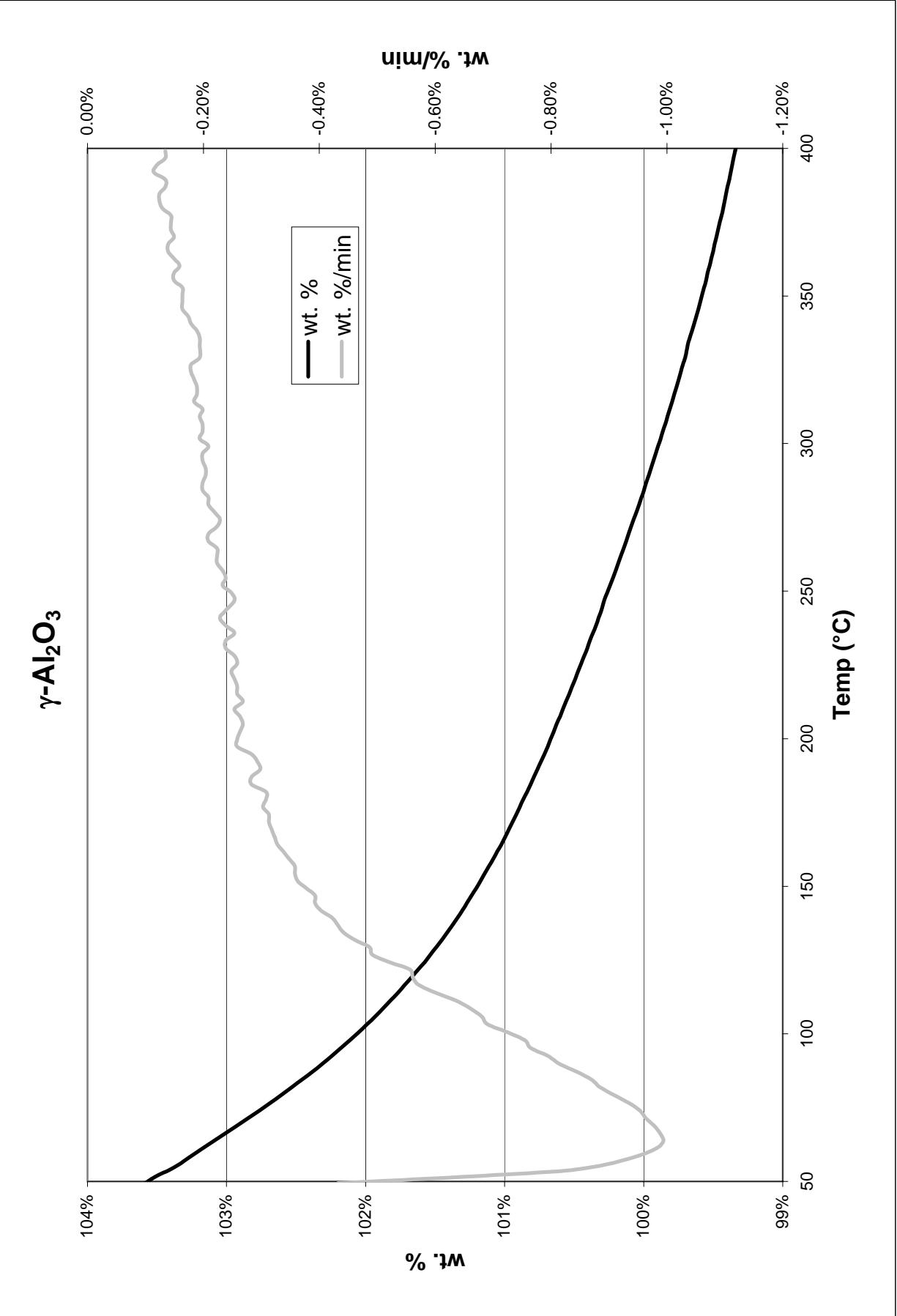
AlPO-18

Feed Ratio MeOH/H ₂ S	Temp °C	WHSV h ⁻¹	mol% in product (N ₂ free basis)				X, MeOH %	X, H ₂ S %	Y, SP %	S, MT %	Y, DME %	Y, HC %
			MeOH	DME	MT	DMS						
2.08 ± 0.17	360	0.409	4.7%	28.6%	2.4%	1.5%	93.0%	12.0%	8.0%	44.2%	84.8%	0.2%
1.24 ± 0.07	360	0.388	3.8%	23.0%	2.6%	1.4%	93.1%	9.0%	9.8%	47.2%	83.0%	0.2%
1.21 ± 0.08	400	0.380	3.4%	18.5%	3.8%	4.9%	93.8%	19.4%	25.0%	27.9%	67.5%	1.3%
1.53 ± 0.17	400	0.430	4.1%	18.8%	5.3%	6.6%	93.3%	30.0%	30.4%	28.6%	62.2%	0.7%
2.89 ± 0.67	400	0.240	5.3%	21.4%	4.1%	10.0%	92.8%	54.5%	32.3%	17.0%	57.7%	2.9%

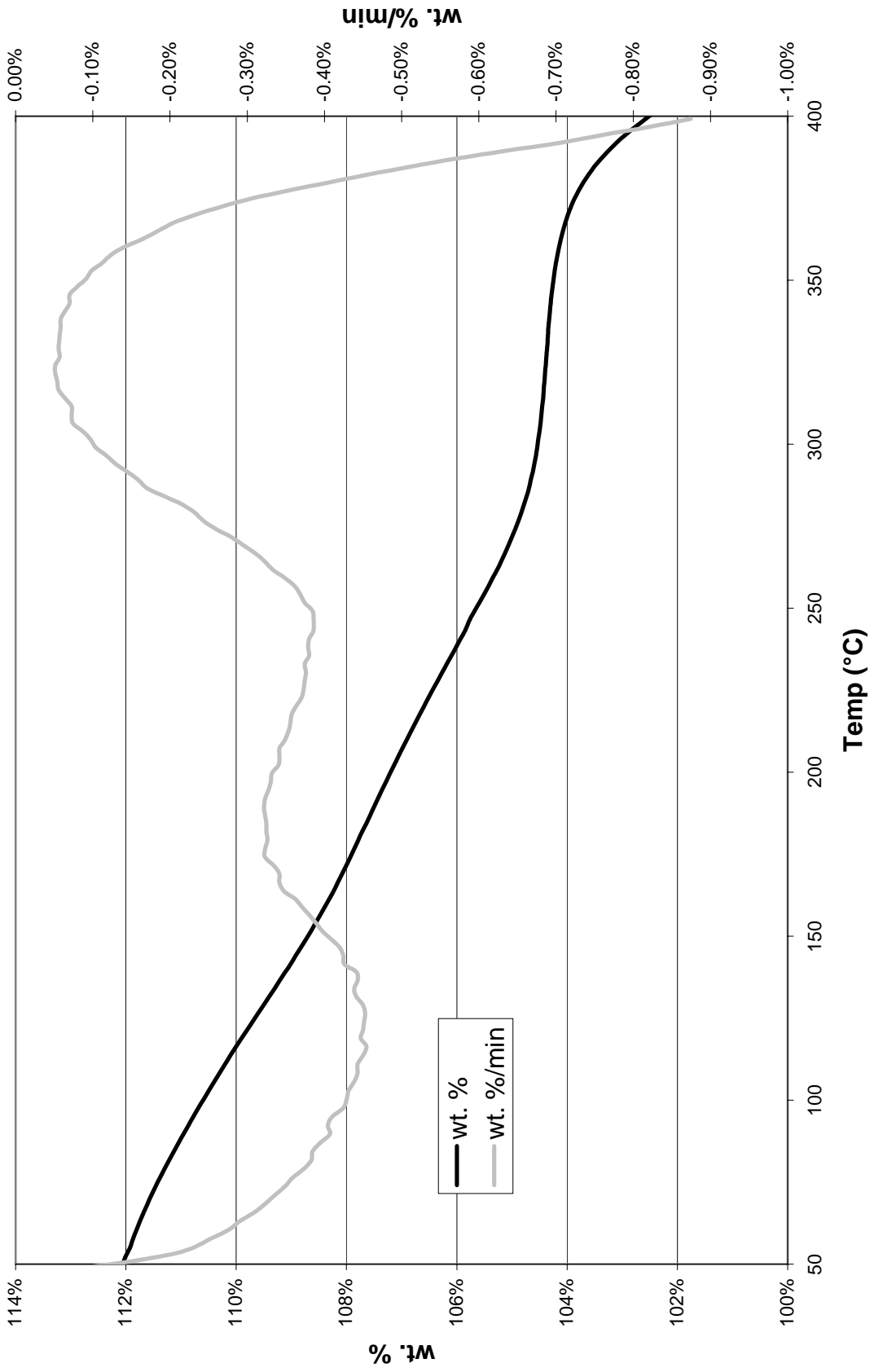
ACID SITE CHARACTERIZATION RESULTS

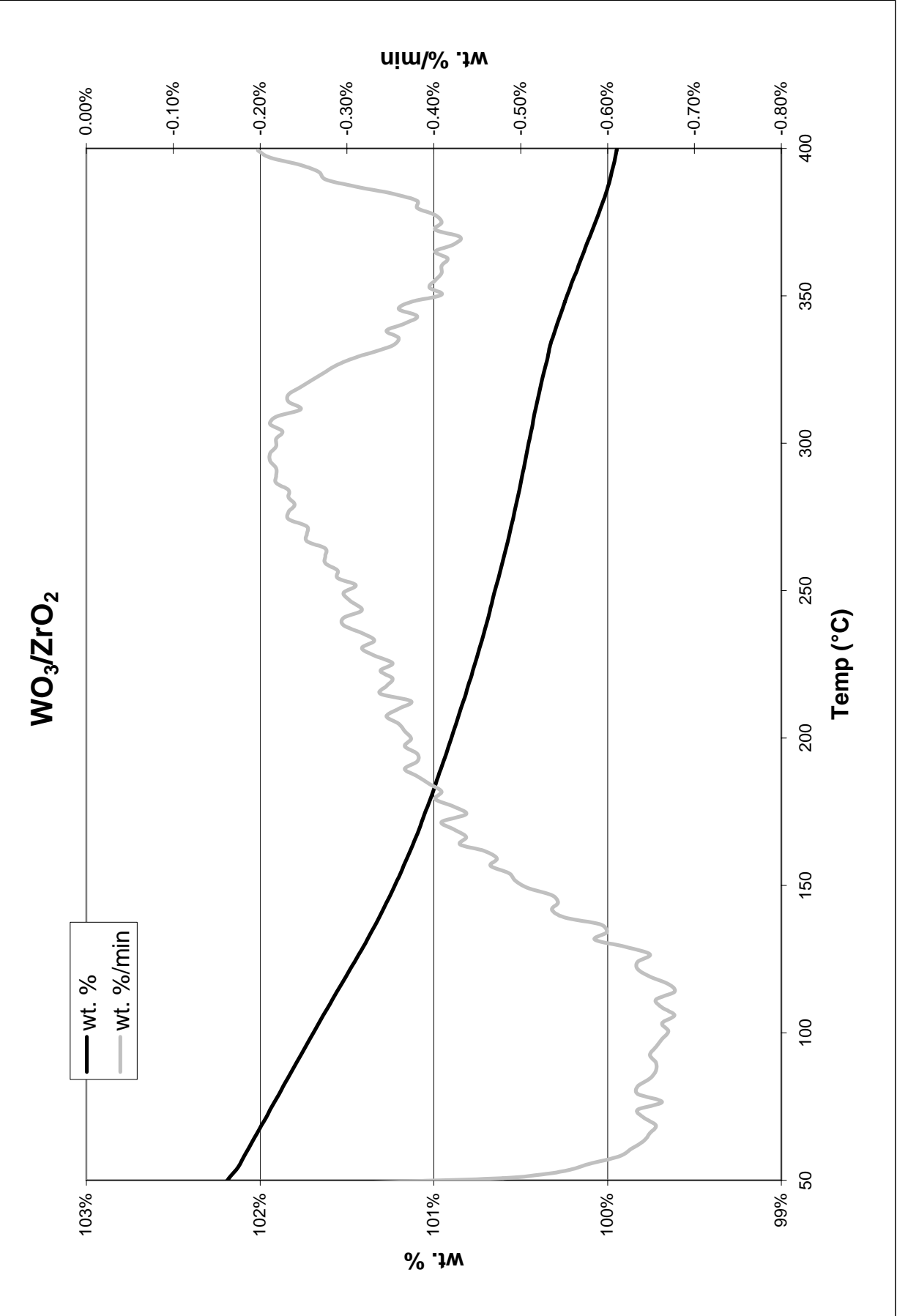
La₂O₃/Al₂O₃

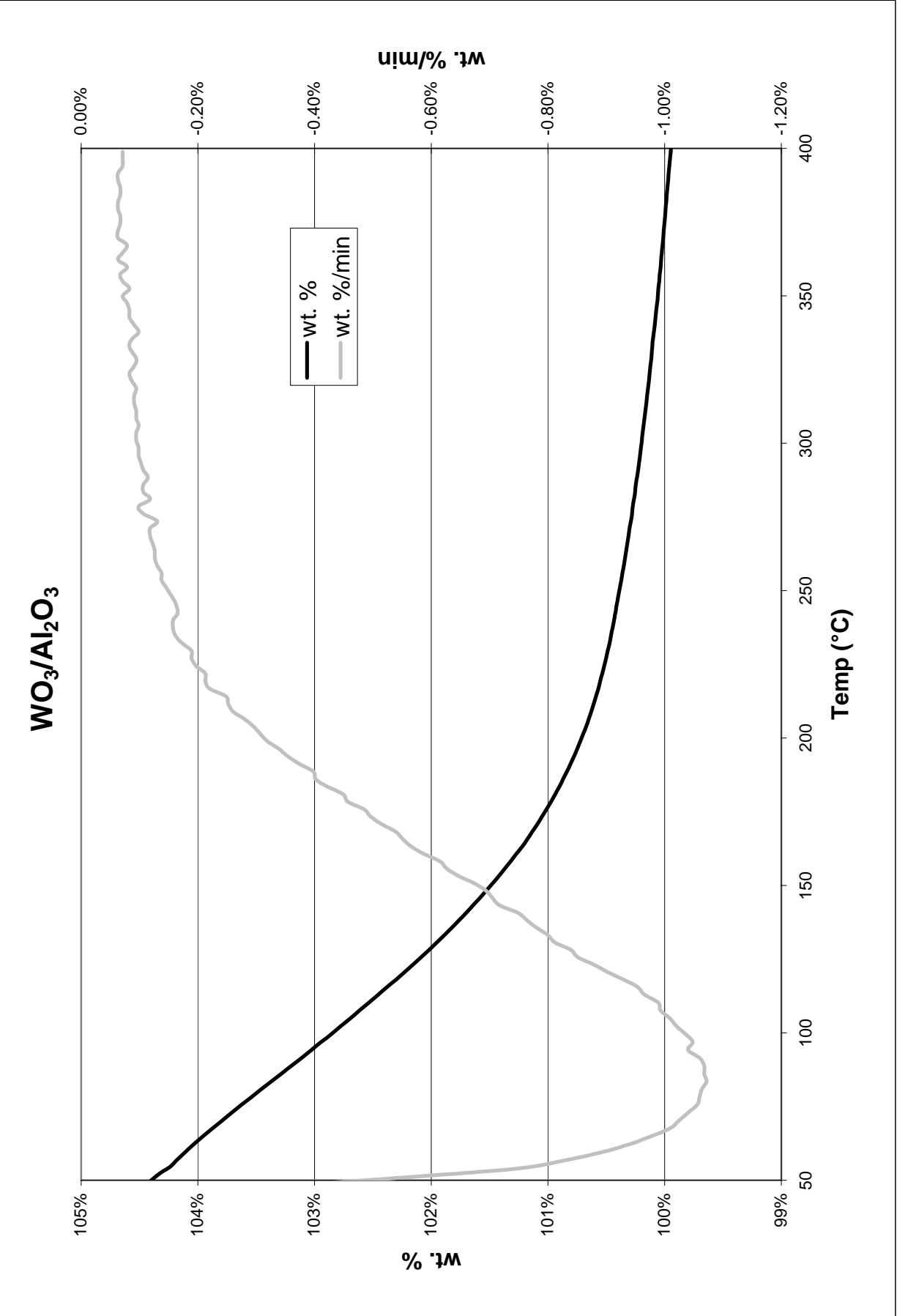




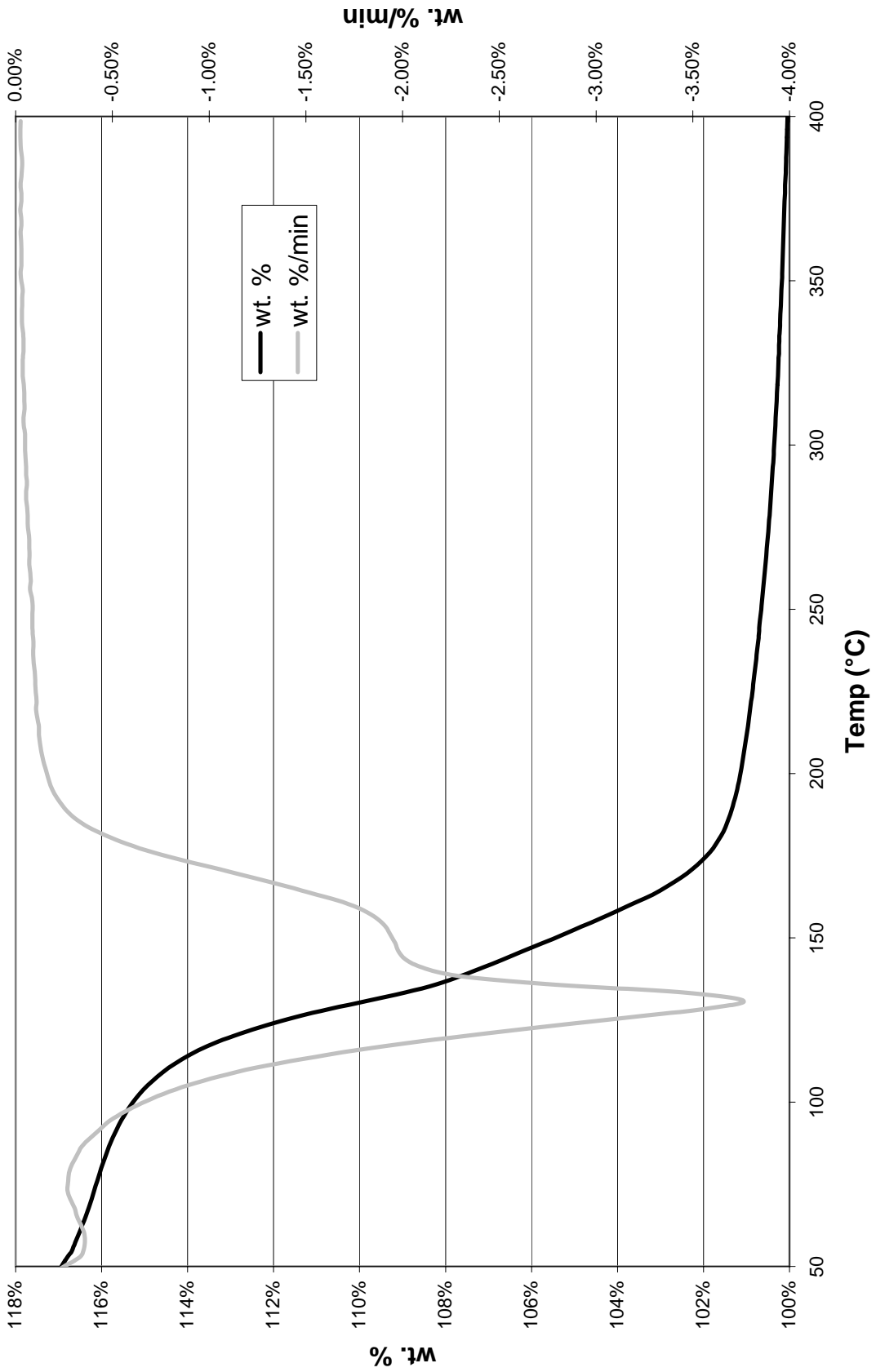
HZSM-5



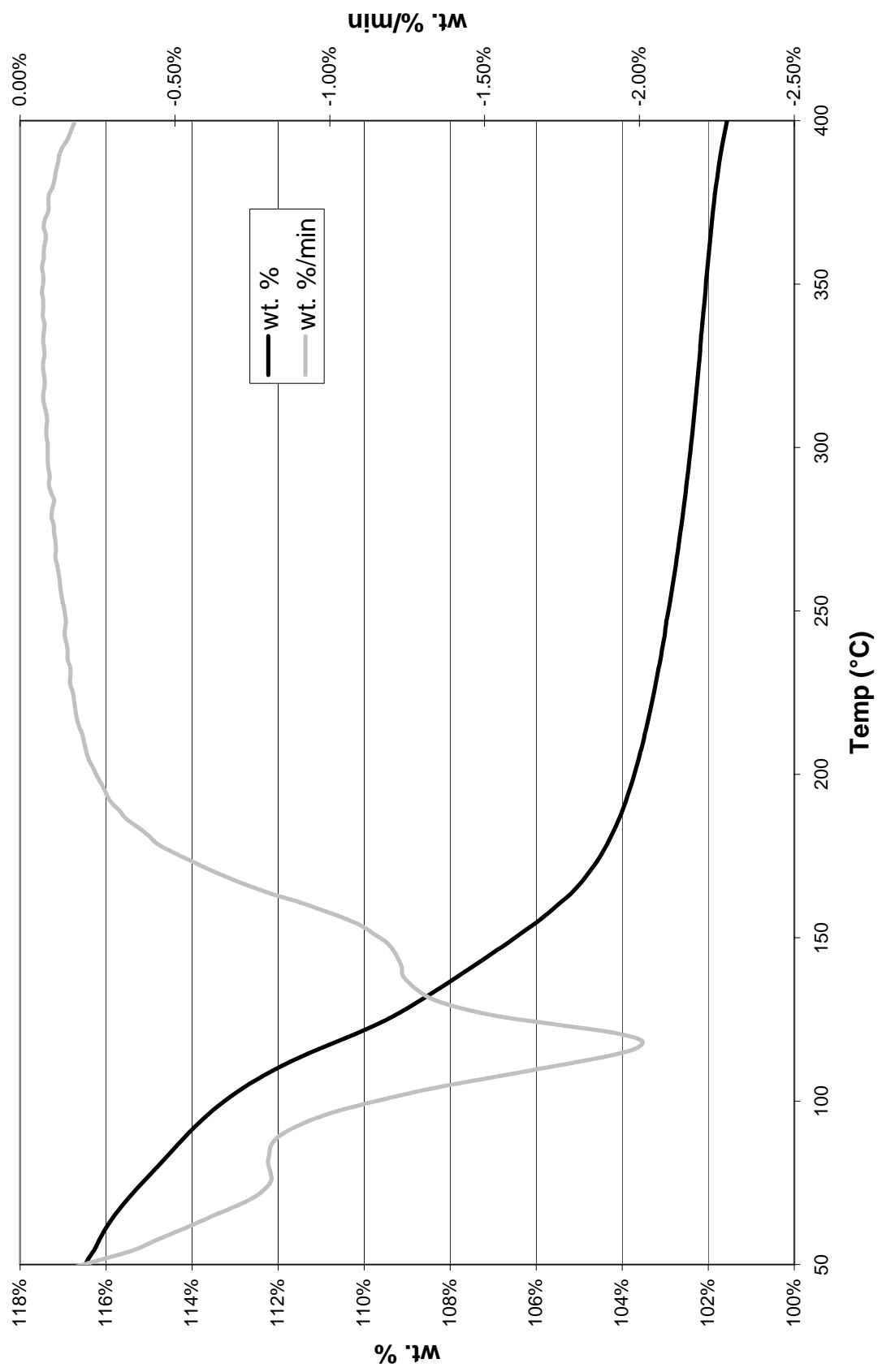


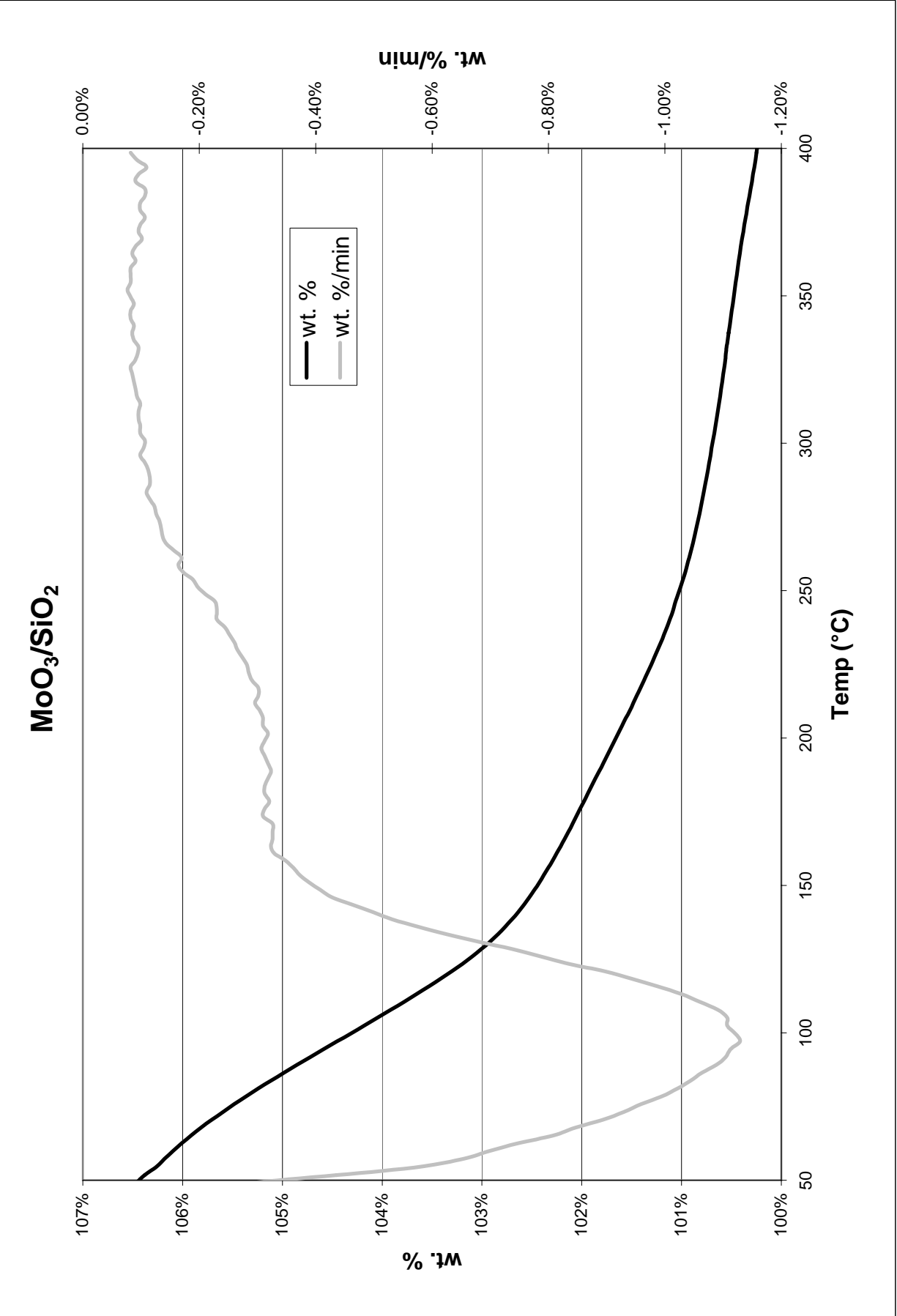


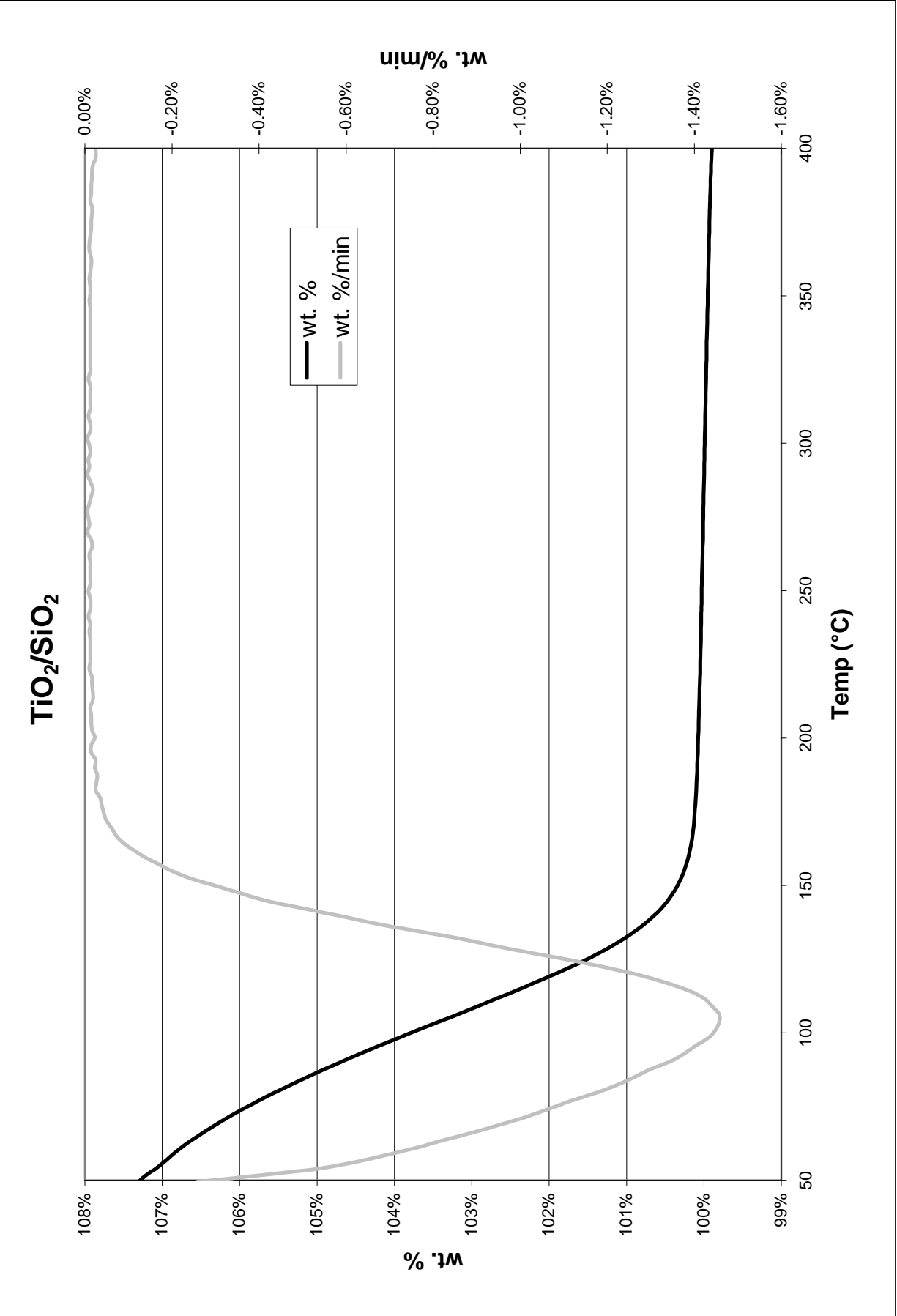
AIPO-18



SAPO-18







VITA

Craig Plaisance was born in 1981, to George and Christina Plaisance, in Baton Rouge, Louisiana. He completed his high school education in Baton Rouge in 2000. He was accepted by Louisiana State University into the Department of Chemical Engineering and earned a Bachelor of Science in 2003. Upon graduation, he continued his education in the graduate program of the same department. This thesis completes his requirements to receive the degree of Master of Science in Chemical Engineering.